Universidad Tecnica Federico Santa Maria

Departamento de física

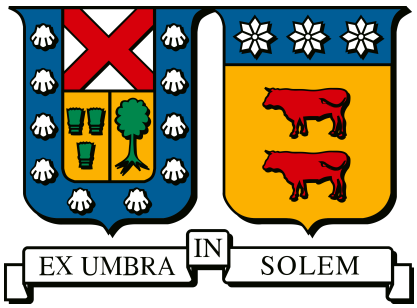

A thesis submitted for the degree of

Master in Physics

Transverse momentum broadening of DIS multiple-pion events with CLAS at Jefferson lab

---

Matías Eduardo Barría Lopez

Advisor: Hayk Hakobyan

2023

The purpose of a storyteller is not to tell you how to think,

but to give you questions to think upon.

Brandon Sanderson

Acknowledgements

Primero me gustaría agradecer a mis padres, Jorge y Marcela y a mi hermana Jessica por su apoyo a lo largo de todo mi proceso universitario sin ellos no estaría aquí.

Gracias Hayk por el conocimiento y la guía que me diste en el proceso y por introducirme en un área que no sabía que me iba a gustar tanto. Gracias a Will y Taya por todos sus comentarios y consejos sobre la investigación.

Gracias a la gente del CCTVal que conocí durante este año y medio en el centro especialmente a los del segundo piso A.K.A "Los del fondo". A Antonio, Bruno , Claudio aunque la conclusión final siempre fuera "Esta todo trucho" y a Esteban por ahorrarme meses de trabajo literalmente.

Gracias a mis amigos de toda la vida por estar siempre ahí.

Finalmente Gracias a Brandon Sanderson a quien descubrí durante este tiempo y a Eichiro Oda por ayudarme con sus obrar a recuperar energías en mis momentos libres.

Abstract

High energy physics has experienced a large number of discoveries in the last decades. However, one of the processes that is not fully understood yet is the hadronization process.

To obtain more information about this process, this thesis analyzed data from electron-nucleon collisions. The data were collected during the EG2 experiment carried out at Hall B in the Thomas Jefferson National Accelerator Facility. The beam had 5.014 GeV of energy and the targets used were carbon, iron, lead, and deuterium.

The main goal of the thesis was to obtain the measurement of transverse momentum broadening of DIS multiple-pion events as a function of different kinematic variables and the size of the target.

Contents

Chapter 1

Physics Motivation

This chapter aims to give context about particle physics and why the experiment and this analysis were done. Also, it gives a brief summary of the theory of the studied scattering. The information of this chapter, as well as more detail, can be found in [1], [2], [3].

Particle physics or high energy physics tries to understand what are the most fundamental components of the universe and how they interact, giving rise to all the known matter.

The first particle discovered was the electron in the late 1800's, then in the early 1900's new subatomic particles were discovered. Since then, particle physics has evolved into a highly sophisticated and complex field of study involving particle accelerators, detectors, and other advanced technologies. This improvement leads to the discovery of a lot of new particles.

1.1 Quarks, Hadrons, and the Eightfold Way

In the 50's and 60's, a lot of new particles were discovered; some of them can be seen in Tab. 1.1. The number of discovered particles was much bigger than the physicists expected; hence, they started to suspect that those particles were not fundamental and were compounded by something else.

The discovered particles could be categorized into: mesons, which are fermions, and baryons, which are bosons. The physicists also realized that these particles could be grouped into smaller groups if they defined new quantum numbers. This method was called the Eightfold Way (see Fig 1.1). The new quantum numbers were the Baryonic

Particle	Charge	Spin	Mass(MeV)
π^0	0	0	134.98
$\pi^{\pm}$	± 1	0	139.57
$\rho^{0,\pm}$	0, $\pm .1$	1	~ 775.11
$\Delta^{0,\pm,++}$	0, ± 1,2	$\frac{3}{2}$	~ 1232

Table 1.1: List of some hadrons and its quantum numbers

number (B), the strangeness (S), and isospin (T_3). It is also helpful to define the hypercharge as $Y = B + S$; furthermore, the charge can be written as $Q = T_3 + Y/2$. Once they studied the groups, they noticed that they had the form of the representation of the SU(3) group. Using this model it was even possible to predict the existence of new particles to fill the empty spaces in some groups, such as the Ω^- baryon.

This group can be explained as the combination of particles in the fundamental representation of SU(3). Therefore, M. Gell-Mann and G. Zweig proposed the existence of particles with spin $\frac{1}{2}$ and fractional electric charge and baryonic number. These particles are known as quarks. They proposed three different flavors of quarks (up (u), down (d), and strange (s)). Mesons would be the combination of two of them (quark-antiquark), and baryons the combination of three quarks (antiquarks).

Nowadays, thanks to more energetic experiments, it is known there exit other types of quarks (charm (c), bottom (b), top(t)) and, in combination, they generate all the known hadrons (top quarks do not generate hadrons because they are too massive and decay too quickly).

Looking at the case of the Ω^- baryon inner structure (sss), it can be noticed that three strange quarks form it. In addition to the fact that it has spin 3/2, this implies that all the quarks have to be in the same quantum state, breaking the Fermi-Dirac statistics. To avoid this, the quarks must have another quantum number, called *Color charge*, which must have at least three different values.

Color charge is the source of a gauge interaction that generates the strong force. The quantum field theory which describes it is named Quantum ChromoDynamics (QCD).

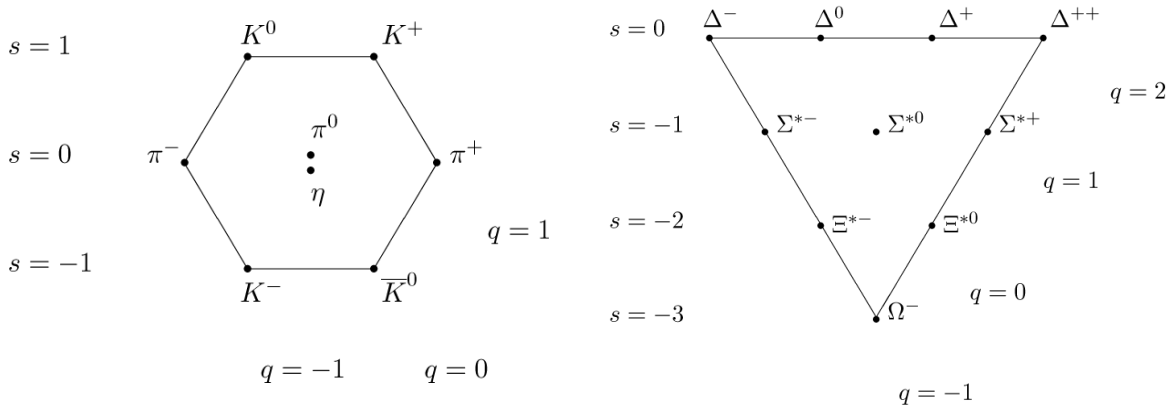

(a) Meson octet (b) Baryon decuplet

Figure 1.1: Hadrons organization in the Eightfold Way. On the left meson octet with spin 0, and in the right baryon decuplet with spin $\frac{3}{2}$. Particles in the same diagonal have the same charge, in the same column have the same isospin, and in the same row have the same strangeness

1.2 QCD and the coupling constant

QCD is a non-abelian gauge theory with symmetry group SU(3), which explains the interaction of color charge particles, and it is described by the following Lagrangian.

$$\mathcal{L}_{\text{QCD}} = \bar{\psi}_i \left(i\gamma^\mu (D_\mu)_{ij} - m\,\delta_{ij}\right)\psi_j - \frac{1}{4} G^a_{\mu\nu} G^{\mu\nu}_a \tag{1.1}$$

$$G^a_{\mu\nu} = \partial_\mu \mathcal{A}^a_\nu - \partial_\nu \mathcal{A}^a_\mu + g f^{abc} \mathcal{A}^b_\mu \mathcal{A}^c_\nu \tag{1.2}$$

where ψ_i is the quark field and f^{abc} are the SU(3) structure constants. The interaction occurs through the exchange of color charge bosons called gluons ($\mathcal{A}^a_\nu$), which emerge in the theory as a consequence of the local gauge symmetry. Gluons can interact between them, in contrast with the photons in QED.

The interaction between quarks and gluons generates the hadrons measurement in the experiments and keeps the nucleons (protons and neutrons) together in the nuclei of the atom, in spite of the electric repulsion.

The QCD coupling constant (the factor that determines the strength of the interaction) depends on the energy scale (see Fig 1.2). The behavior of the coupling constant at high energy scales is called asymptotic freedom and implies that quarks interact weakly at high energies, and some perturbative calculations are allowed. On the other hand, when the energy scale decreases, the coupling constant rises, and the interaction becomes

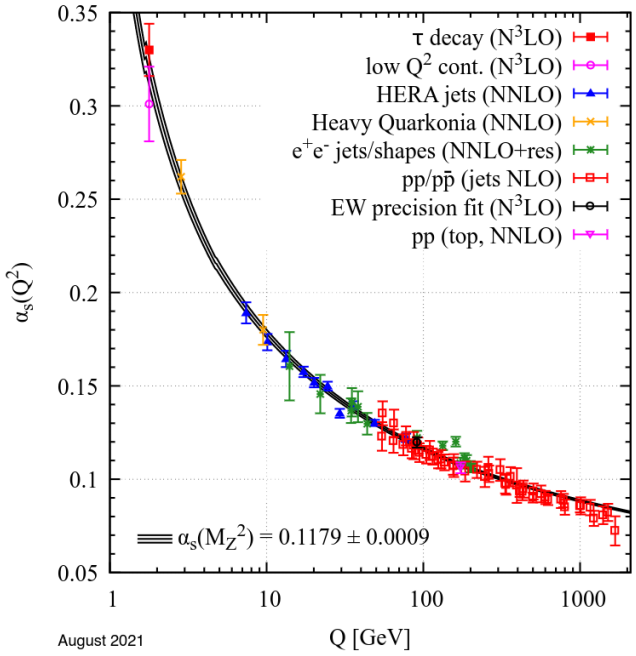

Figure 1.2: Summary of measurements of α_s as a function of the energy scale Q. Plot taken from [3]

stronger. This fact caused color charge particles to not be isolated, so the quark and gluons had to stick together, forming colorless objects (technically, the objects must be invariant under rotations in the color complex space); this is called color confinement. There is not any analytic proof of color confinement yet.

1.3 Hadronization

Color confinement implies that quarks and gluons cannot be directly detected in regular conditions (temperatures below the 2×10^{12}K). The process where quarks and gluons clump together and form colorless hadrons is called *hadronization*.

The hadronization process can be phenomenologically described in two different subprocesses or two timescales.

- **Production length** (l_p): This process occurs right after the quark is taken out of the nucleon. Here the parton can radiate gluons or produces a quark-antiquark pair. This process ends when the quark neutralizes its color, forming a prehadron.

- **Hadron formation length** (l_f): In this stage, the prehadron propagates until it collapses into a hadron.

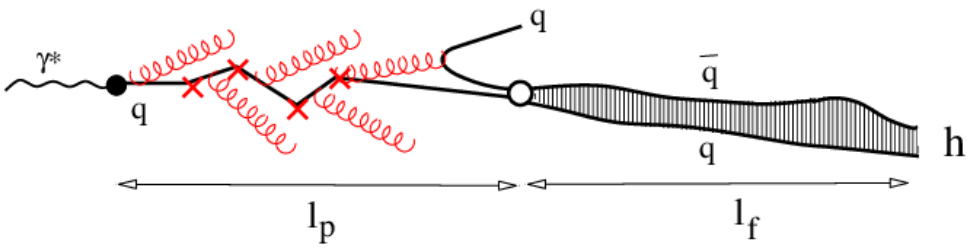

Figure 1.3: The two timescales of the hadronization process. Image taken from [4]

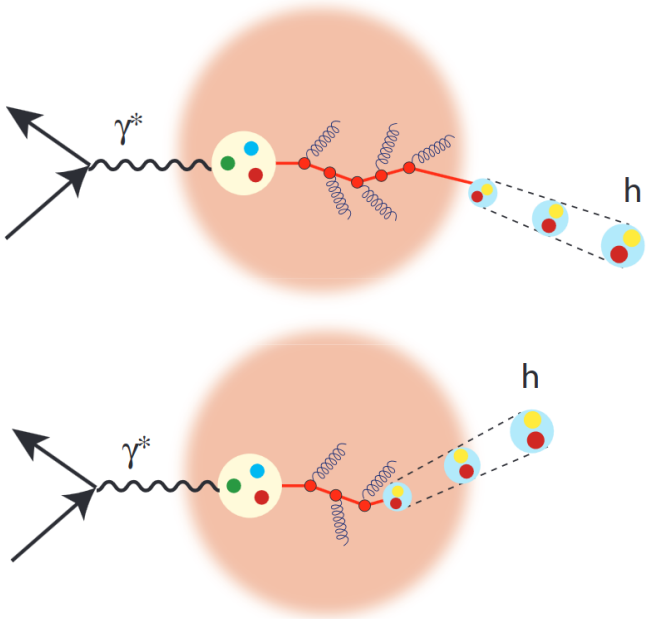

Figure 1.4: Illustration of a parton moving through nuclear media. At the top the prehadron is formed outside the nuclei and at the bottom it is formed inside. The figure is taken from [5]

.

The two timescales can be visualized in Fig 1.3.

One method to study the hadronization process is changing of the medium where the process takes place. The medium can be changed by introducing a nuclear medium because the hadronization distances are in the order of a nuclear diameter for medium energy DIS. The effects of this medium are important because they can be measured by comparing the final hadron states with and without nuclear media. From those measurements, information can be extracted for both time scales of the hadronization process.

The production length can be bigger or smaller than the nucleon size, so the prehadron can be formed inside or outside the nuclei (see Fig 1.4). This can be studied by changing the size of the nuclei and the kinematic variables.

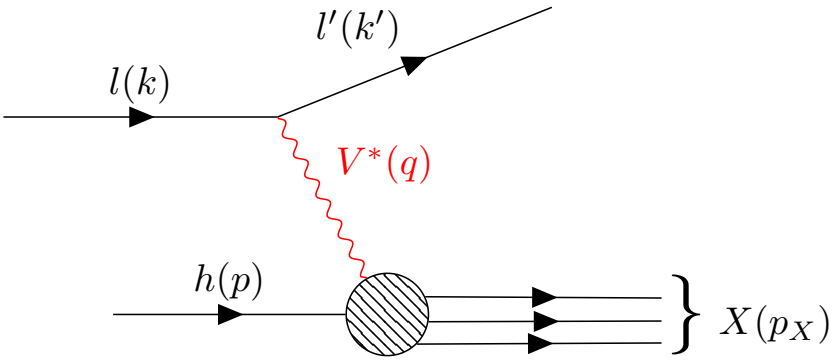

Figure 1.5: Schematic diagram of DIS.

1.4 Deep inelastic scattering

The most common way of studying the inner structure of the nucleons and the hadrons, and the hadronization process, is called Deep Inelastic Scattering (DIS).

DIS is the name of the scattering between lepton and a nucleon and it has the following form (also see Fig 1.5):

$$l(k) + h(p) \rightarrow l'(k') + X(p_X) \tag{1.3}$$

where l and l' represent the lepton before and after the scattering and k and k' represent the 4-momentum of respectively: h represents the initial nucleon which has a 4-momentum p; and X represents the hadronic final state particles. The interaction is mediated by the exchange of a virtual vector boson, V* (γ, $W^{\pm}$ or Z), which carries a 4-momentum $q = k - k'$. In the experiment studied in this thesis, the leptons were electrons, and the intermediary boson was a photon because the beam of electrons had not enough energy to produce bosons with the mass of $W^{\pm}$ or Z; consequently, the weak interaction was not taken into account (There is a small contribution of $W^{\pm}$ or Z because virtual bosons could be off shell, but it was not taken into account). The word Deep in DIS comes from the idea that the lepton interacts directly with the inner components of the nucleon. This condition is guaranteed to set a lower limit in the virtuality $Q^2 \equiv -q^2 > 1\ GeV^2$, corresponding to a spatial resolution of around 0.2 fm.

Taking the reference frame where the nucleon is at rest (lab frame) the nucleon and

lepton 4-momentum is given by:

$$\begin{aligned} p &= (M, 0, 0, 0) \\ k &= (E, 0, 0, E) \\ k &= (E', \vec{k}) \\ q &= (E - E', \vec{k} - \vec{k'}) \end{aligned} \tag{1.4}$$

From now on, in the thesis, natural units will be used, which means $c = \hbar = 1$. In the lab frame the virtuality can be written as

$$\begin{aligned} Q^2 &= -(q \cdot q) \\ &= -\left(2m_e^2 - 2EE'\left(1 - \frac{|\vec{k}||\vec{k'}|}{EE'}\cos(\theta)\right)\right) \\ &\approx 4EE'\sin^2\left(\frac{\theta}{2}\right) \end{aligned} \tag{1.5}$$

where θ is the angle between the incoming and scattered lepton and in the last line ultrarelativistic approximation was used, which means that $k^2 = k'^2 = m_e^2 \approx 0$. Also we can define ν as:

$$\nu \equiv \frac{p \cdot q}{M} \overset{lab}{=} E_k - E_{k'}; \tag{1.6}$$

which in the lab frame represents the energy of the virtual boson.

Different from the case of elastic scattering, the mass of the final hadron state is not longer the mass of the initial nucleon M, but it has the following form:

$$W = (p + q)^2 \overset{lab}{=} M^2 + q^2 + 2M\nu \tag{1.7}$$

In Fig 1.6 a differential cross section can be seen. In the distribution there are some peaks related to resonances, in these cases the final hadron comes from the decay of the resonance. This process could be for example:

$$e + p \to e + \Delta^+ \to e + p + \pi^0, \tag{1.8}$$

in this case the proton is excited to a Δ^+ which then decays into a proton and a neutral pion. This will be useful when we select events in Sec 3.

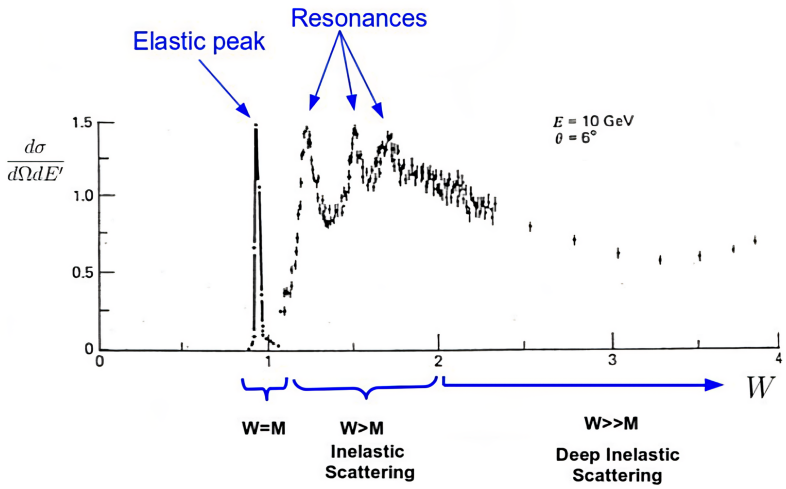

Figure 1.6: Differential cross section for fixed θ and E as a function of W in GeV/c^2.

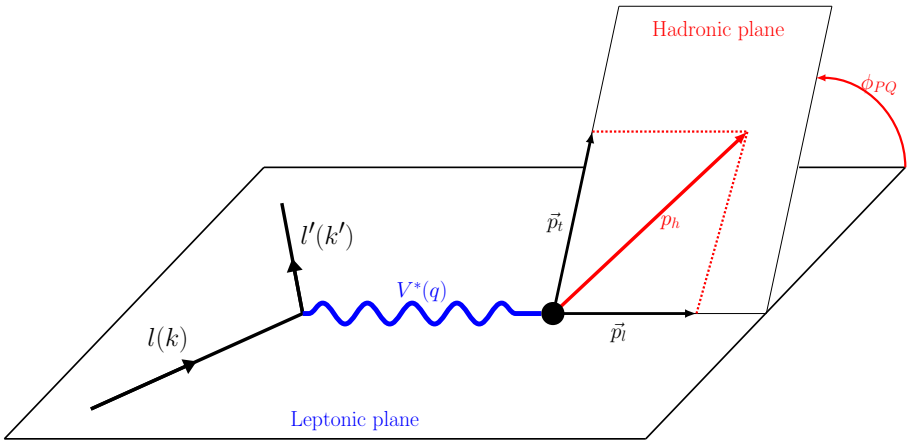

Figure 1.7: Schematic representation of a SIDIS process and some of the variables involved

DIS is usually separated into three different cases according to the detected particles in the final state. One is called inclusive DIS when only the scattered lepton is detected. Then there is the case when all particles are detected; this is called exclusive DIS. Finally, there is the case in which just one hadron is detected; this is called semi-inclusive DIS (SIDIS). The SIDIS reaction has the following form:

$$l(k) + h(p) \rightarrow l'(k') + h(p_h) + X(p_X), \tag{1.9}$$

where h represents the detected hadron which carries a 4-momentum p_h. A schematic representation of SIDIS can be seen in Fig 1.7

In the lab frame the 4-momentum of the detected hadron is given by:

$$\begin{aligned} p_h &= (E_h, \vec{p_h}) \\ &= (E_h, \vec{p_l} + \vec{p_t}) \end{aligned} \tag{1.10}$$

Other useful leptonic variables that have not defined yet are: the scaling variable x_b is given by

$$x_b \equiv \frac{Q^2}{2p \cdot q} \overset{lab}{=} \frac{Q^2}{2M\nu} \tag{1.11}$$

which can be interpreted in the Breit frame as the fraction of the nucleon taken the struck quark, in the cases of inelastic collision $0 < x_b < 1$; and the scaling variable

$$y_b \equiv \frac{p \cdot q}{p \cdot k} \overset{lab}{=} \frac{\nu}{E} \tag{1.12}$$

which is interpreted as the fraction of energy exchanged between the lepton and the hadron systems.

The following are the variables which involve the hadron. First, Z_h which represents the fraction of the energy of the virtual photon and is defined as

$$Z_h \equiv \frac{p \cdot p_h}{p \cdot q} \overset{lab}{=} \frac{E_h}{\nu}. \tag{1.13}$$

There are two angles that describes the direction of the outgoing hadron momentum in relation to the virtual boson. One is ϕ_{PQ}, which measures the angle between the leptonic and the hadronic plane (see Fig 1.7) and the other is the polar angle θ_{PQ}, which have the following form

$$\cos(\theta_{PQ}) = \frac{\vec{q} \cdot \vec{p_h}}{|\vec{q}||\vec{p_h}|}. \tag{1.14}$$

Using this angle, the transverse momentum squared with respect to the direction of the virtual photon $|\vec{p_t}|^2 \equiv P_t^2$ (see Eq 1.10) can be written as

$$P_t^2 = |\vec{p_h}|^2(1 - \cos^2(\theta_{PQ})) \tag{1.15}$$

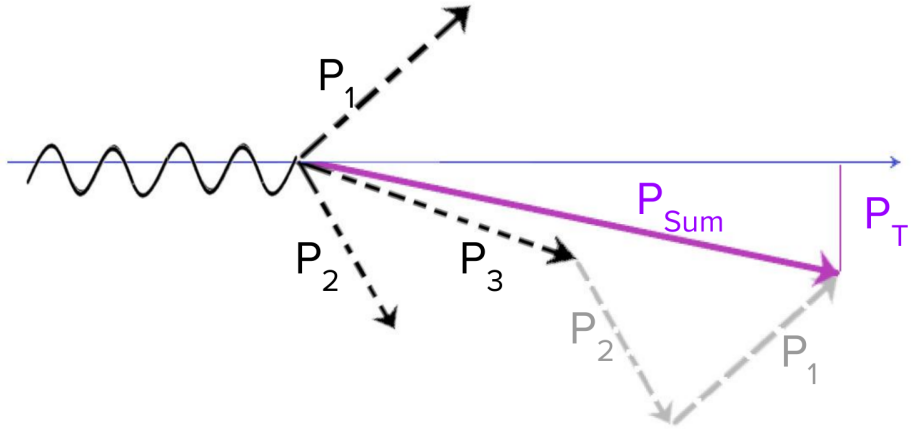

Figure 1.8: Schematic representation of the momentum vector sum in a event with multiple-pions in the final state.

1.5 Observable definition

The observable studied in this analysis is the average transverse momentum broadening for a multiple-pion final state. This observable is related to the induced energy lost and is defined as the difference between the mean of the square transverse momentum (P_t^2) for particles produced in nuclear media (A) and deuterium (D). In this analysis, we defined the transverse momentum of the event by taking the vector sum of the positive pion's momentum (see Fig. 1.8) and then calculated the transverse component of this vector in relation to the virtual photon. From now on, P_t^2 and ϕ_{PQ} will refer to this vector sum. So the formula for the transverse momentum broadening is:

$$\Delta P_t^2 = \langle P_t^2 \rangle_A - \langle P_t^2 \rangle_D$$

where $\langle P_t^2 \rangle_{A/D}$ represents the mean of P_t^2 for one of the solid target, and deuterium respectively. The results are shown as a function of Zh_{Sum}, which is the sum of the Z_h for all the positive pions in the event. From now on, the phrase "n pion event" refers to events where n positive pions were detected.

The vector sum was taken because it represents how much momentum did not come from the photon exchange.

1.5.1 Previous measurements

The transverse momentum broadening for multiple pion events has not bean measurd before; however, the measurement had been done for single charge pion events by the HERMES collaboration [6]. They performed experiments with electron and positron beams, with 27.6 GeV of energy, incident on deuterium, helium, nitrogen, krypton, and xenon. Their results show that the broadening increases with the size of the target and it vanishes at $Z_h \to 0$ (see Fig. 1.9).

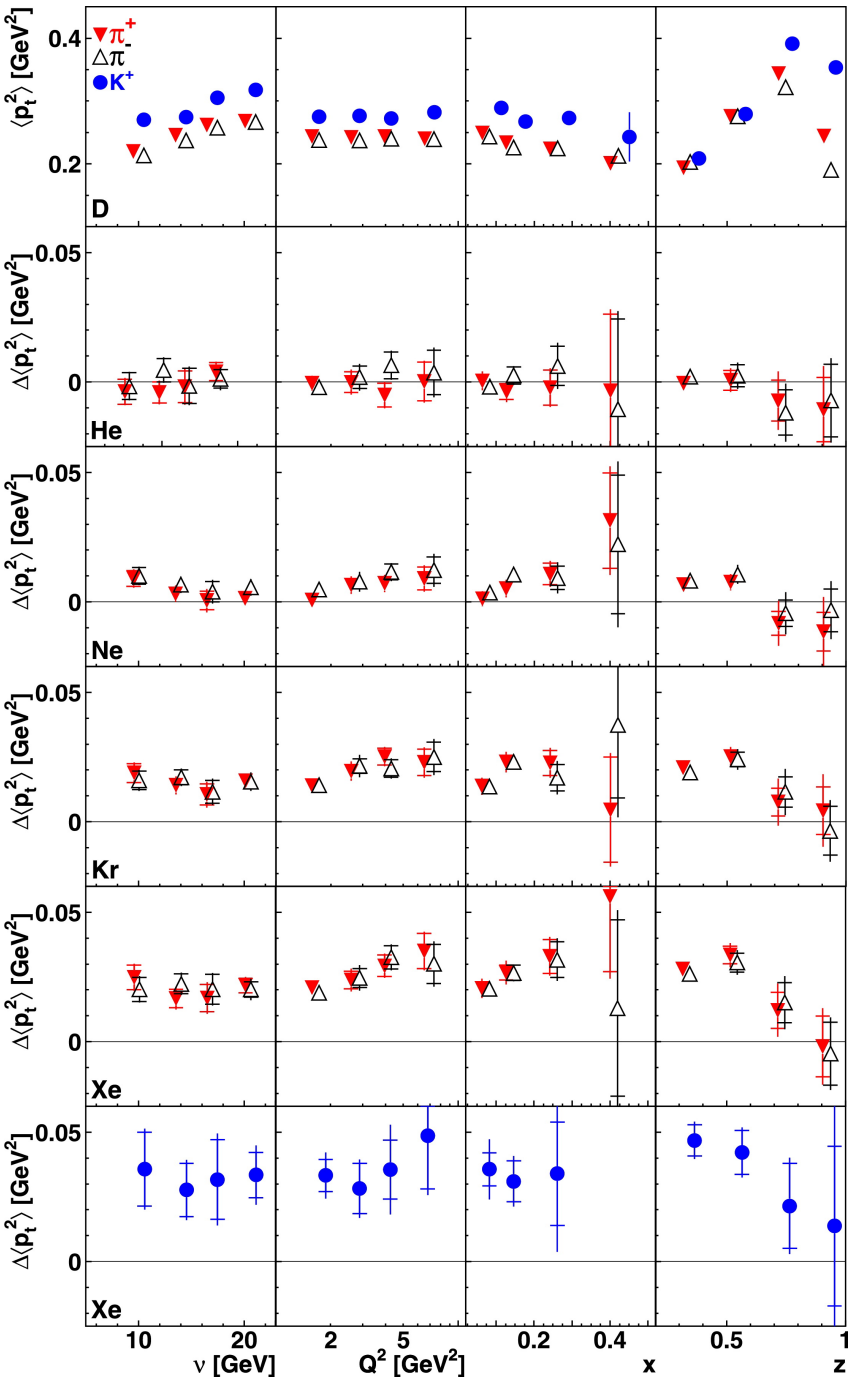

Figure 1.9: HERMES transverse momentum broadening measurements.

Chapter 2

Experimental Setup

This chapter summarizes the experimental setup used to collect the data analyzed in the thesis. The experiment occurred between January and March 2004 in the Thomas Jefferson Accelerator Facility (TJNAF), commonly called Jefferson Lab.

This laboratory is located in Newport News, Virginia, USA, and its focus is the high energy physics experiments to study nuclear physics. Jefferson Lab has a linear electron accelerator called CEBAF and four experimental stations called Hall A, B, C, and D; being Hall B, in which the experiment occurred (see Fig 2.1).

2.1 CEBAF

The Continuous Electron Beam Accelerator Facility (CEBAF) is built 8 meters below the Earth's surface. It consists of a polarized electron source and injector and a pair of superconducting RF linear accelerators (LINAC) connected by two recirculation arc sections that contain steering magnets [7] (see Fig 2.2).

Each LINAC has a length of 1.4 km and is formed by 20 cryomodules. Each comprises superconducting niobium cavities that boost the beam with RF waves and are in constant contact with liquid helium to keep it at ~ 2 K. The arc sections are composed of four and five individual arcs. These have a radius of 80 meters, which is large enough to decrease the energy loss of the electrons due to synchrotron radiation.

The accelerator works as follows; First, the injector produces an unpolarized electron beam of 45 MeV. This beam enters the north LINAC, where it should be accelerated up to 0.6 GeV, then the electrons go through one of the recirculation arcs and enter the

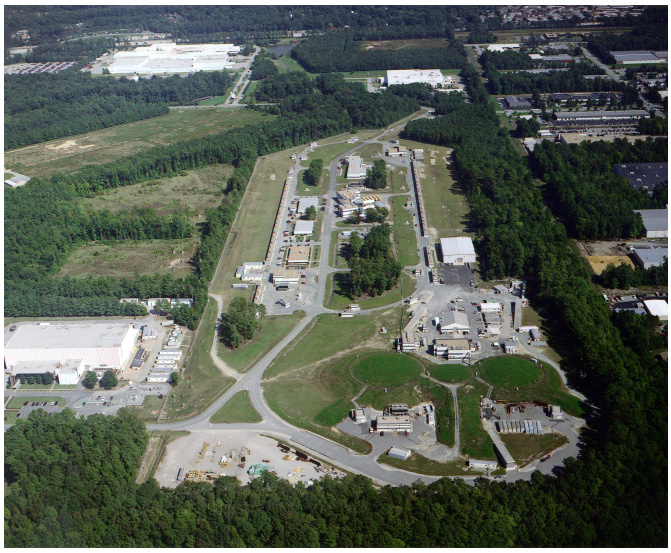

Figure 2.1: Aerial view of Jefferson Lab

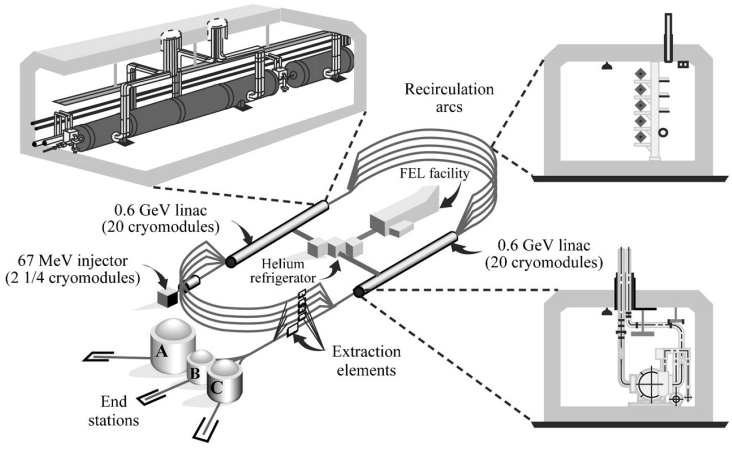

Figure 2.2: Representation of CEBAF accelerator

south LINAC. This process is repeated until electrons complete up to five cycles and reach ~ 6 GeV. Finally, the beam is delivered to one of the halls.

Nowadays, after an upgrade, the beam can reach up to 12 GeV, and the luminosity is bigger.

2.2 CLAS

The CEBAF Large Acceptance Spectrometer(CLAS) was the principal detector of Hall B. The main feature of CLAS is that it provided almost 4π acceptance in solid angle. Relative to the direction of the beam line, the detector covered angles from 8° to 140° for charged particles and from 8° to 75° for neutral particles, and for the azimuthal coordinate, the detector covered all the possibles angles, with just six gaps due to the magnetic coils. These values made the detector very good for the study of multiple-particles final states.

CLAS was designed based on a toroidal magnetic field generated by six superconducting coils arranged around the beam line. This field bent the particles only in the polar direction. The main ideas for this design were the capacity to measure the momentum of charged particles with high resolution, the geometrical coverage mentioned above, and keeping the region around the target without a magnetic field to allow the use of dynamically polarized targets [8]. The coils that generated the magnetic field divided the detector into six identical sectors. Each of these worked as an independent spectrometer but shared the same target, trigger, and data acquisition system.

Additionally, between the target and the first part of the detector system, there was located a second magnet, smaller than the principal, that helped to deflect electrons produced by Møller scattering. Also, at the end of the beam line, there was a Faraday Cup to collect the non-scattered electrons.

The particle detector system consisted of drift chambers to determine the trajectories of charged particles, gas Cherenkov counters for electron identification, scintillation counters for time-of-flight measurements, and electromagnetic calorimeters to detect showering particles (see Fig 2.3).

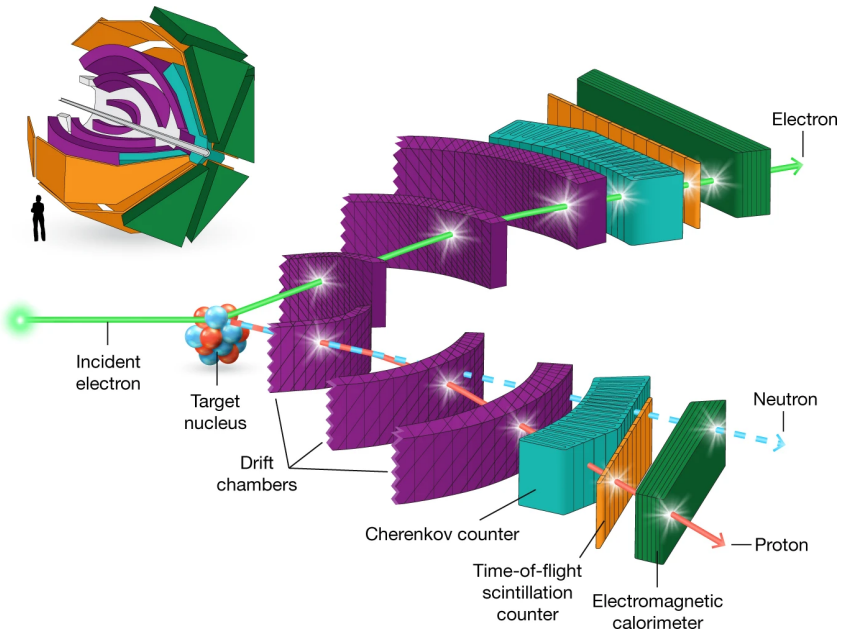

Figure 2.3: Schematic view of CLAS Detector, its components and the trajectory of the particles (Fig taken from [9])

2.2.1 Drift Chambers

The first detector that the particles encountered on their way after the scattering are the drift chambers (DC). DC were placed to determine the trajectory of charged particles with momentum bigger than 200 MeV with a precision of 0.5%, covering polar angles between the 8° and 140° and 80% of the space in the azimuthal direction [10].

In each sector of CLAS, there were three DC called regions, making a total of 18 DC. Each DC was formed by superlayers of wires, the first region consisted in four superlayers and the others in two superlayes. Each superlayer was made of 6 layers of wire cells. Each cell had a hexagonal shape and consisted of one wire in the center (anode) and six wires surrounding it (cathodes), one in each vertex (see Fig 2.4). One of the superlayers was in the direction of the magnetic field and the other was rotated 6° respect to the other. This allowed the determination of the azimuthal angle.

DC is a type of detector that works based on the ionizing effect that high-energy particles produce when they move through matter (more information in [11]). In this case, the matter was a gas mixture of 90% Ar and 10% CO_2 that filled the cells. After the ionizing effect was produced, the electrons generated by this process drifted to the central wire of the cell. Once the electron was close to the anode, the electric field was strong enough to make the electron generate an avalanche of electrons that went to the

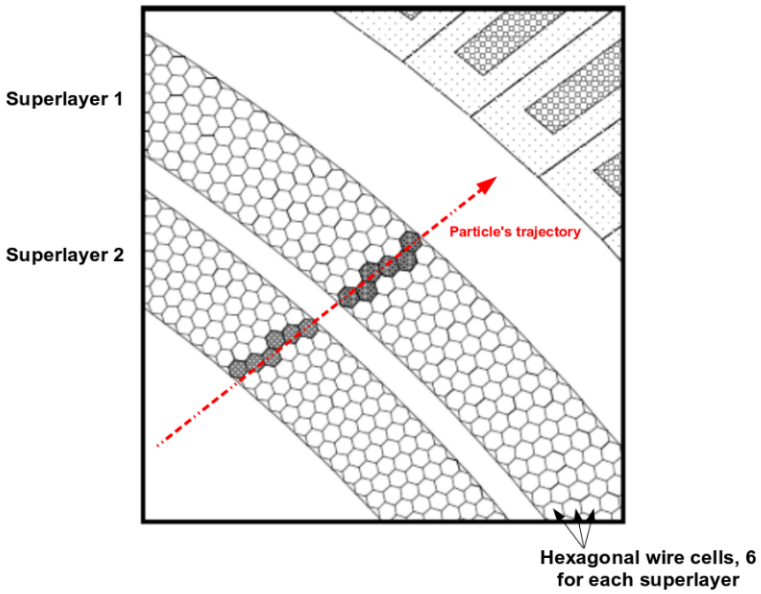

Figure 2.4: Representation of the superlayets and cells of a DC

wire and generated a measurable current.

The first region of the DC was the closest to the target; here, the magnetic field was weak and so it was used to determine the initial direction of the particle. The second region was between the magnetic coils, so the magnetic field was strong and was used to determine the maximum curvature of the particle track. In the last region, there was no magnetic field, and it determined the final direction of the particle.

2.2.2 Cherenkov Counters

The second set of detectors was the Cherenkov Counters (CC). CC had two essential functionalities. The first was the differentiation between electrons and negative pions with momentum smaller than 2.5 GeV, and the second was its role in the trigger electron system [12]. CC covered all the space in the azimuthal direction and between 8° and 45° on the polar angles.

Cherenkov counters, as its name implies, work detecting Cherenkov radiation. This radiation is the electromagnetic waves emitted by charged particles when they move faster than light in some medium. The Cherenkov counters are filled with gases with a high refractive index to induce this process. In the case of CLAS, the CC were filled with perfluorobutane (C_4F_{10}), which has a refractive index of $n = 1.00153$. Typically an electron going through the detector resulted in 4-5 photoelectrons.

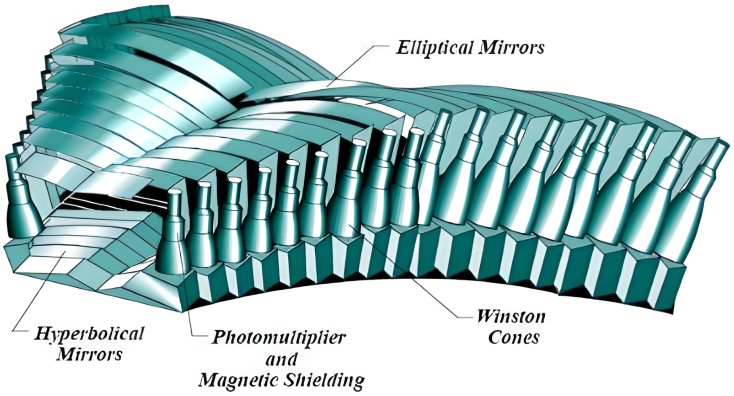

Figure 2.5: Schematic view of the exterior of CC

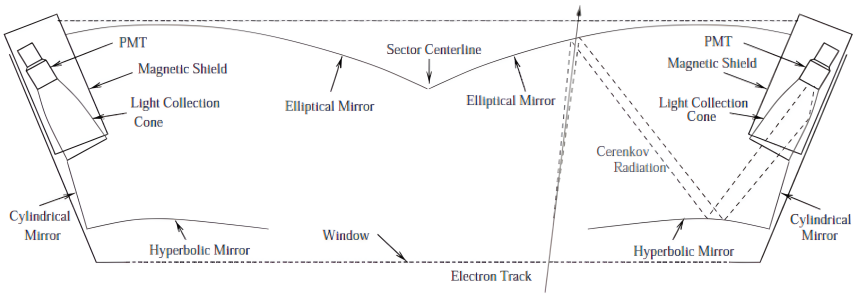

Figure 2.6: Schematic view of the interior of a CC

Due to the form of the magnetic field, charged particles moved approximately in a constant azimuthal angle. Because of this, the light collection system was designed to focus the light in the azimuthal direction. Thus, each sector of CLAS was divided into eighteen regions in the polar direction (see Fig 2.5). Each region consisted of a set of mirrors, two light collection cones, and two photomultiplier tubes (PMT) (see Fig. 2.6).

2.2.3 Time of Flight Counters

Looking in the radial direction, the third type of detectors were the Time of Flight (TOF) counters, which are a set of Scintillation Counters(SC). The primary purpose of TOF was particle identification. They covered angles between 8° and 142° on the polar angles, all the space in the azimuthal direction, a total area of 206 m^2, and they had an average time resolution of 163 ps for electrons[13].

TOF refers to the time it takes a particle to go from the point of interaction in the target to the TOF system. This value allowed the calculation of the particle's velocity,

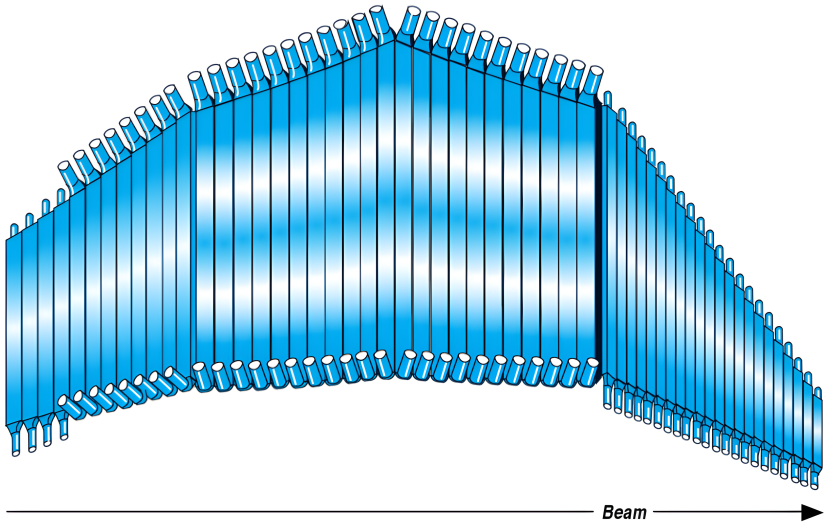

Figure 2.7: Schematic view of the TOF counters

which, in conjunction with the measurement of the momentum done by DC, allowed the calculation of the particle's masses.

Scintillation counters detect the light that certain materials emit when a high energy particle strikes them. This material is coupled to a photomultiplier, which converts the photons into an electrical signal.

In CLAS there were a total of 342 organic plastic scintillators, with a PMT at each end; this means 57 for each sector of CLAS. The lengths of the counters ranged from 32 to 445 cm, and they were situated to be perpendicular to the average trajectory of the particles (see Fig 2.7).

2.2.4 Electromagnetic Calorimeters

The last region of CLAS was the Electromagnetic Calorimeters (EC), having three main goals. First detecting and triggering electrons at energies above 0.5 GeV, second detecting photons at energies above 0.2 GeV to allow the reconstruction for neutral pions and eta particles, and third detecting neutrons [14]. The EC covered the azimuthal region between 8 and 45°. There was a second detector in two sectors, which extended up this range to 75°. EC also covered the entire range in the azimuthal angles as the rest of the detectors.

Electromagnetic calorimeters work by collecting the energy deposited by electrons and photons. These particles (also positrons) create electromagnetic showers, which scintillators can detect. Hadrons lose energy mainly via ionization, and the signal generated

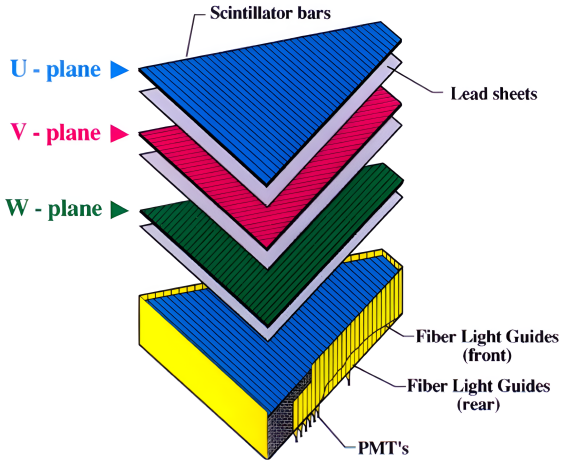

Figure 2.8: Schematic view of a EC module and the layers

by this process is very different from the one that comes from showers. This difference made possible the differentiation between electrons and pions with energies bigger than 2.5 GeV, which CC could not distinguish.

The EC were made of layers, each consisting of a 10 mm thick scintillator followed by lead sheets of 2.2 mm. The lead worked as an absorber that induced electromagnetic showers. Scintillators were composed of 36 parallel scintillator strips; this gave them an orientation. The shapes of the EC were triangular modules (one for each CLAS sector) made of 39 layers that increased as they got farther from the target. Each layer was rotated 120° with respect to the last one, generating three planes of orientation called U, V, and W (see Fig 2.8). This generated 13 complete layers per sector. Finally, each module required 216 PMT.

In order to improve the distinction between hadrons and electrons, the 13 complete layers were divided into two groups, the inner five layers and the other outer eight. The energy stored in the inner group is denoted as E_{in}, and the energy stored in the outer group is called E_{out}. Another important fact is that the ratio between the energy deposited in the EC and the total energy of the particle was around 0.27; this factor is called the sampling fraction.

2.3 Double target system

The EG2 Experiment was the experiment from which the data analyzed in this thesis comes. The scattering studied was the DIS between an electron and a nucleus. The main goal of the experiment was to study the hadronization process. This is the process through which quarks and gluons form hadrons. The experiment was divided into three runs with different beam energies. Only one run was analyzed because that run had an energy beam of 5.014 GeV, which is the lowest energetic limit for a good study of quark propagation.

The design of the experiment was based on a double target system in which two targets were exposed to the beam simultaneously. The first was a cryogenic liquid deuterium or hydrogen target, which had a length of 2 cm, and it was called the Liquid Target (LT). The second was a Solid Target (ST) that changed between Carbon (C), Aluminium (Al), Lead (Pb), Iron(Fe), and Tin (Sn), but only the data or C, Fe, and Pb was analyzed on this thesis because there were events for these targets. ST had a circular form of 0.15 cm of radius, and their lengths can be seen in Table 2.1. These lengths were selected to try to have the same number of nuclei for each target, except for the Pb, which had a reduced length to decrease the background. Also, the lengths had to be less than 2-3% of the radiation length of any target material to suppress secondary electromagnetic processes. The ST was placed in $Z = -25$ cm and the liquid target in $Z = -30$ cm, where $Z = 0$ is the center of CLAS and grows in the beam direction. This location was selected to improve the acceptance of negative charged particles, which bend inward due to the magnetic field polarization during the experiment. The full details of the double target mechanism can be found in [15].

Target	length (cm)
C	0.17
Fe	0.04
Pb	0.014

Table 2.1: Thickness of the ST

The main idea of the double target system is the precise comparison of elementary targets, such as deuterium, to heavy solid targets to study subtle medium effects, such as transverse momentum broadening, color transparency, and hadron attenuation. The advantage of this target location was that both targets were positioned in the beam

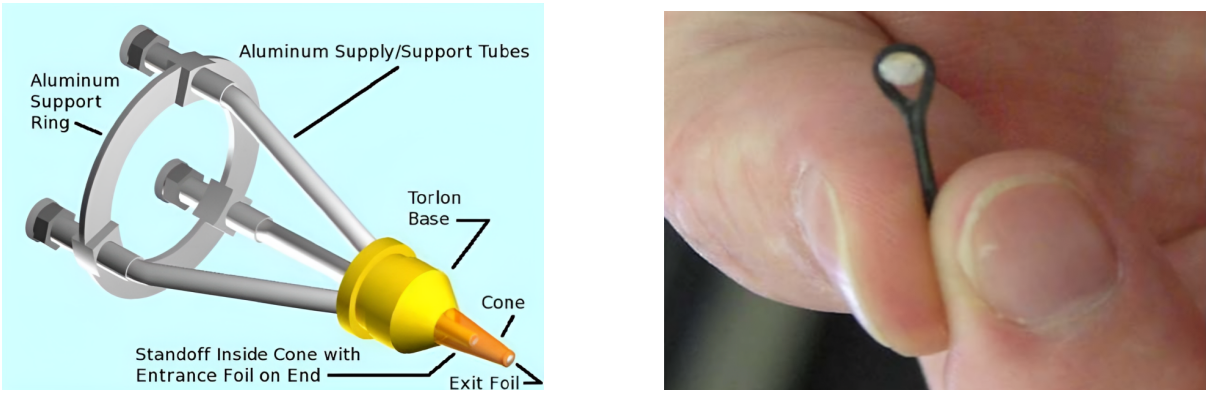

(a) (b)

Figure 2.9: In Figure (a) is a representation of the LT system and Figure (b) shows a picture of a ST

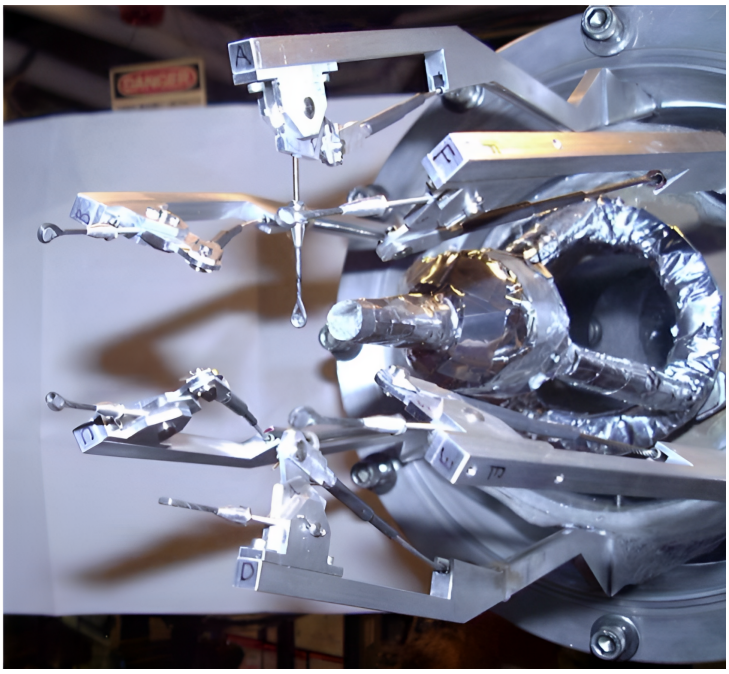

Figure 2.10: Photograph of the double target system.

simultaneously. This reduces sources of time dependent systematic errors related to inefficient detector channels or the beam, like the luminosity. These will be canceled approximately in ratios of observables.

Chapter 3

Data Analysis

For the study of the observable, it is necessary to take the signals collected by the different detectors of CLAS and identify them as particles. This was done by applying cuts, which are a set of rules that some variables must obey to be identified as a specific particle with enough certainty. The cuts applied in this thesis were taken from Sebastian Moran's analysis note [16].

After that, acceptance corrections, radiative corrections, and background subtraction were applied. Finally, the transverse momentum broadening was measured with the corrected data.

The data analysis was done with the ROOT framework for C++ and Python to the plots.

3.1 Data taking

From all the signals collected by CLAS, only the ones that passed the triggering system were saved. This system consisted of two levels. The first was detecting a coincident signal between the EC, CC, and TOF, which could be associated with a possible electron. The second level looked for possible tracks in the information collected by the DC; if possible candidates were detected, the event was saved. All the events that pass the triggering system were transferred to the tape silo and saved in the data system of Jefferson Lab.

After the data were collected, it went through the reconstruction process known as *cooking*, which was done with a software called RECSYS. The cooking process used in this analysis is called *pass2* . Once this process was done, the data were stored in ROOT

files in Bank Object System (BOS) format. Here the more important is the EVNT bank, which contains the four momentum vector of the reconstructed particles and links to the signal left in each detector. These files were analyzed using the ClasTool package for C++.

3.2 Particle identification

The relevant particles for this analysis were the electrons and the positive pions. Electron identification is essential because only events where an electron was reconstructed were considered valid for the analysis. The positive pions were important because they are involved in the observable studied in the thesis.

Particles were identified by applying cuts to the raw data. This section aims to show these cuts and why they were selected. The cuts were applied for different reasons:

- Correct the signal of the detector.
- Reject some contamination in the sample.
- Eliminate some regions where the detectors have efficiency problems; these last are called fiducial cuts.

The plots shown in this section were made with a representative subset of the carbon data, but all the fits were made with all the data.

3.2.1 Electron identification

The candidates for electrons are the ones that obey the following rules. They must be in the first track in the EVNT bank because the cooking process added in the first place the particle that most probably triggered the event. The particle must also have left a track in all of the detectors. Additionally, the particle must have passed the Time Based Tracking (TBT) and the Hit Based Tracking (HBT) during the reconstruction. Naturally, the charge of the particle must be negative, The particle's charge was determined by the bending direction in the DC due to the magnetic field.

The fiducial cuts applied were two. One was applied to some regions of the DC, these cuts were developed by L. Zana, and the full description can be found in Ref [17]. These

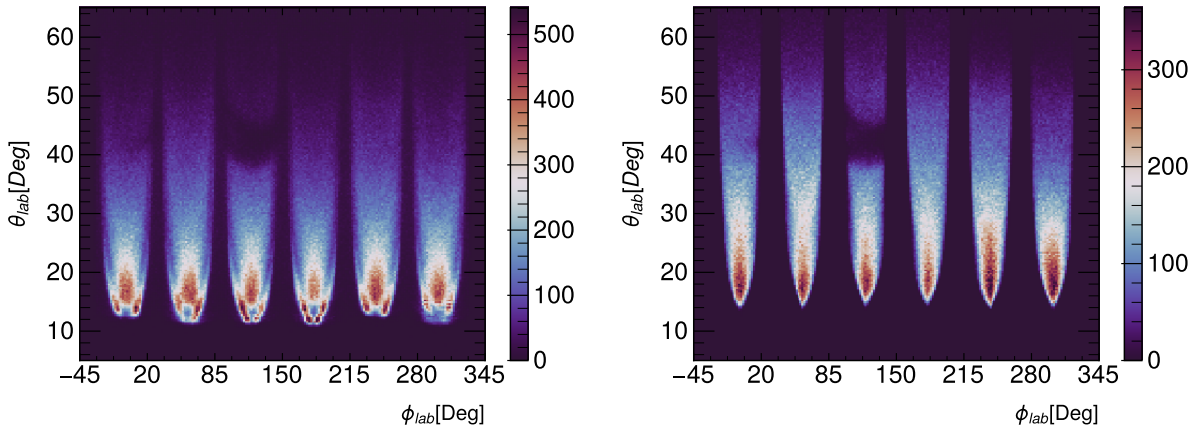

(a) With out cuts

(b) DC fiducial cuts applied

Figure 3.1: ϕ_{lab} vs θ_{lab} phase space. In (a), all the electrons candidates, and in (b), the electrons candidate not rejected by the DC fiducial cuts.

cuts depend on the momentum and the angular coordinates. The events rejected by these cuts can be seen in Fig 3.1.

The other fiducial cuts were applied on EC. Since the electromagnetic showers could not be well measured in the edges of the EC; therefore, it will give an incorrect value of the deposited energy. To avoid this the cuts shown in Eq. 3.1 were applied, where the U, V, and W are the coordinates perpendicular to the edges of the EC layers. These cuts can be seen graphically in Fig 3.2.

$$40\ cm < U < 410\ cm \qquad V < 370\ cm \qquad W < 405\ cm \tag{3.1}$$

At this point, the principal problem was the contamination of other particles. The particles that contributed the most to the contamination were negative pions. One way to discriminate between these and the electrons is by looking at the number of photo-electrons (Nphe) collected by the CC. The electrons went through the CC near the speed of light; this implies that they should not generate a small Nphe. On the other hand, negative pions are heavier, so they went slower and generated less Nphe. Due to this, a sector dependent cut in the Nphe was applied. The cuts for each sector can be seen in Fig 3.3.

Other cuts applied to decrease the negative pion contamination were based on the energy deposited in the EC. Using the variables E_{in} and E_{out} (see Sec 2.2.4), the cuts applied are the following. The energy deposited in the outer layers of the EC must be

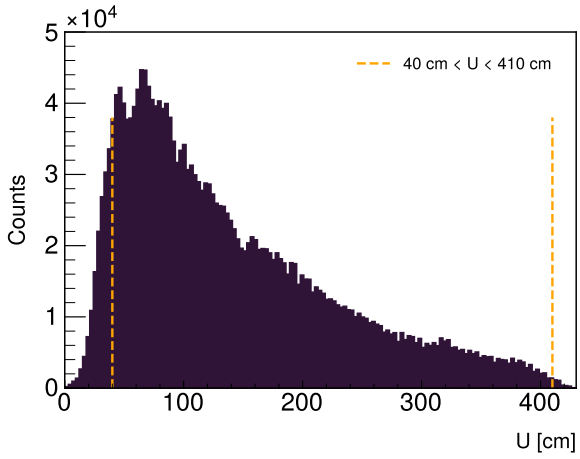

(a) U distribution

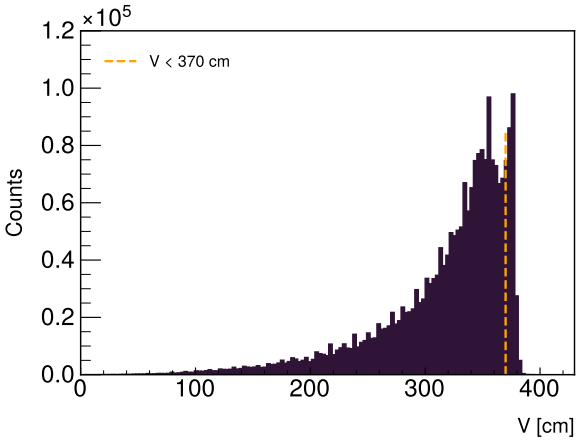

(b) V distribution

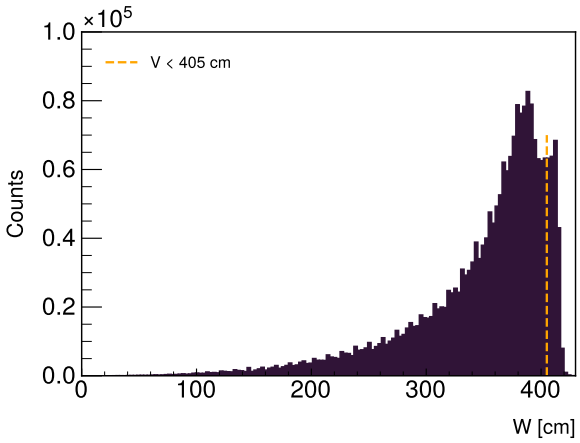

(c) W distribution

Figure 3.2: U, V , W distributions; in orange, the applied cuts

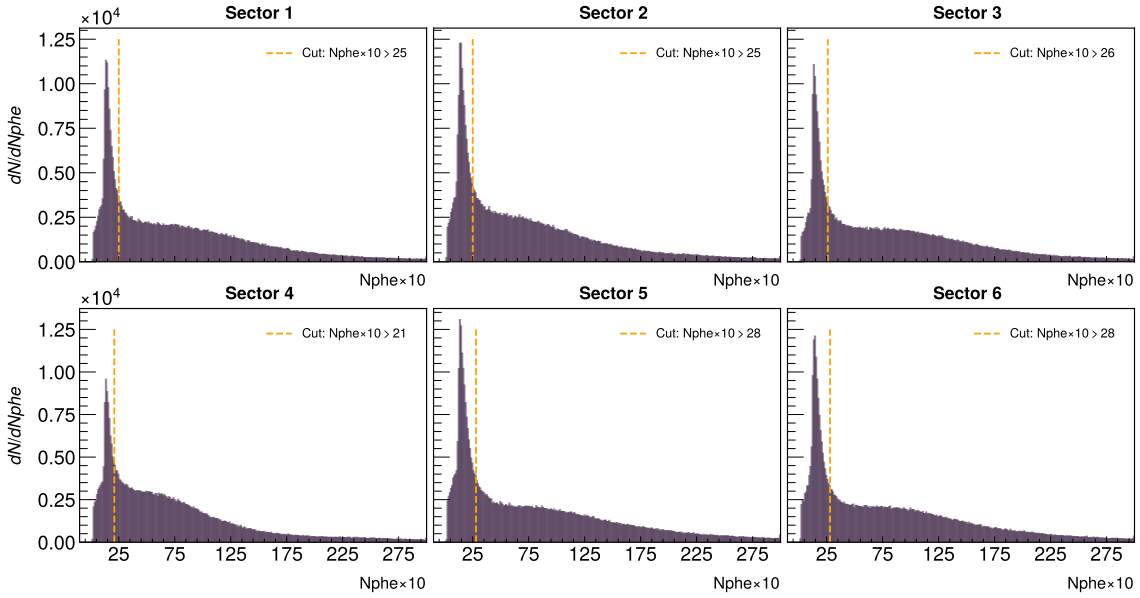

Figure 3.3: Number of photo-electrons (x10) distribution for the electron candidates. In orange, the cuts that were applied to reduce the negative pion contamination.

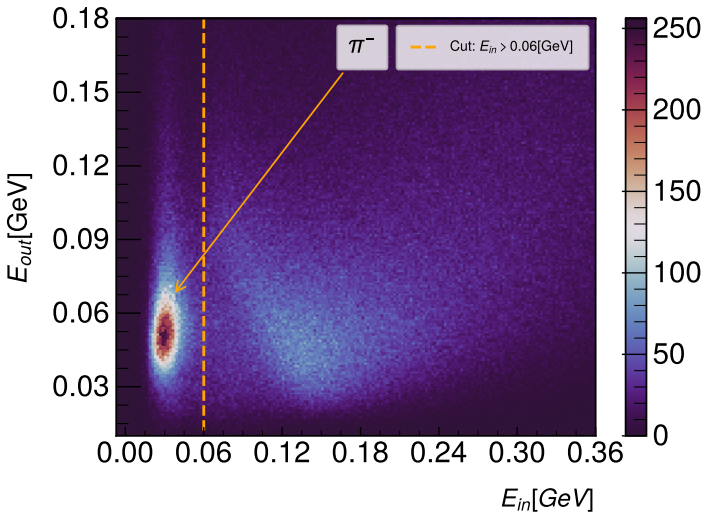

Figure 3.4: E_{out} vs E_{in} distribution for the electron candidates. The orange dashed line is the cut on the E_{in}. All the events at the left of the cut were rejected

Sector \ Cut	Upper cut	Lower cut
1	$E'_{tot} < 1.05 \times P + 0.18$	$E'_{tot} < 1.05 \times P - 0.46$
2	$E'_{tot} < 1.05 \times P + 0.18$	$E'_{tot} < 1.05 \times P - 0.46$
3	$E'_{tot} < 1.11 \times P + 0.18$	$E'_{tot} < 1.11 \times P - 0.43$
4	$E'_{tot} < 1.07 \times P + 0.18$	$E'_{tot} < 1.07 \times P - 0.43$
5	$E'_{tot} < 1.11 \times P + 0.18$	$E'_{tot} < 1.11 \times P - 0.43$
6	$E'_{tot} < 1.11 \times P + 0.18$	$E'_{tot} < 1.11 \times P - 0.43$

Table 3.1: Upper and lower limits for E'_{tot} as a function of the momentum. The events between the two cuts remain as electron candidates.

greater than zero, i.e., $E_{out} > 0$. Also, a peak associated with negative pions can be seen in low values of E_{in} (see Fig 3.4). The cut $E_{in} > 0.06$ GeV was applied to eliminate that problem.

The contamination was reduced even more by applying two extra sets of sector depend cuts in the energy deposited in the EC. These cuts were based on the idea that negative pions are often minimum ionizing, so the energy they deposited does not dependent on their momentum. One was a cut in E_{tot} divided by the sampling fraction factor, which is 0.27 (see Sec 2.2.4). This ratio will be denoted as E'_{tot} and the cuts can be seen explicitly in Table 3.1 and graphically in Fig 3.5a. The other cut was similar but was applied in the sum of E_{in} and E_{out} divided by the sampling fraction factor. Again the ratio will be denoted as $E'_{in/out}$. This cuts can be seen explicitly in Table 3.2 and graphically in Fig 3.5b.

Sector \ Cut	Upper cut	Lower cut
1	$E'_{in} + E'_{out} < 1.11 \times P$	$E'_{in} + E'_{out} < 0.75 \times P$
2	$E'_{in} + E'_{out} < 1.11 \times P$	$E'_{in} + E'_{out} < 0.75 \times P$
3	$E'_{in} + E'_{out} < 1.19 \times P$	$E'_{in} + E'_{out} < 0.84 \times P$
4	$E'_{in} + E'_{out} < 1.15 \times P$	$E'_{in} + E'_{out} < 0.83 \times P$
5	$E'_{in} + E'_{out} < 1.22 \times P$	$E'_{in} + E'_{out} < 0.85 \times P$
6	$E'_{in} + E'_{out} < 1.19 \times P$	$E'_{in} + E'_{out} < 0.84 \times P$

Table 3.2: Upper and lower limits for $E'_{in} + E'_{out}$ as a function of the momentum. The events between the two cuts satisfy remain as electrons candidates.

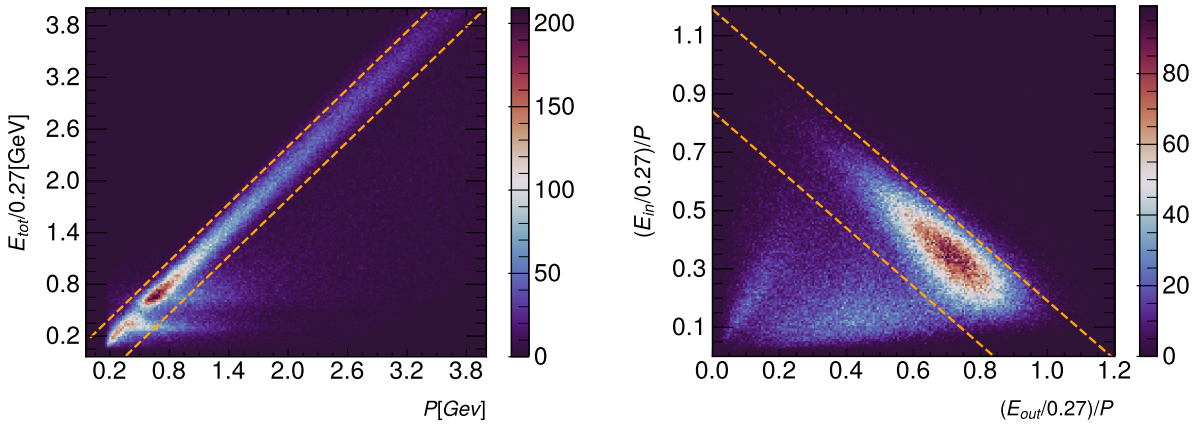

(a) (b)

Figure 3.5: (a) E'_{tot} vs P and (b) E'_{in}/P vs E'_{out}/P distributions for the electron candidates. The particles between the orange lines satisfy the cuts.

Cut / Sector	a_1	a_2	a_3	b_1	b_2
Sector 1	0.252164	0.0122263	-7.939e-04	9.5511e-03	3.4067e-02
Sector 2	0.278574	0.0187482	-0.0023821	1.3988e-02	3.7468e-02
Sector 3	0.262079	0.0230685	-0.0035474	9.3276e-03	2.9004e-02
Sector 4	0.251108	0.0201568	-0.0033236	8.2105e-03	2.9889e-02
Sector 5	0.263396	0.00955238	-0.0010203	2.2568e-02	3.0650e-02
Sector 6	0.255245	0.0232659	-0.0030479	1.1725e-02	3.6422e-02

Table 3.3: Parameters of the sampling fraction cuts for carbon data.

In reality, the sampling fraction factor is not a constant, it depends on the particle's momentum and the sector it hit. So to improve the cuts shown before, a sampling fraction cut was applied. The procedure consisted of taking the E/P distribution as function of P, where $E = max(E_{in} + E_{out}, E_{tot})$. Then fitting the mean value $\mu(P)$ and the width $\sigma(P)$ of the distribution. These functions have the form shown in Eq 3.2. The parameters for the carbon target can be seen in Table 3.3. The parameters for the other targets, as well as the details of the model of the functions and the fits, can be found in the Eg2 neutral pion analysis note developed by Taisiya Mineeva [18]. Finally, the cut had the form shown in Eq 3.3, and it is illustrated for each CLAS sector in Fig 3.6.

$$\begin{aligned} \mu(P) &= a_1 + a_2 \times P + a_3 \times P^2 \\ \sigma(P) &= \sqrt{b_1^2 + \frac{b_2^2}{P}} \end{aligned} \tag{3.2}$$

$$\left| \frac{E}{P} - \mu(P) \right| > 2.5 \times \sigma(P) \tag{3.3}$$

The final cut was applied in the variable ΔT_e defined in Eq 3.4.

$$\Delta T_e \equiv \left| (\text{Time}(EC) - \text{Time}(SC)) - \frac{1}{c} (\text{Path}(EC) - \text{Path}(SC)) \right| < 5 \times \sigma \tag{3.4}$$

where Time(EC/SC) is the time that it took to the particle to go from the vertex to the EC/SC, Path(EC/SC) is the distance traveled by the particle from the vertex to the EC/SC and $c = 30\ cm/ns$ is the speed of light.

After all the other cuts were applied, a Gaussian function was fitted to the ΔT_e distribution and a value of $\sigma = 0.35\ ns$ for the width was obtained. Finally, all the

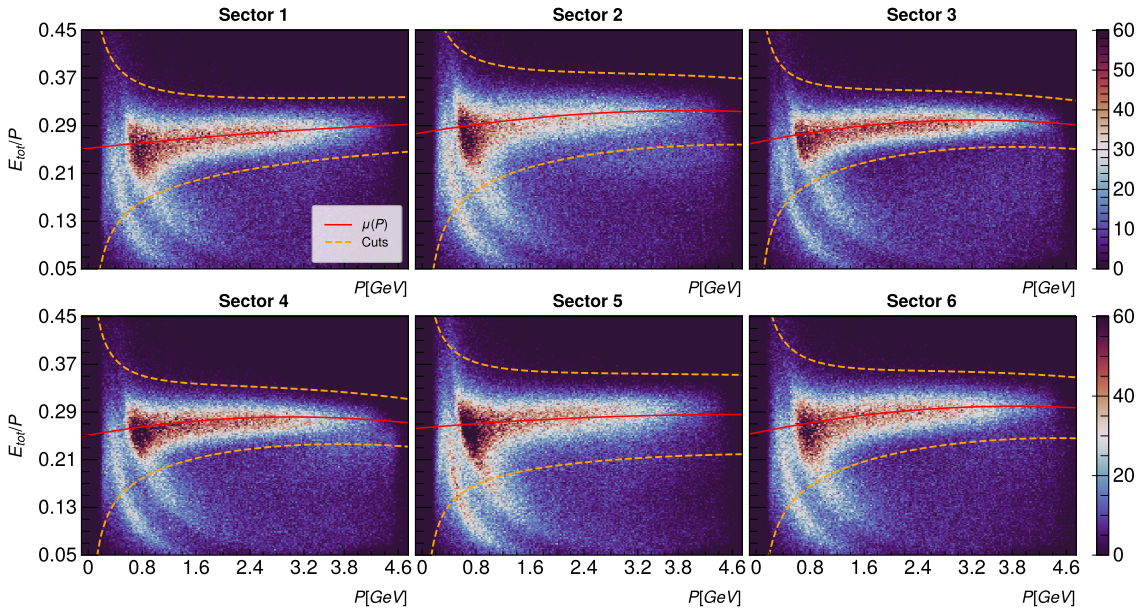

Figure 3.6: E/P vs P distributions for electron candidates. The red curve represent $\mu(P)$ and the orange curve represents $\mu(P) \pm \sigma(p)$ both for the carbon parameters

particles with $\Delta T_e > 5\sigma$ were rejected. The ΔT_e distribution can be seen in Fig 3.7.

3.2.2 Positive pion identification

Identifying the trigger electrons was only half of the work; another set of cuts was necessary to identify the positive pions.

The first criterion was that the particles must have passed the Time Based Tracking and Hit Based Tracking, and there must be a track in the DC. Also, the bending direction of the particles must be in concordance with positive charge particles.

Two different methods were used to discriminate between positive pions and other positive particles. One for particles with $P < 2.7$ GeV and the other for particles with $P > 2.7$ GeV.

3.2.3 Low momentum positive pions

For pions with $P < 2.7$ GeV, the first requirement imposed was to have a positive status in SC. Then the identification cuts were applied in the variable ΔT_π, which is defined as

$$\Delta T_\pi = \left(\frac{\text{Path}_e(SC)}{c} - \frac{\text{Path}_\pi(SC)}{v_\pi} \right) - (\text{Time}_e(SC) - \text{Time}_\pi(SC)) \tag{3.5}$$

where $\text{Path}_{e/\pi}(TOF)$ are the distance from the vertex to the TOF counters for the

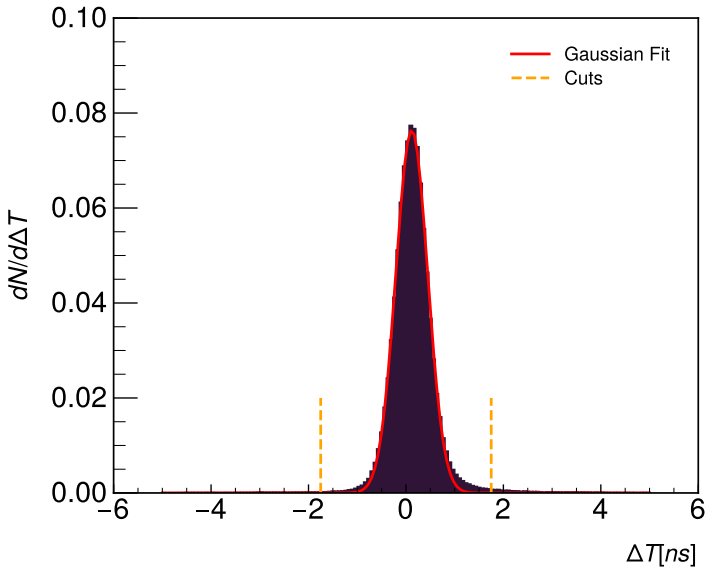

Figure 3.7: Normalized ΔT_e distribution for the electron candidates after all the other cuts were applied. The red curve corresponds with the fitted Gaussian function and the orange dotted lines represent the cuts on ΔT_e

electron and pion, respectively, v_π is the velocity of the pion candidate, and $\text{Time}_{e/\pi}$ are the time of flight from the vertex to the SC for the electron and pion respectively. The distribution of this variable can be seen in Fig 3.8.

This variable represents the difference in arrival time between the particle and a theoretical pion. The mean of this variable should be 0 for positive pions. Therefore, cuts around $\Delta T_\pi = 0$ were applied. These cuts depended on the momentum. The exact cuts can be seen in Table 3.4.

Besides the ΔT_π cuts, a cut in the mass squared (see Eq 3.6) was applied to reduce kaon contamination. This cut can be seen in Table 3.5.

P GeV	Lower limit	Upper limit
$[0.00 - 0.25]$	-0.70	0.70
$[0.25 - 0.50]$	-0.70	0.65
$[0.50 - 0.75]$	-0.70	0.65
$[0.75 - 1.00]$	-0.70	0.65
$[1.00 - 1.25]$	-0.55	0.55
$[1.25 - 1.50]$	-0.50	0.55
$[1.50 - 1.75]$	-0.50	0.40
$[1.75 - 2.00]$	-0.48	0.40
$[2.00 - 2.25]$	-0.50	0.40
$[2.25 - 2.50]$	-0.50	0.40
$[2.50 - 2.75]$	-0.50	0.40

Table 3.4: ΔT_π cuts for different momentum ranges

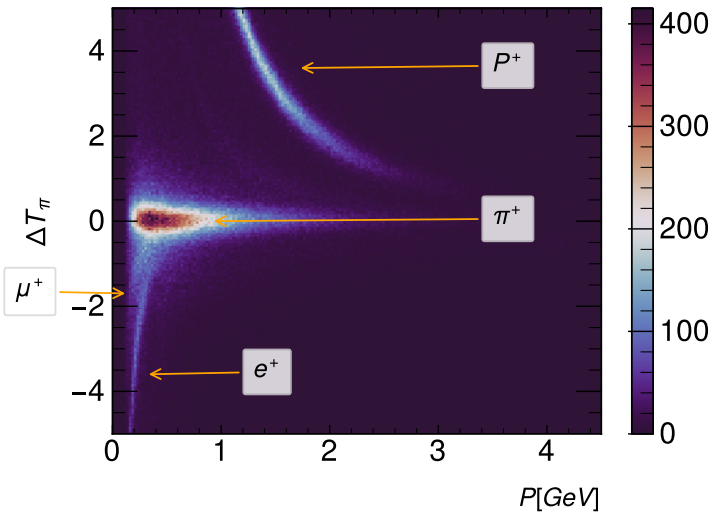

Figure 3.8: ΔT_π vs P distribution for positive particles

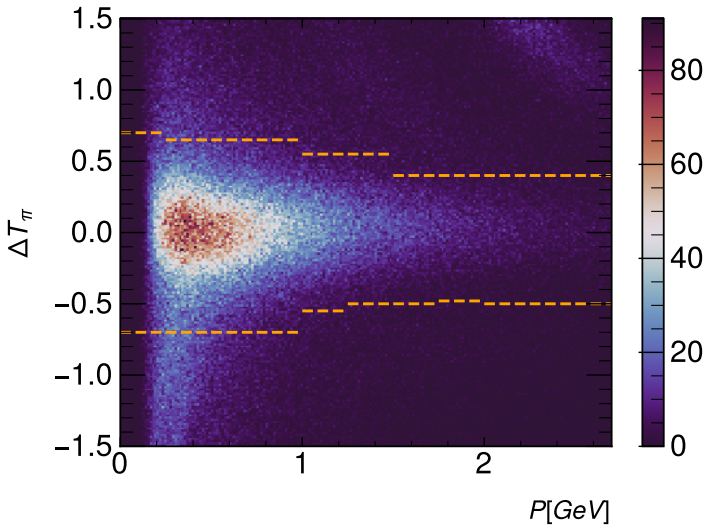

Figure 3.9: ΔT_π for positive particles, the orange lines represent the cuts, and each box is a different range of the momentum

P Ranges (GeV/c)	Upper Limit
$[2.25 - 2.50]$	0.5
$]2.50 - 2.70]$	0.4

Table 3.5: Mass squared limits for different momentum ranges

$$m^2 = p^2 \left(\frac{1}{\beta^2} - 1 \right) \tag{3.6}$$

3.2.4 High momentum pions

The second term in Eq 3.5 is calculated as:

$$\frac{\text{Path}_\pi(SC)}{v_\pi} = \frac{\text{Path}_\pi(SC)}{c} \sqrt{\frac{m_\pi^2}{p^2} + 1} \tag{3.7}$$

Hence, if the momentum increases, the square root on the right goes to 1 independent of the value of m^2. Due to this that another method for pion identification was required for high momentum pions.

In the case of particles with $P > 2.7$ GeV, the CC variables were used. The first necessary condition is a positive status in the CC data bank. Then a geometrical condition was imposed. This was a limit of 5° in the angle between the CC hit and the closest SC hit. The most crucial cut was $NPhe > 2.5$. This cut allows some positron contamination. To avoid this it was imposed that the particle must not obey the positron cuts, which are the same as the electron but with a positive charge. Finally the cut $\Delta T_\pi < 0.35$ was applied.

The particles that pass all the cuts can be seen in Fig 3.10.

3.3 Additional Cuts

In addition to the cuts for particle identification shown before, the following cuts were applied to reduce the noise and to dismiss some particles reconstructed badly.

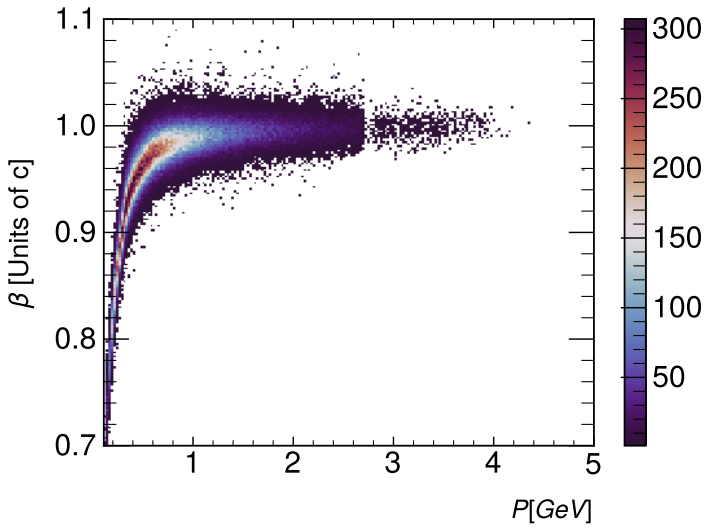

Figure 3.10: β vs P distribution for all the particles identified as positive pions

3.3.1 ΔZ Cut

Another source of contamination for positive pions that was not considered in the previous cuts came from the main decay mode of the pion (see Eq 3.8).

$$\pi^+ \rightarrow \mu^+ + \nu_\mu \tag{3.8}$$

MC studies resolve that about 18% of the decay in this mode during the flight. Often the anti-muon, which carries almost all of the momentum of the pion, is reconstructed as a positive pion but with a considerably different momentum.

This problem was fixed by applying a cut in ΔZ (see Eq. 3.9), which is the difference between the Z vertex of the pion and the electron (see Ref. [19]). The number of events rejected by this cut depending on the number of pion detected in the event can be seen in Tab. 3.6.

$$|\Delta Z| = |Z_{\pi^+} - Z_{e^-}| < 3 \text{ cm} \tag{3.9}$$

3.3.2 YC cut

The YC coordinate had worse reconstruction than the ZC coordinate due to the form of the DC stereo wires. Hence, a cut in YC was applied to reduce the background. The cut was developed by Orlando Soto, Raphael Dupré, and William Brooks.

N pions	C	Fe	Pb
1	12.1%	12.7%	13.1%
2	27.4%	28.0%	29.2%
3	43.2%	43.2%	47.42%

Table 3.6: Percentage of events dismissed due to the ΔZ cut depending on the number of detected pions.

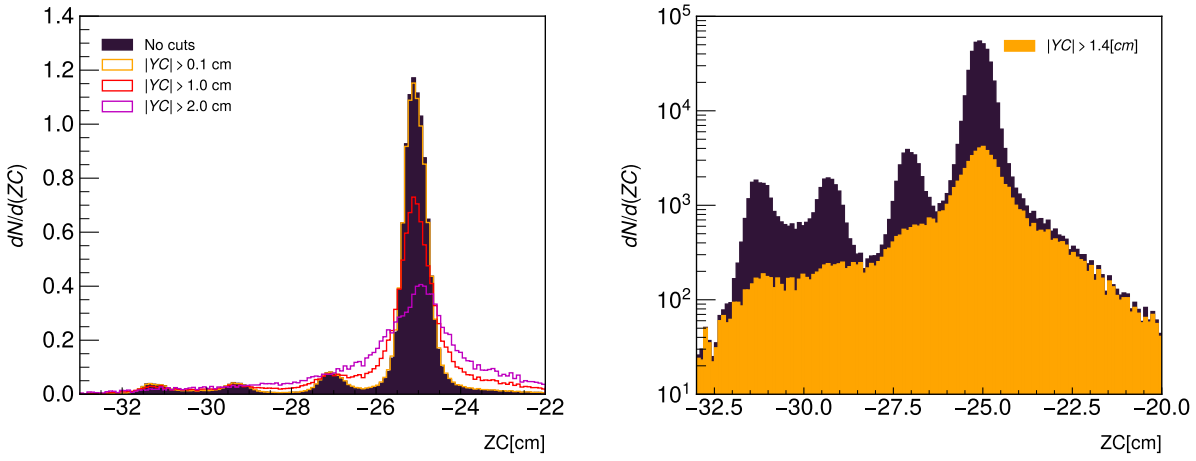

(a) (b)

Figure 3.11: Both figures represent the ZC distribution for electrons in a run with an empty target. In (a), the distributions are normalized, and there are different regions of YC. In (b), the orange distribution represents the event rejected by the cut.

In Fig 3.11a can be seen the ZC distribution for different regions of YC. In distributions without cuts, the peaks are distinguishable, but for $|YC| > 1.0$ cm, the small peak cannot be differentiated. Furthermore, for $|YC| > 2$, the peak is wide enough to make the vertex determination inconsistent, so if a cut were not applied, events for the different targets could be mixed. Finally, the cut applied was $|YC| < 1.4$ cm, removing almost all the background, as seen in Fig 3.11b. Even though this cut was applied, the aluminum foil can still be seen in the distribution, so the ZC cut was still necessary.

3.4 DIS region

In order to select the DIS events, the three cuts shown in Eq. 3.10 were applied. A representation of the cuts can be seen in Fig. 3.12.

$$Q^2 > 1\ GeV^2, \qquad W > 2\ GeV, \qquad y_B < 0.85 \tag{3.10}$$

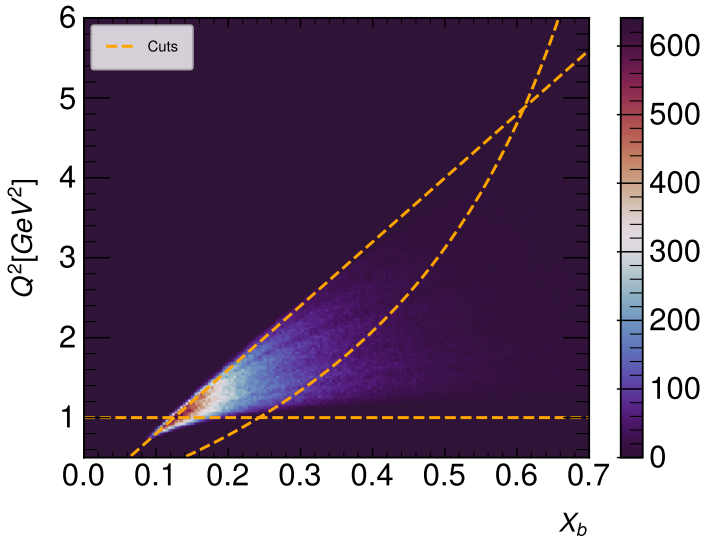

Figure 3.12: Q^2 vs X_B distribution. The orange curves correspond to the DIS cuts.

The Q^2 cut was applied to guarantee that the virtual photon had enough virtuality to resolve the inner structure of the nucleon. A W cut was selected to avoid nucleon resonances (see Fig 1.6), and y_B was chosen to limit the contribution of the radiative correction.

3.5 Vertex identification

In addition to the particle identification, another important factor to consider was determining whether the collision took place in the solid target or in the liquid target (see Sec 2.3). The cuts developed in Ref. [18] were used to determine the vertex of interaction. The procedure used to find the cuts is described below.

Considering that the beam was going in the $\hat{z}$ direction and that CLAS had its geometrical center at $Z = 0$, the center of the solid target was located in $Z = -25$ cm and the center of the solid target was located in $Z = -30$ cm. Sector dependent cuts in Z must be applied to identify the vertex of interaction. Nevertheless, when the experiment occurred, the beam was not perfectly located at $(x, y) = (0, 0)$ but was shifted. Actually, the beam position was $(x, y) = (-0.043, 0.33)$ cm. These position was calculated using electron-proton elastic scattering, which is a very well-known process. Considering these new centers the new corrected positions were calculated, and was named XC, YC, and ZC. The change in Z coordinate can be seen in Fig. 3.13.

As seen in Fig. 3.13a, after this procedure, the cuts in the ZC were independent of

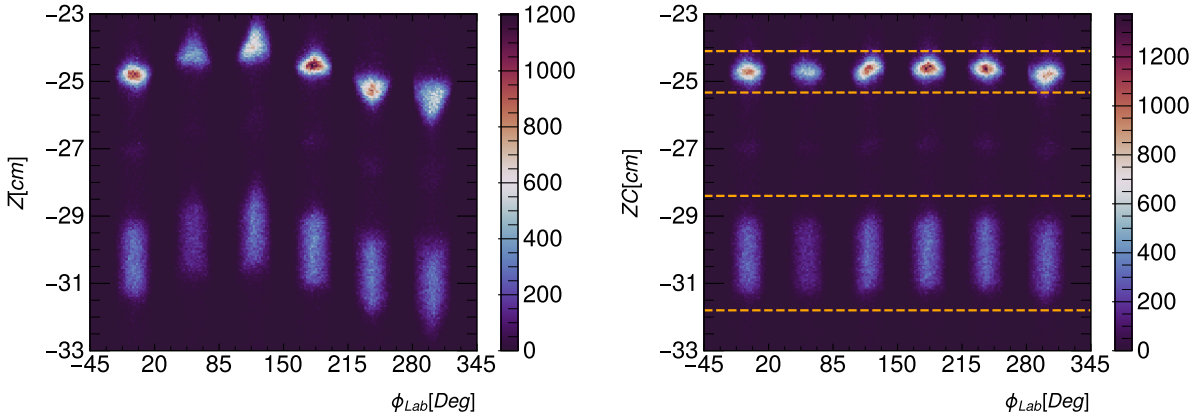

(a) Before correction

(b) After Correction

Figure 3.13: Z vertex vs ϕ_{lab} for electrons in carbon runs. In (a) before the correction and in (b) after the correction. The orange lines represent the cuts applied for vertex determination for carbon

Target	Range
D	-31.80 cm $< ZC <$ -28.40 cm
C	-25.65 cm $< ZC <$ -24.26 cm
Fe	-25.33 cm $< ZC <$ -24.10 cm
Pb	-25.54 cm $< ZC <$ -24.36 cm

Table 3.7: Cuts applied to ZC of the electrons to identify the vertex of the interaction

the sector. The final cuts for ZC variables were calculated by fitting a function around the approximate target, then cuts were selected using Eq. 3.11.

$$\langle ZC \rangle - 3\sigma_{ZC} < ZC < \langle ZC \rangle + 3\sigma_{ZC} \tag{3.11}$$

Where $\langle ZC \rangle$ is the mean of the fitted function and σ_{ZC} is the standard deviation. The cuts for each target can be seen in Tab. 3.7.

3.6 Zh_{Sum} Distribution

The principal results of Chapter 4 are shown as function of Zh_{Sum}. Logically, this variable is equal to Z_h for one pion events. However, for two pion events it is more complex. The behavior of the variable for two pions can be understood with Fig. 3.14.

The plot shows the distribution of Zh_{Sum} vs. Zh_1, where Zh_1 is the Z_h value of the most energetic pion in the event (the low energetic pion is denoted with Zh_2). The distribution is normalized separately for each bin of Zh_{Sum} meaning that each column

sums to one. There are no events in the dark grey region because the most energetic pion cannot have more energy than both pions. The light grey region is empty because the Zh_1 is related to the most energetic pion, so it has to have at least half of the energy of both pions. The bins near the dark grey area come form events that are the combination of pions with almost all the energy of both with other with low energy, while the closer the bins are to the light grey area, the energies of the pions are more similar.

It can be seen that besides the cases when one of the pions has a small fraction of the energy ($Zh_2 < 0.12$), all the combinations have a similar contribution. This means that events with two pions with close energies or events with pions with different energies have a similar probability of occurring.

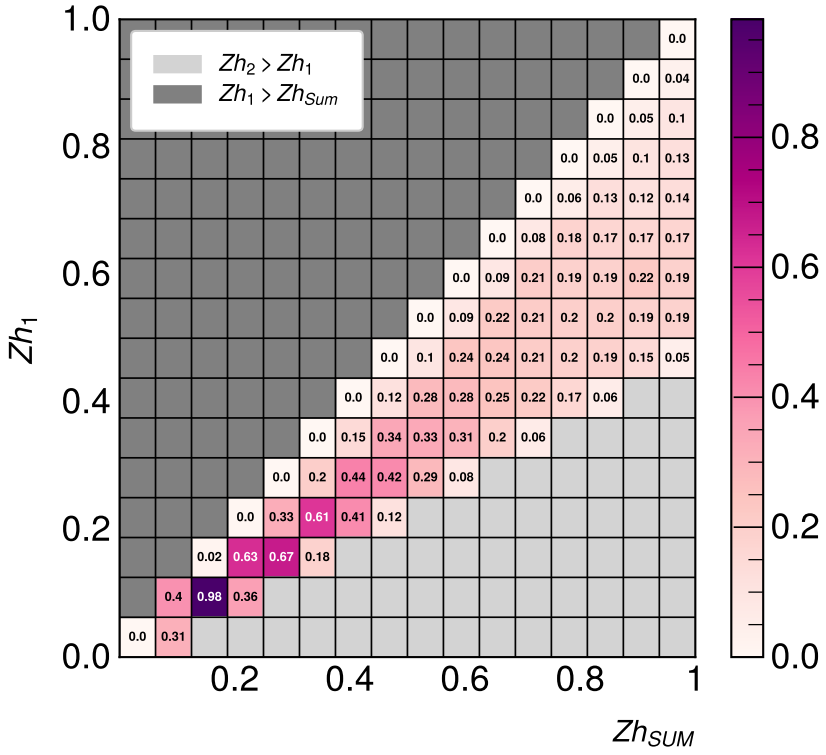

Figure 3.14: Zh_{Sum} vs Zh_1 distribution for all the events that came from the iron target. The distribution is normalized for each bin of Zh_{Sum} separately; this means that each column sums to one.

3.7 Binning

The binning used is in Table 3.8. The Q^2 and ν bins were selected to have approximately the same number of two pion events. It is useful to remark that the Q^2 and ν distributions

Variable	Binning
$Q^2[GeV^2]$	$[1, 1.32, 1.74, 4.00]$
$\nu[GeV]$	$[2.2, 3.36, 3.82, 4.26]$
Zh	[0.0, 0.1, 0.2, 0.3, 0.4, 0.5, 0.6, 0.8, 1.0]
$P_t^2[GeV^2]$	60 bins equally spaced between 0 and 3
$\phi_{PQ}[Deg]$	6 bins equally spaced between -180 and 180

Table 3.8: Binning used in the acceptance correction

are not equal for one and two pions events, especially for ν (see Fig 3.15). The P_t^2 and ϕ_{PQ} bins were selected equally spaced, and the number of bins was selected to have enough statistics in each bin. The exact binning is in Table 3.8. However, for $Zh < 0.1$, there are almost no two pion events, so the first bin studied in $0.1 < Zh_{Sum} < 0.2$

3.8 Acceptance correction

Particle detectors cannot detect all the particles generated in a collision, some of them get lost due to efficiency or geometrical reasons. The data was corrected using simulations to solve this issue. DIS events were generated with the Montecarlo simulator PYTHIA, and CLAS was recreated with Geant. For more details about the software and simulation settings, see [20].

3.8.1 Simulations

The number of events in the simulation depending on how many events were generated and reconstructed is in Tab. 3.9. Tab. 3.10 shows that according to the simulation, 14.6% of the events, where one pion was generated, one pion was reconstructed; for two pions this percentage decreases to 6.0%, and for three pions events the percentage is just 1.6%. On the other hand, Tab. 3.11 shows that 86% of the events in the simulation that were reconstructed as one pion events, came actually from an event in which one pion was generated. Of the other events reconstructed as one pion events 12.0% came from events where two pions were generated, but one was missed. For the cases of two pion events, 94% came from events where truly two pions were generated. For events where three pions events, just 64.9% came from events in which three pions were generated and, 31.1% came from events in which two pions were generated and the other signal came from the background.

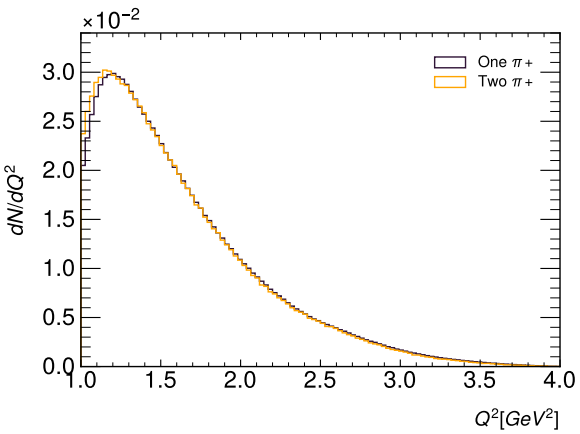

(a) Q^2 distribution

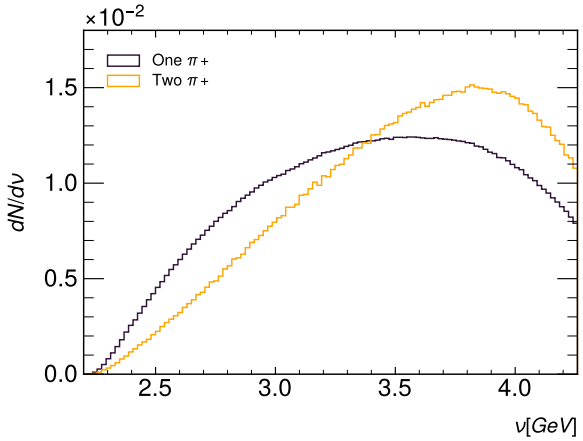

(b) ν distribution

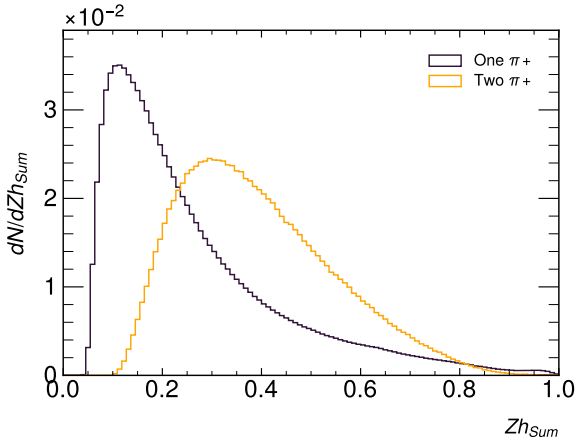

(c) Zh_{Sum} distribution

Figure 3.15: Q^2, ν and Zh_{Sum} normalized distributions for all the data in the carbon runs. In black, events where one positive pion was detected, and in orange, events where two pions were detected. There is a noticeable difference in ν and Zh_{Sum}. distributions

Rec \ Gen	0	1	2	3
0	-	4.93e+07	8.10e+06	1.27e+05
1	1.10e+05	8.41e+06	1.18e+06	1.22e+04
2	468	2.82e+04	5.92e+05	8.7e+03
3	1	136	1.07e+03	2.23e+03

Table 3.9: Number of events with positive pions in the iron simulation. Thrown columns represent how many positive pions were generated in that event, and rec row show how many positive pions were reconstructed in the event.

Rec \ Gen	0	1	2	3
0	-	85.4%	82.0%	84.5%
1	99.6%	14.6%	12.0%	8.2%
2	0.4%	0.1%	6.0%	5.9%
3	$\sim 0\%$	$\sim 0\%$	$\sim 0\%$	1.5%

Table 3.10: Number of events normalized by how many events were generated. The numbers in the table represent which percentage of the events where n (columns) pions were generated were reconstructed as events with m (rows) pions.

Rec \ Gen	0	1	2	3
0	-	85.7%	14.1%	0.2%
1	1.1%	86.5%	12.2%	0.1%
2	0.1%	4.5%	94.0%	1.4%
3	~ 0 %	4.0%	31.1%	64.9%

Table 3.11: Number of events normalized by how many events were reconstructed. The numbers in the table represent which percentage of events where n (rows) pions were reconstructed came from events where m (columns) were generated.

3.8.2 Acceptance correction factors

The acceptance was applied using five dimensional bins. The idea behind that is to reduce dependencies on the Montecarlo model.

The idea of correcting the data is based on two acceptance factors. One to account for events that were not correctly reconstructed (Acc_1). The other is to correct the incorrectly reconstructed event (Acc_2). For example, if two pions are produced in a collision, and one is missing, there will be a lost two pions event, but also there will be an extra one pion event that did not occur. The acceptance factors had the following form:

$$Acc_1^i = \frac{N^i_{accept=thrown}}{N^i_{thrown}} \qquad Acc_2^i = \frac{N^i_{accept=trown}}{N^i_{accept}} \tag{3.12}$$

where $Acc^i_{1,2}$ are the acceptance factors for events of i pions; N^i_{accept} is the number of events in the simulation where i pions were reconstructed, and N^i_{thrown} is the number of events where the Montecarlo simulation generated i pions, and $N^i_{accept=thrown}$ ($N^i_{a=t}$ from now on) is the number of events where the number of generated and reconstructed events are equal. These factors corrected the data as

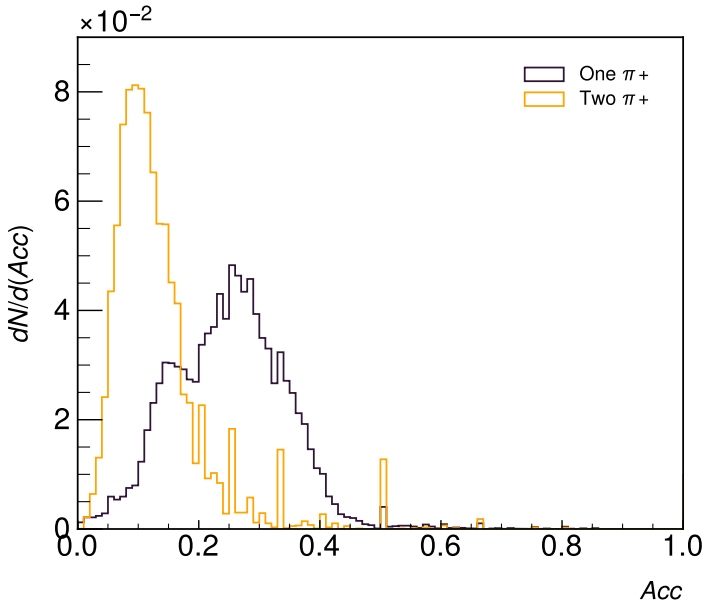

Figure 3.16: Acc normalized distribution. In black, one pion events; and in orange, two pions events. It can see be seen that for events of two pions, the factors are, in general, smaller. This is because detect two pions is less probably than detecting one

$$\text{Corr. data events}_i(5dim) = \text{data events}_i(5dim) \times \frac{Acc_2^i(5dim)}{Acc_1^i(5dim)} \tag{3.13}$$

where i represent the number of pions and the $5dim$ represent the variables (Q^2, ν, Zh_{Sum}, P_t^2, ϕ_{PQ}).

The final acceptance factor that was calculated is the ratio between the other both:

$$Acc^i = \frac{Acc_2^i}{Acc_1^i} = \frac{N_{thrown}^i}{N_{accept}^i} \tag{3.14}$$

The effect of this factor is logically the same but does not explicitly depend on $N_{a=t}^i$. However, it was applied the condition of having at least one well reconstructed event in the bin, that is $N_{a=t}^i(5dim) \geq 1$. The effect of this condition is shown in the systematic uncertainty Section 3.11. The acceptance factors distribution can be seen in Fig. 3.16.

The error of the factors was calculated assuming there is no correlation between the number of reconstructed events and the number of generated events. Therefore the error has the following form:

$$\delta Acc^i = Acc^i \sqrt{\frac{\delta N_{thrown}^i}{N_{thrown}^i} + \frac{\delta N_{accept}^i}{N_{accept}^i}} \tag{3.15}$$

Since the Montecarlo simulation generates N^i_{thrown}, it does not have an associated error. Considering that each trial has some probability of being reconstructed, δN^i_{thrown} was calculated assuming a binomial distribution. Thus the error of the acceptance factor is:

$$\delta Acc^i = \pm \left| \sqrt{\frac{Acc^i(1 - Acc^i)}{N^i_{thrown}}} \right| \tag{3.16}$$

3.8.3 Simulation vs data

If $N^i_{a=t} = 0$, the acceptance factors were not calculated, and those could imply loss some bins of data. Therefore; it is important that the simulations cover all the phase space of the data.

In Fig. 3.17, it is seen that simulations distributions are more similar to data for the liquid target than for solid targets, although they are not equal in either case. However, the simulation seems to cover all the phase space in the one dimensional plots.

Nevertheless, this is not true in five dimensions for two pion events because there are not as many events as for one pion events (Tab. 3.9). Fig. 3.18a shows the number of bins where there is data, and the bins where the is data and simulation ($N^i_{a=t} \geq 1$). It seen that there were events in the tale of P_t^2 distribution that were lost because there were not simulated events. The number of events in those bins is shown in Fig. 3.18b.

Even if the percentage of lost bins is notable (see Fig. 3.19a), they are in a low statistics region, so the percentage of events is not that big (see Fig. 3.19b) for $Zh_{Sum} < 0.8$. However, the lost events have high P_t^2, and there are most lost events for solid targets than for the liquid target, so this had a non-negligible impact on the transverse momentum broadening.

To avoid lossing those events, the acceptance factor in the bins where there is data, but no simulation were interpolated as a linear interpolation of all the non-zero factors adjacent to the five dimensional bin. The difference in the results with and without applying this procedure is shown in Fig. 3.20. This difference was considered a source of systematic error. More details about that will be given in Section 3.11.

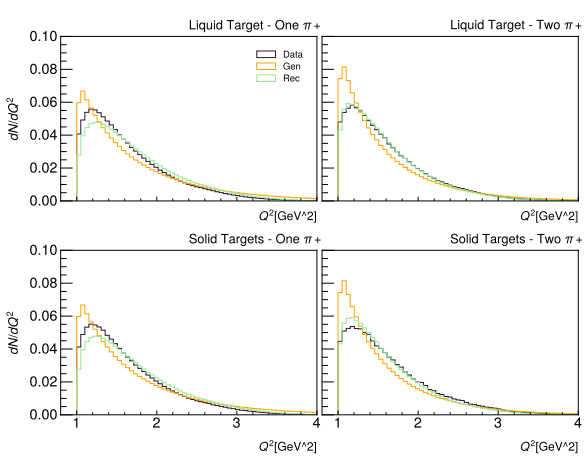

(a) Q^2 distribution

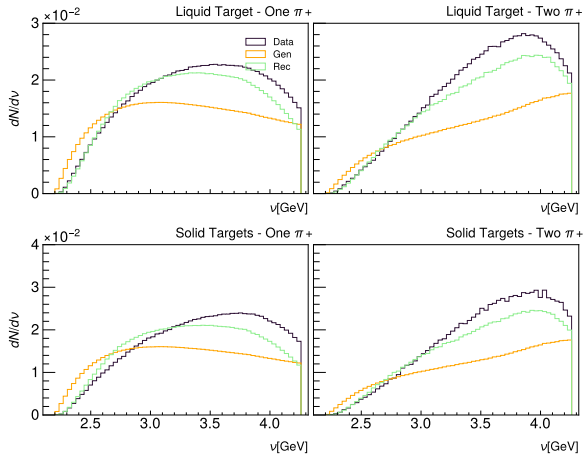

(b) ν distribution

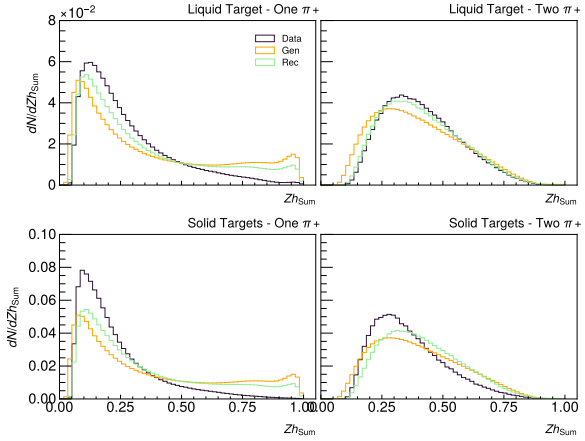

(c) Zh_{Sum} distribution

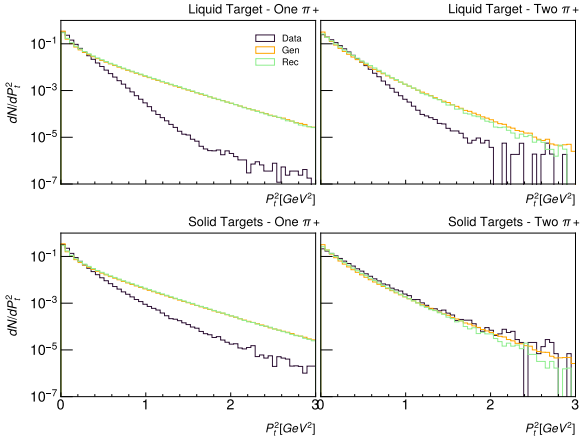

(d) P_t^2 distribution (Log scale)

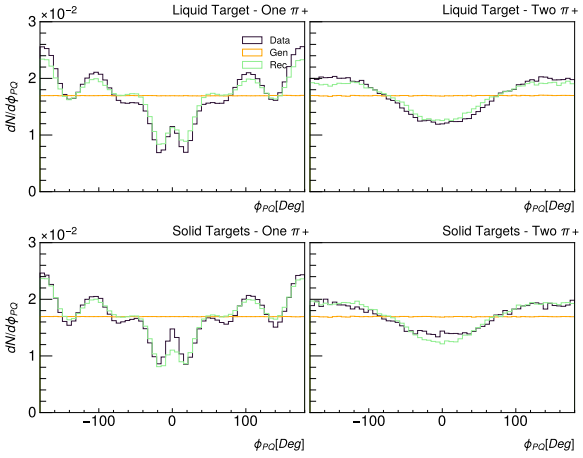

(e) ϕ_{PQ} distribution

Figure 3.17: Normalized distributions for some important variables. In black, events in the data, in orange, generated events in the simulation, and in light green, reconstructed events in the simulation.

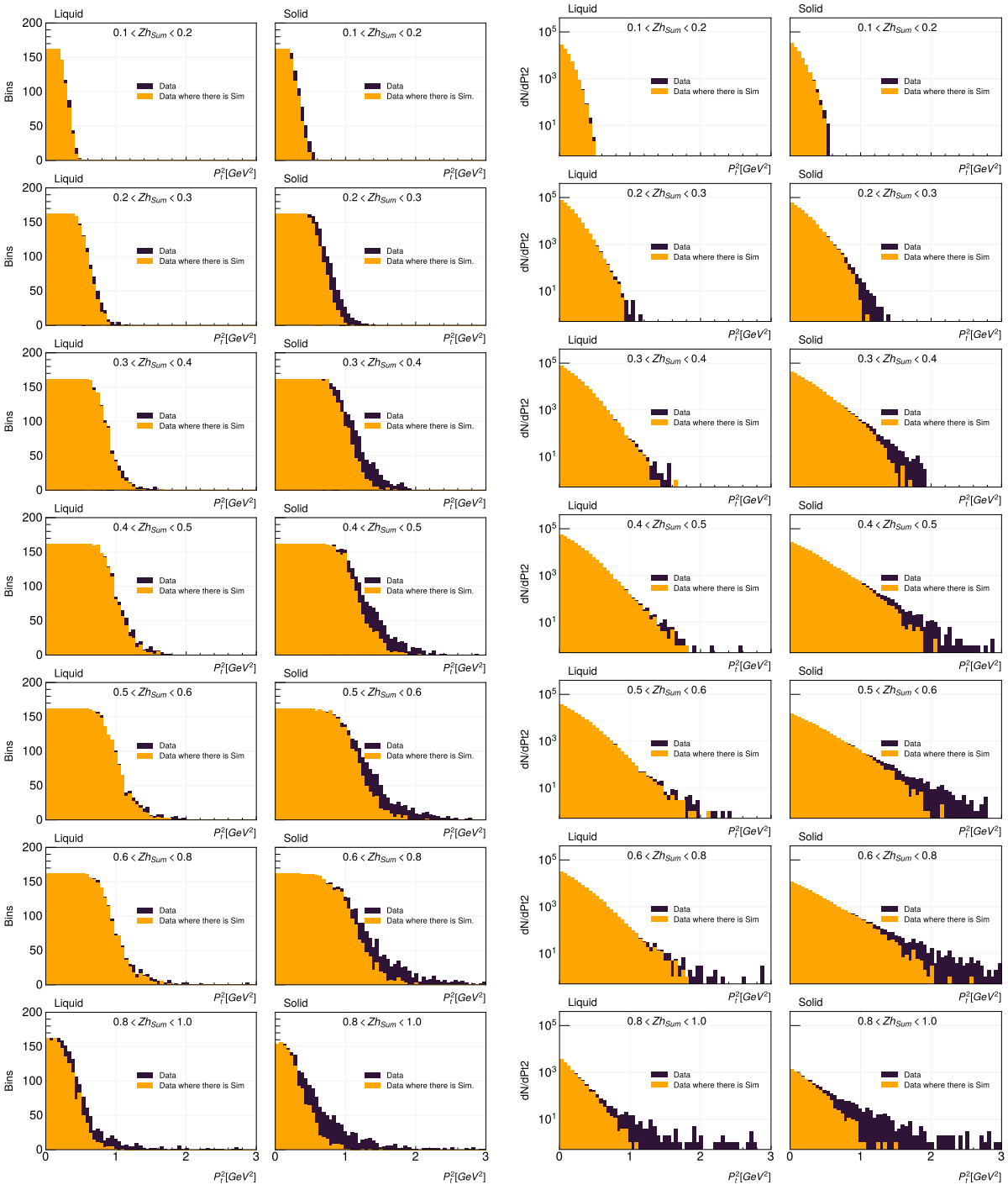

(a) Bins distributions

(b) Events distribution

Figure 3.18: In (a), the number of three dimensional bins (Q^2, ν, ϕ_{PQ}) as a function of P_t^2 and Zh_{sum}. In (b), P_t^2 distribution for different bins of Zh_{Sum}. Both cases are for two pions events. In dark blue, all the data, and in orange, data in bins in which there are well reconstructed events in the simulation.

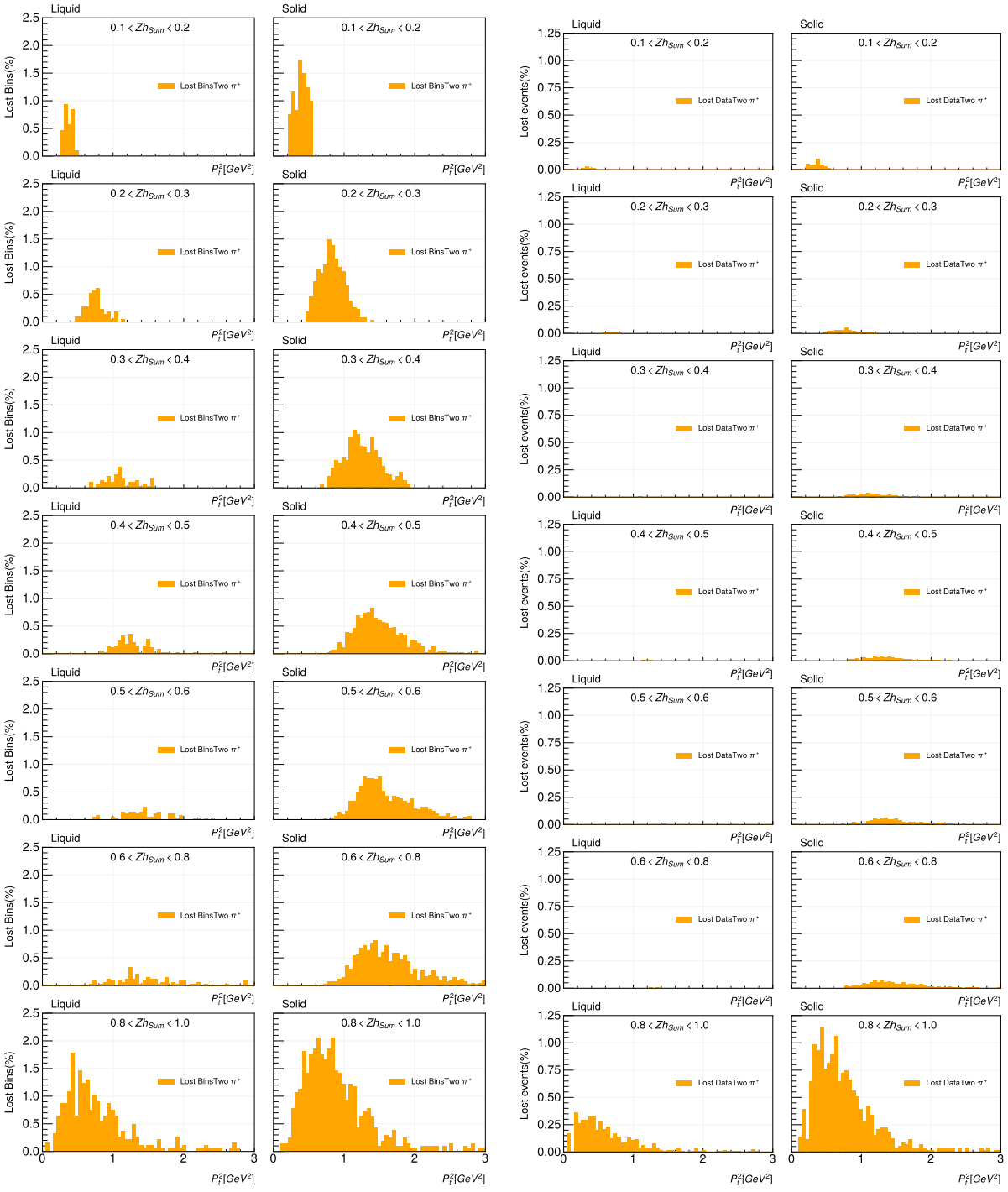

(a) Bins distributions (b) Events distribution

Figure 3.19: In (a), percentage of bins in which there is data but there are not well reconstructed events in the simulation. In (b) percentage of events located in bins in which there are data but not well reconstructed events in the simulation. Both cases are shown as a function of P_t^2 and Zh_{Sum}.

	Liquid Target	Solids Targets
Zh_{Sum}	Lost events(%)	Lost events(%)
0.1 - 0.2	0.062	0.319
0.2 - 0.3	0.029	0.282
0.3 - 0.4	0.022	0.358
0.4 - 0.5	0.036	0.506
0.5 - 0.6	0.044	0.773
0.6 - 0.8	0.063	1.116
0.8 - 1.0	4.496	15.202
Total	0.083	0.591

Table 3.12: Percentage of the two pion events in bins where there are not reconstructed events in the simulation.

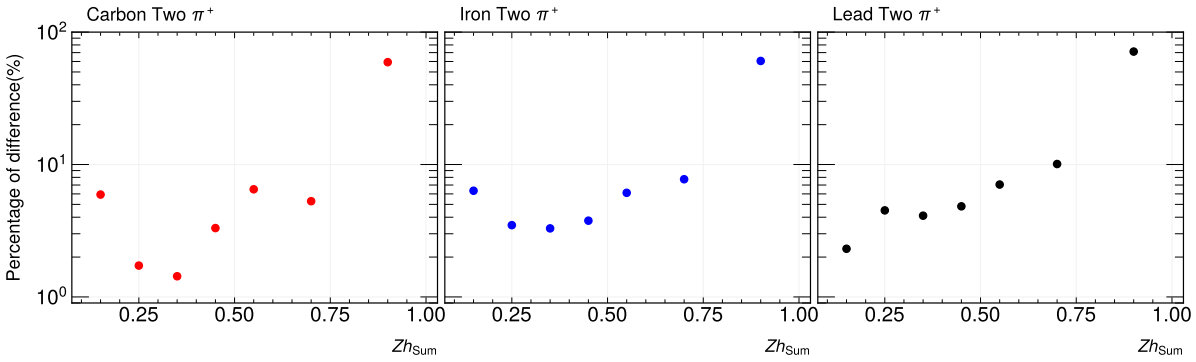

Figure 3.20: Percentage of difference between ΔP_t^2 calculated with and without the extrapolated acceptance factors. The plot is in logarithmic scale.

3.8.4 Acceptance Correction effects

The effect of the acceptance correction in the transverse momentum broadening can be seen in Fig. 3.21. The plot shows that in the first and last bin of Zh_{Sum}, the result changes by a factor of 2. This deviation is probably related to the low statistics, and it had a big impact on the calculation of the systematic errors related to the acceptance correction (see Sec 3.11).

3.9 Radiative correction

Radiative corrections (RC) aim to remove the contributions of the radiation of photons by the incoming or outgoing electron and the higher order electrodynamics contributions to the electron-photon vertex and the photon propagator [21] (see Fig 3.22). This photon emission implies a modification in the kinematic variables.

To correct this effect, a software called HAPRAD was used, which calculations are

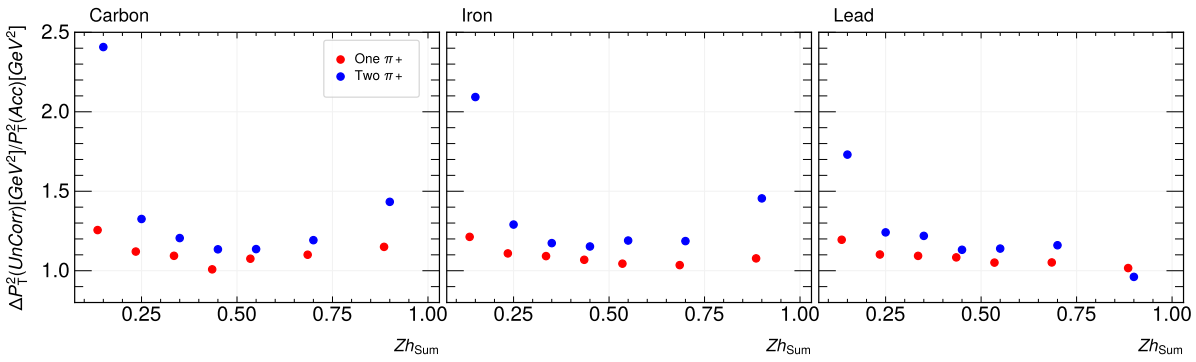

Figure 3.21: Ratio between the ΔP_t^2 calculated with the uncorrected data and with acceptance corrected data. Red points represent events with one pion, and blue points represent events with two pions

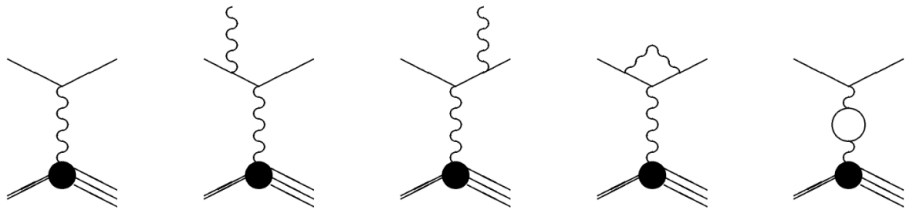

Figure 3.22: In (a) a one photon exchange process, and in the other letters the diagrams with the other radiative contributions

based in [22] and [23]. The software calculates radiative correction factors to correct the Born cross section as:

$$Rc = \frac{\sigma_{rad}}{\sigma_{Born}} \tag{3.17}$$

where σ_{rad} includes the lowest QED effects and the vacuum polarization.

These factors were calculated based on extracting structure functions from the data (after the acceptance correction). The method consists of fitting a function to the ϕ_{PQ} distribution for each four-dimensional bin of Q^2, X_b, Z_h, and P_t. The function had the following form:

$$F(\phi_{PQ}) = A + B\cos(\phi_{PQ}) + C\cos(2\phi_{PQ}) \tag{3.18}$$

Even though the acceptance correction was done with six bins in ϕ_{pq}, the fit was done using twelve bins instead. This change was done to increase the quality of the fit. As the variable is integrated in the final results, this does not generate changes in the broadening. The *Goodness of fit* or χ^2/ndf distribution is shown in Fig. 3.23.

It is important to notice that even if HAPRAD was developed for SIDIS analysis, it

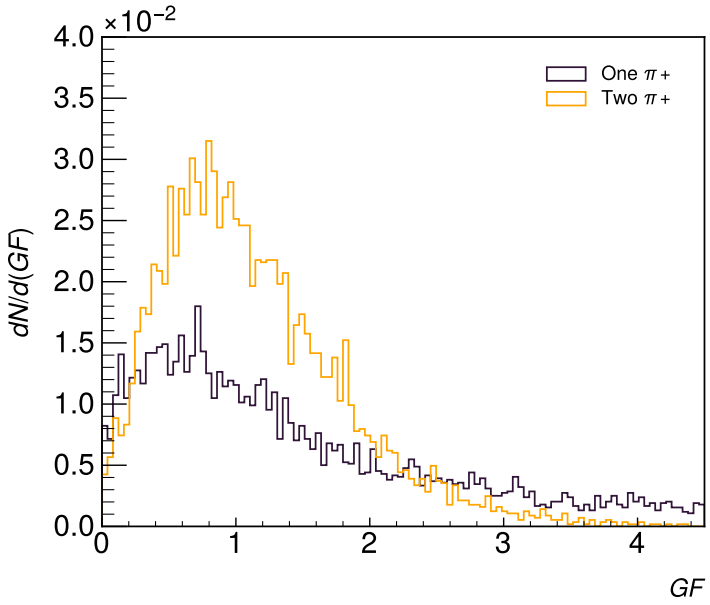

Figure 3.23: χ^2/ndf normalized distribution. In black, one pion events; and in orange, two pions events

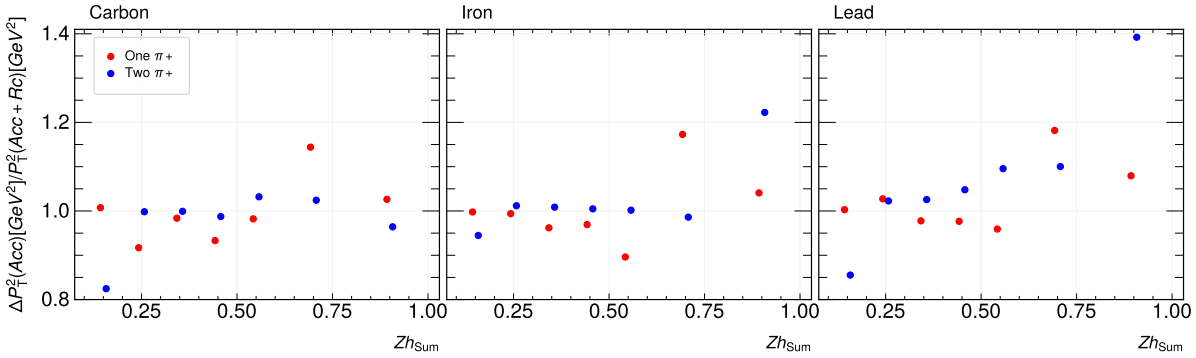

Figure 3.24: Ratio between the ΔP_t^2 with acceptance correction and with acceptance and radiative correction. Red points represent events with one pion, and blue points represent events with two pions

also works for two pion events because the correction is done in the leptonic branch of the DIS coalision. This means that the correction depends on the leptonic variables Q^2 and X_b and not in the hadronic final state.

The effect of the radiative correction in the observable can be seen in Fig. 3.24. For one pion events, the changes are around 5% but increases in some bins until 18%. For two pion events, the effects are around 5%, except for the first bin of carbon. Because the effects are much smaller than the acceptance correction, this will be used as a source of systematic error (see Sec. 3.11).

3.10 Background subtraction

The tail of the P_t^2 distribution could be contaminated with statistical fluctuation or bin migration. Hence, a background subtraction procedure was applied to guarantee the quality of the data. The procedure was based on the one shown in Esteban Molina's thesis [24].

The procedure consisted of two parts. The first consisted of removing the events with P_t^2 bigger than a cutoff value. Then the empty bins in P_t^2 distributions below the cutoff value were interpolated.

The cutoff values differed for each Zh_{Sum} bin and were selected to dismiss the events at high P_t^2, which does not follow an exponential behavior. The events were calculated following these steps.

- Fit an exponential function (see Eq 3.19) to the complete distribution. The cut off value of this fit is the value of P_t^2 where the function is equal to one.

$$f_{fit}(P_t^2) = CExp(-P_t^2/\alpha) \tag{3.19}$$

- Then fit function 3.19 again, but this time starting from the second bin, and find the cutoff value for the fit again.

- Repeat the process, increasing the initial bin from 1 to 15. Some of the fits can be seen in Fig 3.25. Notice that if the maximum number for the starting bin is selected too close to the end of the distribution, the fit can adjust to the noise.

- Finally, calculate the final cutoff value for the Zh_{Sum} bin taking a weighted mean of the previously calculated values. The weight is calculated depending on the quality of the fits and depends on χ^2_{ndf} and ndf and has the following form.

$$w_i = 0.95G(\chi^2_{ndf_i}) + 0.05P(ndf_i) \tag{3.20}$$

  where i represents the bin from which the fit begins; 0.95 a 0.05 are just assigned weights which measure how important is the contribution of each variable; $G(\chi^2_{ndf})$ is a Gaussian function with mean 1 and standard deviation 0.2, which give a big weight to values closer to 1 and almost eliminate the contributions of fits with χ^2_{ndf}

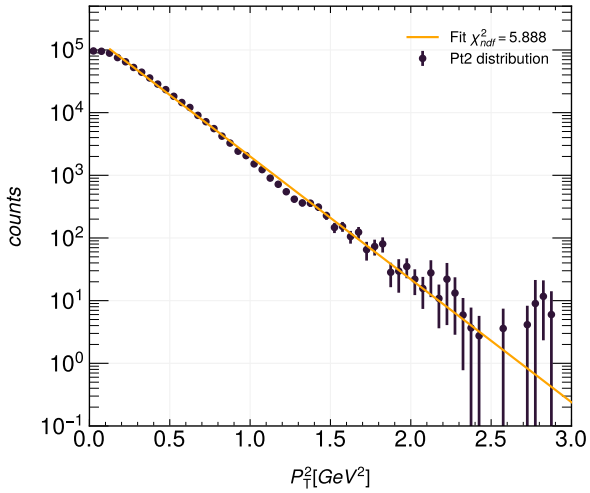

(a) One pion events; starting from the 3 bin

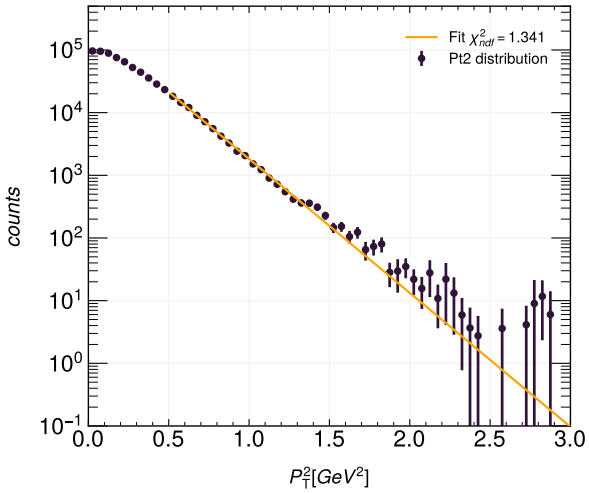

(b) One pion events; starting from the 12 bin

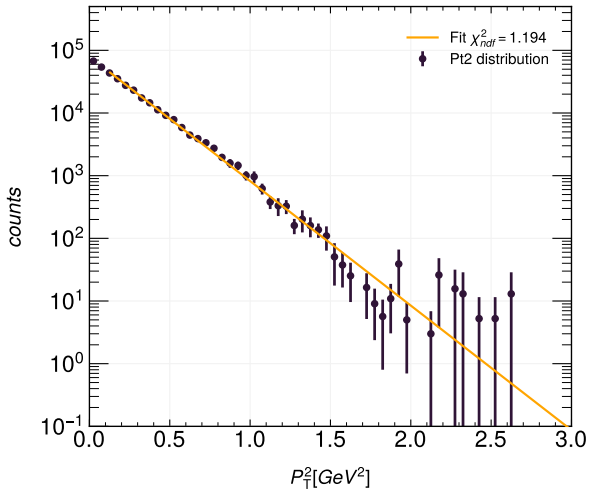

(c) Two pion events; starting from the 3 bin

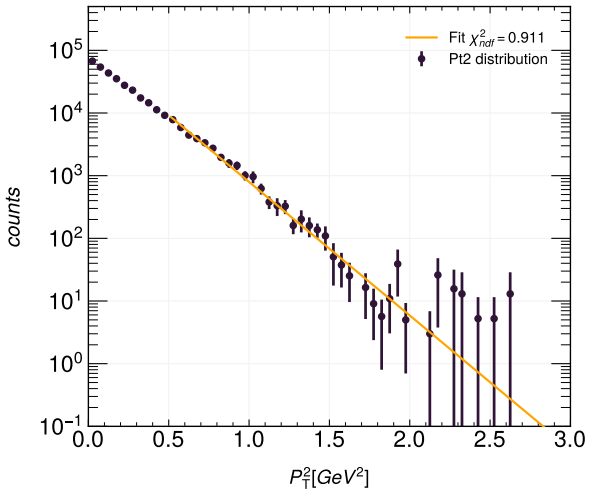

(d) Two pion events; starting from the 13 bin

Figure 3.25: Fits to the P_t^2 for carbon target and $0.5 < Z_h < 0.6$

out of the range $1 \pm 2\sigma$; and $P(ndf_i)$ is just ndf_i divided by the sum of the ndf_i values for all the fits, this gives a big weight to fit when ndf_i is bigger.

The idea behind the multiple fits method is to decrease the bias in the calculation of the cutoff value.

After eliminating the events, all the empty bins in the distribution were replaced with a linear interpolation between the previous and posterior non-empty bins. The distribution after the procedure can be seen in Fig 3.26.

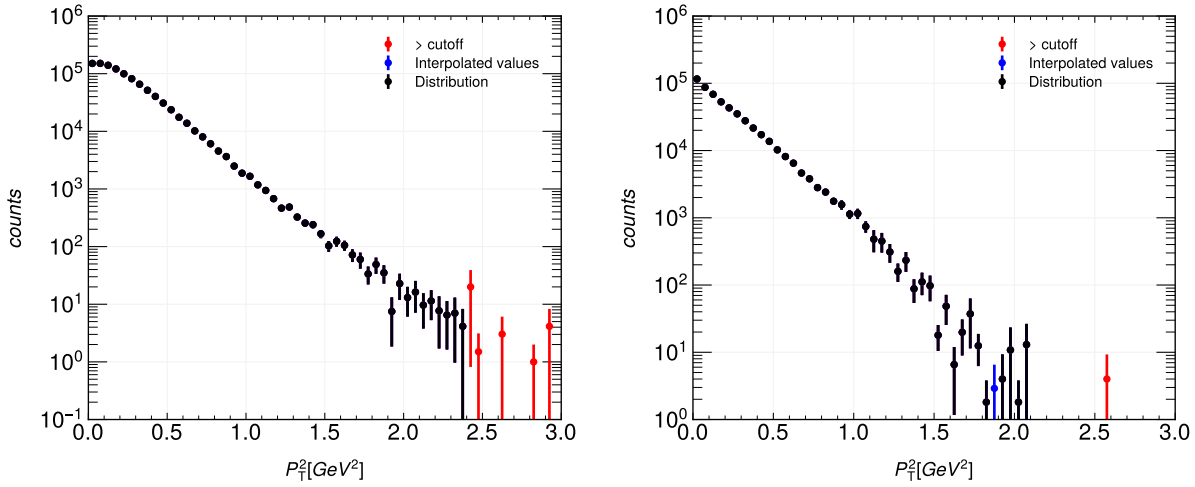

(a) One pion Events (b) Two pion events

Figure 3.26: P_t^2 distribution after the background subtraction for C target with Zh_{Sum} between 0.4 and 0.5. In black, the original point in the distribution; in red, events with P_t^2 bigger than the cutoff value; and in blue, the interpolated points.

3.11 Systematic uncertainties

The sources of systematic errors studied in this analysis are based on the ones used in the charged pion analysis [16].

The value for the systematic error was obtained under the assumption that the nominal value is in the center of a uniform distribution with a length of 2Δ, where Δ is the biggest variation with respect to the nominal value. This assumption was made because no predilection is expected for the selected nominal values. It was estimated that by taking the systematic error as the standard deviation of the uniform distribution, the real value is within the interval with a 68% confidence interval. Therefore, the systematic error reads:

$$f_{uniform} = \frac{1}{2\Delta} = \frac{1}{2\sigma\sqrt{3}} \rightarrow \sigma_{sou} = \pm\frac{\Delta}{\sqrt{3}} \tag{3.21}$$

The total systematic error (σ_{sys}) was calculated as:

$$\sigma_{sys}^2 = \sum_{Sources} \sigma_{sou}^2 \tag{3.22}$$

where the sum goes through all the systematic error sources.

The sources of systematic uncertainty are shown in the next subsections. The results are shown as the percentage of deviation from nominal value and were calculated as

follows:

$$Deviation(\%) = \frac{\Delta Pt^2_{nominal} - \Delta Pt^2_{variation}}{\Delta Pt^2_{nominal}} \tag{3.23}$$

3.11.1 Systematic error sources

1. **Positive Pion identification cuts**

   As seen in Chapter 3.2.2, the TOF were used to identify positive pions up to a limit in the momentum. The nominal value for this limit was 2.7 GeV, and it varied to 2.5 GeV and 2.9 GeV.

   The deviations are, in general, smaller than 1.5% for one and two pions events, except for the $0.8 < Zh_{Sum} < 1$, in this range are around 10%, and reach 20% for lead in two pions events. see Fig 3.31.

2. **Vertex identification**

   Two other methods to identify the vertex of interaction were used to calculate the systematic uncertainty. One was developed by Hayk Hakobyan (see [20]), and the other was developed by Raphael Dupré (see [19]).

   Raphael's method shifted the Z coordinate depending on the Sector and then applied a cut in the shifted variable. The cuts depend on the solid target. The shifts and cuts can be seen in Table 3.13 and Table 3.14, respectively.

Sector	0	1	2	3	4	5
Shift [cm]	+0.1	-0.4	-0.6	-0.1	+0.4	+0.6

Table 3.13: Z shift in Raphael's method

Target	Liquid	Liquid	Solid	Solid
	Z Lower cut [cm]	Z Upper cut [cm]	Z Lower cut [cm]	Z Upper cut [cm]
D-C	-32.1	-28.1	-26.2	-23.2
D-Fe	-32.2	-28.2	-26.4	-23.4
D-Pb	-32.1	-28.1	-26.2	-23.2

Table 3.14: Z cuts in Raphael's method

Hayk's method did not correct the coordinates, Instead, it consisted of applying sector dependent cuts in the Z variable. The exact cuts can be seen in Table 3.15. Furthermore, the nominal cuts and the two variation can be seen in Fig. 3.27.

Target	Liquid	Liquid	Solid	Solid
Sector	Z Lower cut [cm]	Z Upper cut [cm]	Z Lower cut [cm]	Z Upper cut [cm]
1	-32.50	-28.00	-26.50	-20.00
2	-32.50	-27.50	-26.00	-20.00
3	-32.00	-27.75	-25.65	-20.00
4	-32.00	-27.75	-25.85	-20.00
5	-32.50	-28.35	-26.65	-20.00
6	-32.50	-28.75	-27.15	-20.00

Table 3.15: Z cuts in Hayk's method

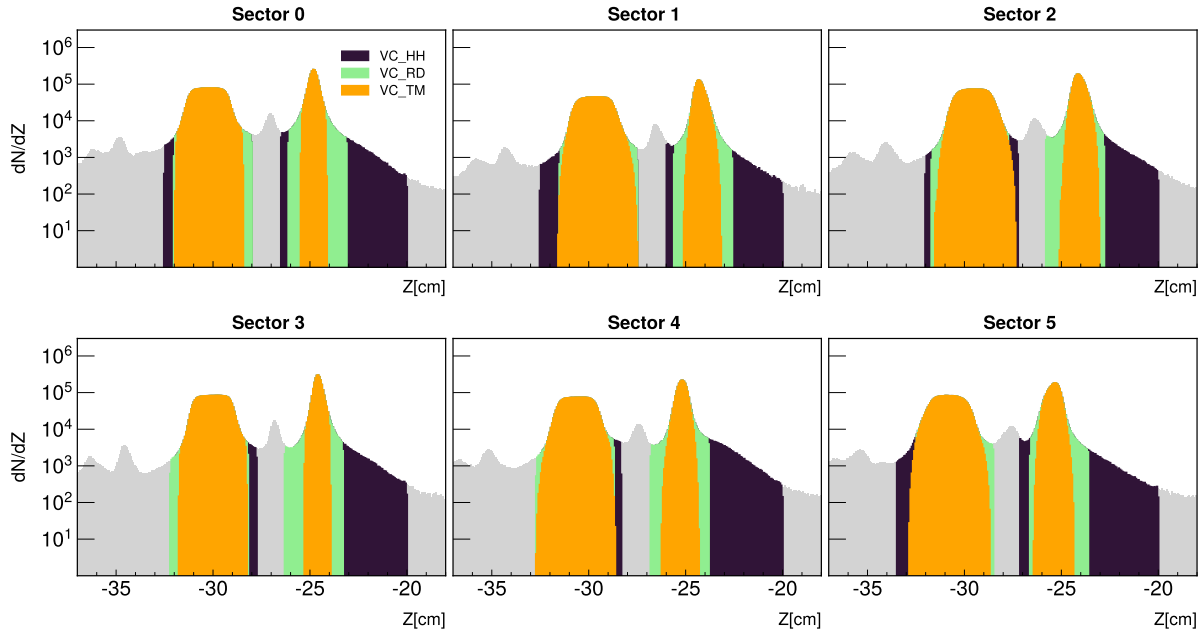

Figure 3.27: Z distribution for each sector; in gray all the rejected events; in orange the events that obey the nominal cuts; in blue the events that passed Raphael's cuts, and in dark blue the events allowed by the Hayk's cuts

Deviations have similar behavior in all the range of Zh_{Sum} and for one and two pions events. They are, generally, within 0.15% and 3.3%, and for the last Zh_{Sum} bin is 9%. see Fig 3.32.

3. ΔZ **Cut**

The $|\Delta Z|$ nominal cut is $|\Delta Z| < 3.0$ cm and it was varied to $|\Delta Z| < 2.5$ cm and $|\Delta Z| < 3.5$ cm.

Deviation grows with Zh_{Sum} for one pion events. Two pion events deviation do not increase with Zh_{Sum} but have similar values than for one pion events, except for the last bin of iron results when it grows to 13%. In general, deviations go from $\sim 0\%$ to 4%. see Fig. 3.33.

4. **Background subtraction procedure**

   The background subtraction consisted of two steps, finding a cutoff value and interpolating the empty bins below that value. The two variations applied were found to the cutoff value but with out interpolation and no procedure was applied.

   Deviations are in general smaller than 0.5% for one and two pion events, although, in some bins, they grow to 2.7% for one pion events and 8% the last bin of carbon in two pion events. see Fig. 3.34.

5. **Number of bins**

   The acceptance correction was done with a nominal value of 60 bins in P_t^2. This value was varied to 50 and 70 bins.

   For one pion events, deviations have a similar value for all the bins in Zh_{Sum} and are around 0.8%. In the cases of two pion events, the deviations are around 2% in the region $0.2 < Zh_{Sum} < 0.8$. Outside this region, the errors are bigger and can grow until 12% for most of the variations, and reach 40% in lead results.

6. $N^i_{a=t}$ **Cut**

   In the nominal acceptance correction procedure, the cut $N^i_{a=t} >= 1$ was applied (see Sec. 3.8). The variations selected were $N^i_{a=t} >= 0$ and $N^i_{a=t} >= 2$.

   For one pion events, the deviations are around 0.5% for all the Zh_{Sum} and for both variations. In the case of two pions events, the deviations are different for the two variations. For the cut $N^i_{a=t} >= 0$, the deviations, in general, are around 2%, but reach 10% in the last bin of Zh_{Sum} for lead. In the case of the cut $N^i_{a=t} >= 2$, the deviations grow with Zh_{Sum} from 2% to 15%.

   The impact of the second variation could be understood by studying the number of bins that are empty after applying the cut but were not empty before applying it (see Fig. 3.28). It can be observed that for one pion events, the number of empty bins is almost negligible. In the case of events with two pions, the number of bins is much bigger. Also, the number of empty bins differs for the liquid and the solid target. This difference explains the big deviations in the broadening because it depends on the differences between the two types of targets.

7. **Acc minimum value**

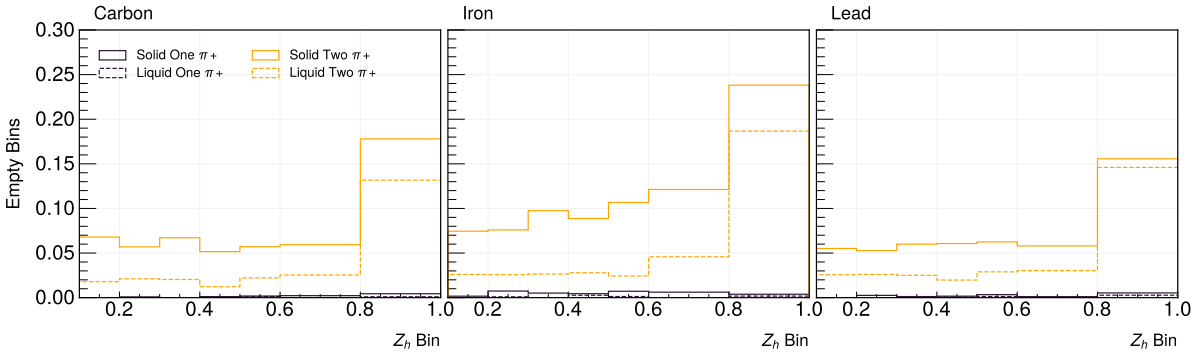

Figure 3.28: Fraction of empty five dimensional bins after the cut $N^{i}_{a=t} >= 2$. The fraction was calculated for each Zh_{Sum} separately. That is, each Zh_{Sum} bin shows the number of five dimensional bins that were empty after the cut within that range of Zh_{Sum} divided by the total number of not empty bins before the cut in the same region.

There is no limit for Acc in the nominal acceptance correction. Two cuts were tested anyway. The variations selected were $Acc > 0.017$ and $Acc > 0.020$. This cut was applied before the interpolation procedure of the acceptance factor (see Subsec. 3.8.3).

The deviation is almost negligible in almost all the cases. However, for two pion event in carbon and iron its around 3%.

8. **Closure test**

Closure test is a method to test the quality of the acceptance correction process. The idea is to use half of the events in the simulation to calculate the acceptance correction factors and apply them to the reconstructed events in the remaining half of the simulation. As the events which generate the reconstructed are known, it is possible to compare the corrected results to the generated ones. To compare, the variable w is used.

$$w = \frac{\text{corr rec sim}}{\text{generated sim}} \tag{3.24}$$

which is basically the number of reconstructed events in the second half of the simulation after the correction divided by the number of generated events in the same half of the simulation. The calculation was done in five dimensional bins using the same binning as the acceptance correction. The closer w is to 1, it is expected better behavior of the acceptance correction.

Taking into account the fact that w is not equal to one, the w value was used as a

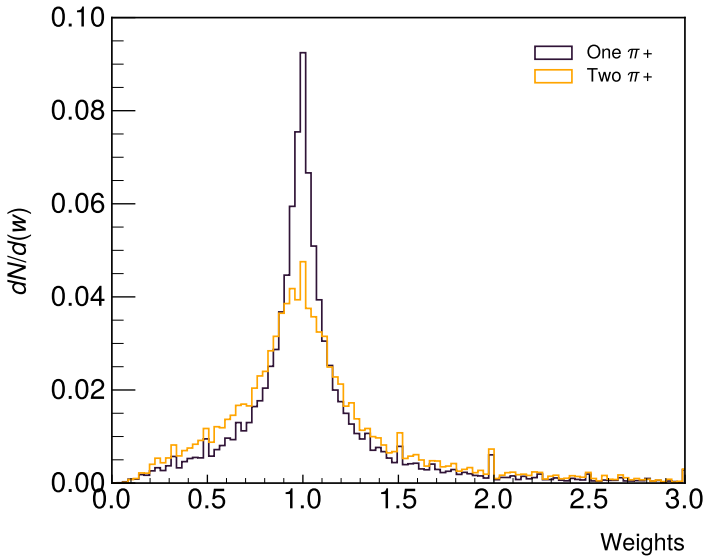

Figure 3.29: Distributions of the weights generated with the closure test. In black, weights for one pion event, and in orange, weights for two pion events.

weight to scale the acceptance correction factors. The correction was:

$$Acc^{i}_{CT} = Acc \times w \tag{3.25}$$

this factor was applied to the data as follows:

$$\text{Corr. data events}_i(5dim) = \text{data events}_i(5dim) \times \frac{1}{Acc^{i}_{CT}(5dim)} \tag{3.26}$$

The distribution of the w values can be seen in Fig. 3.29.

In this systematic uncertainty source, just one variation was considered.

The deviations for one pion events are smaller than 8%. For two pions events without considering the last bin of Zh_{Sum} the deviations are between the 0.3% and the 15%. In the last bin of lead the deviation is 25%.

9. **Acceptance factor interpolation**

As seen in subsection 3.8.3 the acceptance factors in the bins where there is not reconstructed events was interpolated. To apply or do not apply the interpolation was considered as a systematic uncertainty.

For one pion events, the deviations are $\sim$ 0% because the simulation covers all the phase space. For two pion events, the deviations are within 1% and 10% for

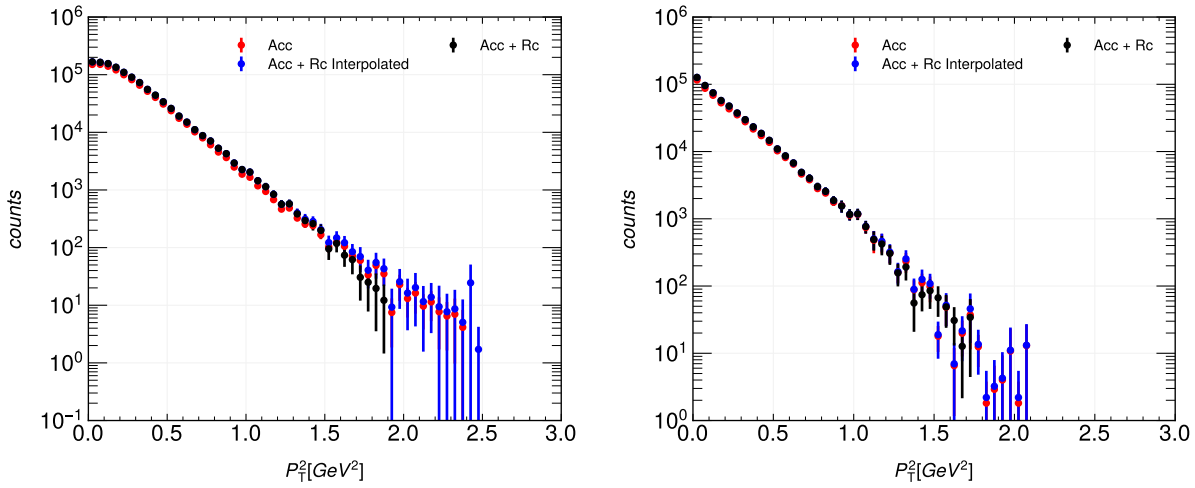

(a) One Pion Events (b) Two Pions events

Figure 3.30: P_t^2 distribution after applying the radiative correction factors for C target with Zh_{Sum} between 0.4 and 0.5. Red points are the distribution with just acceptance correction, black points are the distribution with the RC factors calculated by HAPRAD applied, and in blue points are the distribution after applying the RC factors after the interpolation procedure.

$Zh_{Sum} < 0.8$. For the last bins deviation are between 60% and 70%.

10. **Radiative correction**

    As was mentioned in Subsection 3.9, the radiative correction was considered a source of systematic error. Two variations were selected. The first was applying the RC factors calculated by HAPRAD. However, the software did not calculate the RC factors in all the five dimensional bins (see Fig. 3.30). The second variation was interpolate the RC factors that were not calculated and then applied them to the data and calculate the broadening.

    The deviations are, in general, bigger for one pion events than for two pions events. For one pion events, the deviations go from 1% to 15%, being bigger in the region with Zh_{Sum} within 0.5 to 0.8. The deviations for two pions events are similar for all the Zh_{Sum} bins and are around 3%. Nevertheless, for the first bin of carbon results, the deviation grows to 34%.

3.11.2 Systematic error summary

In the cases of systematic error sources that are unrelated to acceptance correction, the deviations are generally in a similar range for one and two pions events. However, the

sources related to the acceptance correction generate a bigger deviation in the case of two pions events. This effect is more noticeable in the cases when $0.1 < Zh_{Sum} < 0.2$ and $0.8 < Zh_{Sum} < 1.0$. This fact is expected because of the low statistics and the effect that has the acceptance correction in the broadening (see Fig. 3.21).

All the systematic errors are summarized in Tab. 3.16, 3.17, and 3.18, which includes the minimum and the maximum deviation of the broadening in the different Zh_{Sum} bins. Table s 3.19, 3.20, and 3.21 contain the same information but without considering the region $0.1 < Zh_{Sum} < 0.2$ and $0.8 < Zh_{Sum} < 1.0$ because there the deviation are much bigger, so they are not a good representation of the behavior of the systematic errors.

The *Total* row is the sum of the deviations squared divided by $\sqrt{3}$ (see Eq. 3.21).

	One pion		Two pion	
Systematic	min variation	max variation	min variation	max variation
Pion Identification	0.03%	6.48%	0.04%	6.05%
Vertex identification	0.2%	1.51%	0.21%	4.88%
ΔZ Cut	0.36%	5.43%	0.9%	3.65%
BG Subtraction	0.0%	0.79%	0.0%	8.51%
Number of bins	0.09%	1.32%	0.94%	12.05%
$N^i_{a=t}$	0.0%	0.37%	0.81%	7.31%
Limit Acc	0.0%	0.0%	0.0%	4.61%
Closure Test	0.44%	7.31%	0.45%	13.82%
Rad. Corrections	0.74%	12.59%	0.34%	21.28%
Acc Interpolation	0.0%	0.12%	1.49%	59.59%
Total	0.0 %	9.73 %	0.82 %	38.97%

Table 3.16: Summary of the systematic errors for carbon results.

	One pion		Two pion	
Systematic	min variation	max variation	min variation	max variation
Pion Identification	0.13%	1.75%	0.01%	4.27%
Vertex identification	0.01%	0.44%	0.01%	3.58%
ΔZ Cut	0.51%	4.38%	0.41%	4.34%
BG Subtraction	0.0%	0.66%	0.0%	5.79%
Number of bins	0.35%	1.38%	0.62%	8.92%
$N^i_{a=t}$	0.0%	0.77%	1.65%	7.01%
Limit Acc	0.0%	0.0%	0.0%	0.06%
Closure Test	0.67%	2.88%	2.88%	14.83%
Rad. Corrections	0.24%	14.74%	0.51%	21.51%
Acc Interpolation	0.0%	0.58%	3.29%	62.14%
Total	0.0 %	9.09 %	2.58 %	39.8%

Table 3.17: Summary of the systematic errors for iron results.

	One pion		Two pion	
Systematic	min variation	max variation	min variation	max variation
Pion Identification	0.01%	10.25%	0.03%	19.94%
Vertex identification	0.3%	2.62%	0.48%	2.45%
ΔZ Cut	0.93%	4.52%	1.27%	5.41%
BG Subtraction	0.0%	2.26%	0.0%	3.27%
Number of bins	0.25%	0.47%	0.17%	39.34%
$N^i_{a=t}$	0.0%	0.75%	1.33%	15.43%
Limit Acc	0.0%	0.0%	0.0%	0.0%
Closure Test	0.23%	6.29%	0.72%	25.61%
Rad. Corrections	0.28%	15.38%	2.05%	27.92%
Acc Interpolation	0.0%	0.52%	2.31%	71.18%
Total	0.0 %	11.7 %	1.91 %	53.94%

Table 3.18: Summary of the systematic errors for lead results.

	One pion		Two pion	
Systematic	min variation	max variation	min variation	max variation
Pion Identification	0.03%	0.5%	0.04%	1.2%
Vertex identification	0.2%	0.52%	0.39%	1.45%
ΔZ Cut	1.38%	4.34%	0.9%	3.59%
BG Subtraction	0.01%	0.79%	0.0%	1.18%
Number of bins	0.09%	1.32%	0.94%	2.13%
$N^i_{a=t}$	0.0%	0.37%	0.81%	7.31%
Limit Acc	0.0%	0.0%	0.0%	0.0%
Closure Test	0.44%	7.31%	0.45%	13.82%
Rad. Corrections	1.8%	12.59%	0.34%	3.67%
Acc Interpolation	0.0%	0.04%	1.49%	7.05%
Total	1.15 %	8.76 %	0.82 %	10.41%

Table 3.19: Summary of the systematic errors for carbon results within $0.2 < Zh_{Sum} < 0.8$.

	One pion		Two pion	
Systematic	min variation	max variation	min variation	max variation
Pion Identification	0.13%	1.75%	0.01%	1.52%
Vertex identification	0.01%	0.32%	0.07%	0.28%
ΔZ Cut	1.29%	4.2%	0.41%	2.08%
BG Subtraction	0.0%	0.14%	0.02%	0.53%
Number of bins	0.35%	1.38%	0.62%	2.47%
$N^i_{a=t}$	0.03%	0.77%	2.18%	6.44%
Limit Acc	0.0%	0.0%	0.0%	0.06%
Closure Test	0.71%	2.88%	2.88%	14.83%
Rad. Corrections	0.63%	14.74%	0.51%	2.29%
Acc Interpolation	0.01%	0.57%	3.29%	7.93%
Total	0.58 %	9.06 %	2.71 %	10.63%

Table 3.20: Summary of the systematic errors for iron results within $0.2 < Zh_{Sum} < 0.8$

	One pion		Two pion	
Systematic	min variation	max variation	min variation	max variation
Pion Identification	0.01%	2.63%	0.03%	0.45%
Vertex identification	0.3%	1.69%	0.48%	2.12%
ΔZ Cut	1.37%	4.52%	1.27%	5.08%
BG Subtraction	0.0%	0.61%	0.02%	3.27%
Number of bins	0.25%	0.47%	0.17%	3.51%
$N^i_{a=t}$	0.01%	0.75%	1.33%	10.24%
Limit Acc	0.0%	0.0%	0.0%	0.0%
Closure Test	0.73%	6.29%	0.72%	8.84%
Rad. Corrections	2.66%	15.38%	2.05%	9.11%
Acc Interpolation	0.02%	0.52%	4.13%	10.09%
Total	1.63 %	10.05 %	2.77 %	11.78%

Table 3.21: Summary of the systematic errors for lead results within $0.2 < Zh_{Sum} < 0.8$.

3.11.3 Plots

The plots of the deviation due to systematic uncertainties have the following form:

- In the first row (in red) are the results for one pion events, and in the second row (in blue) are the results for two pion events.
- The filled areas represent the statistical errors of the measurement.

$$\text{Statistical deviation} = \frac{\text{Statistical error}}{\text{Nominal value}} \times 100 \tag{3.27}$$

- The triangles represent the systematic deviation (Eq. 3.23).

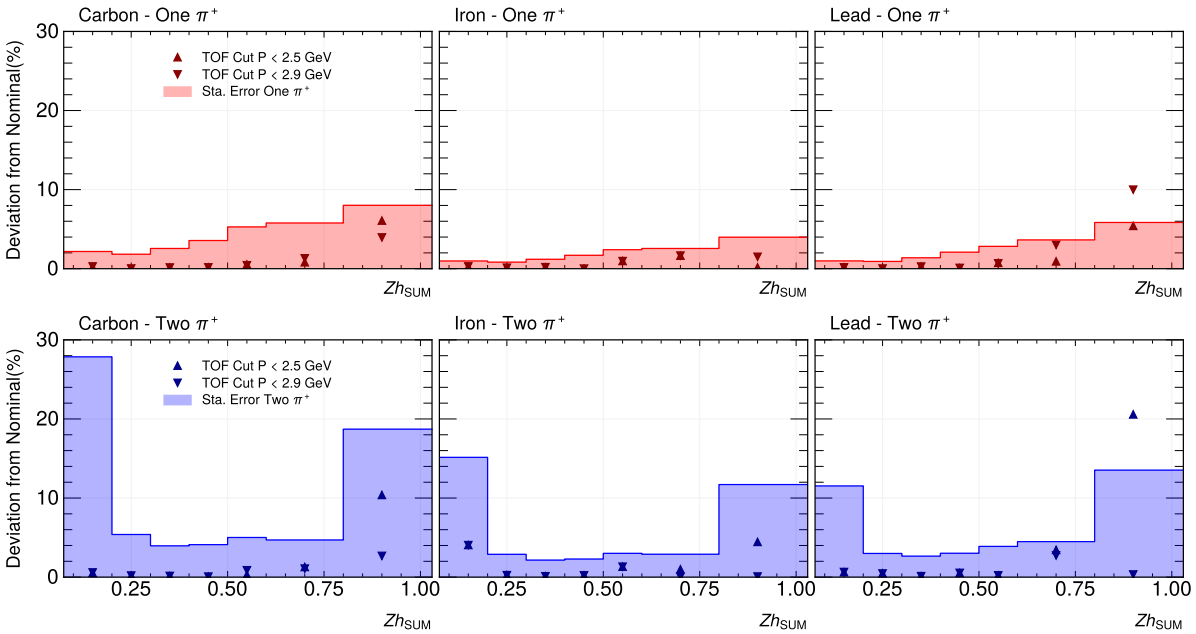

Figure 3.31: Deviation from the nominal ΔP_t^2 value due to the variation in the positive pion identification.

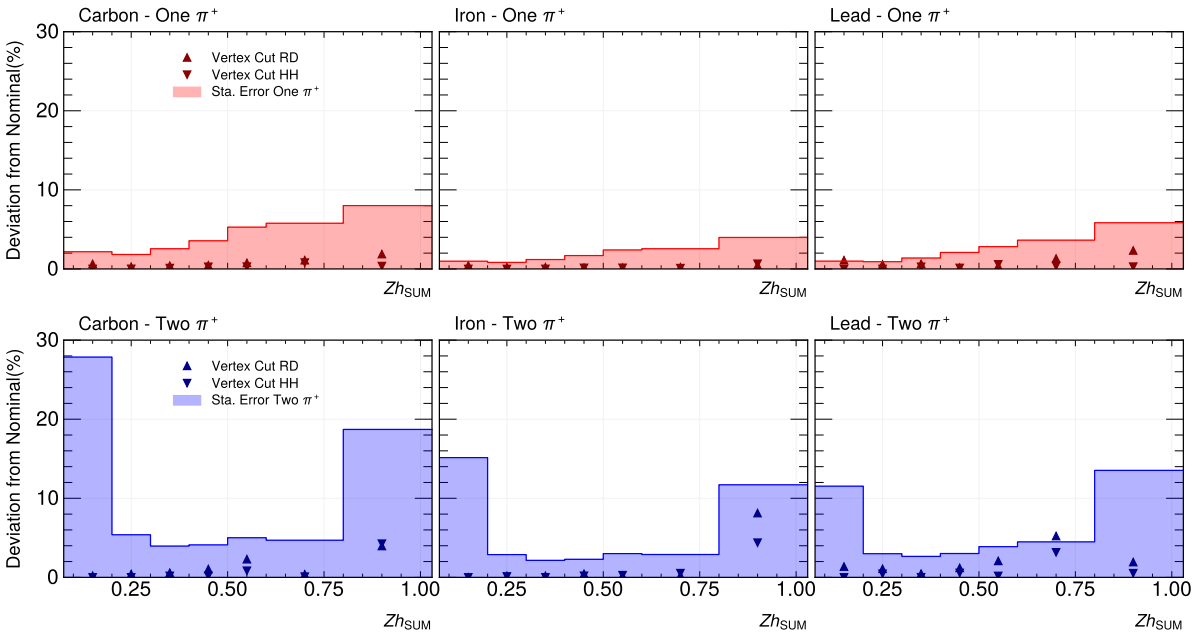

Figure 3.32: Deviation from the nominal ΔP_t^2 value due to the variation in the method used to select the vertex of interaction.

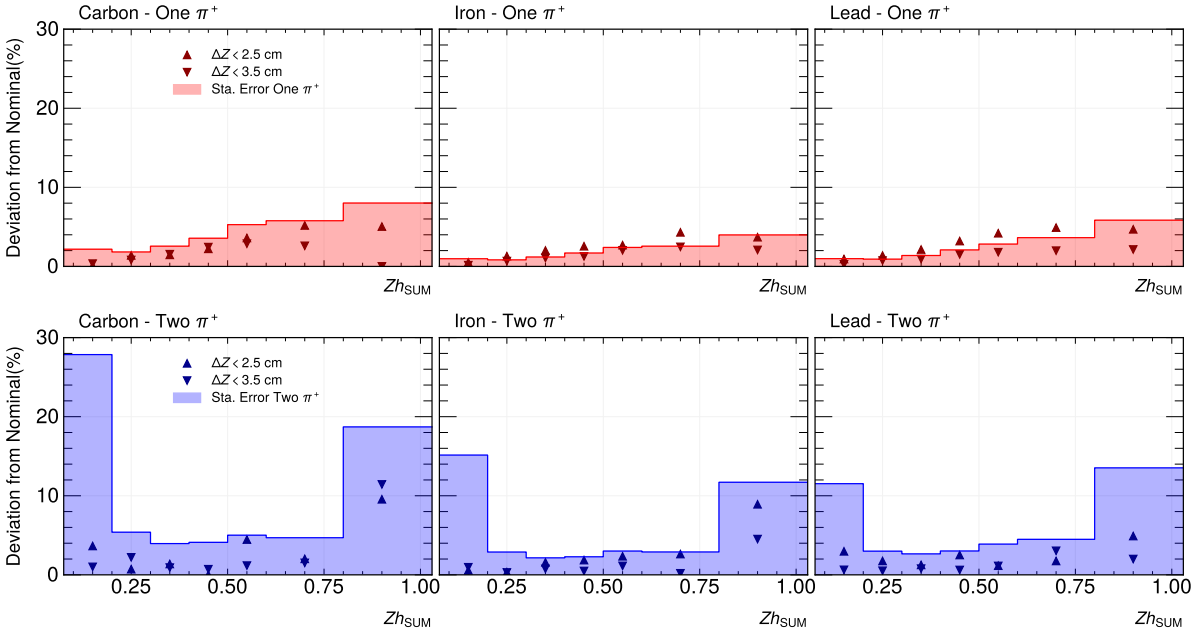

Figure 3.33: Deviation from the nominal ΔP_t^2 value due to the variation in the ΔZ cut.

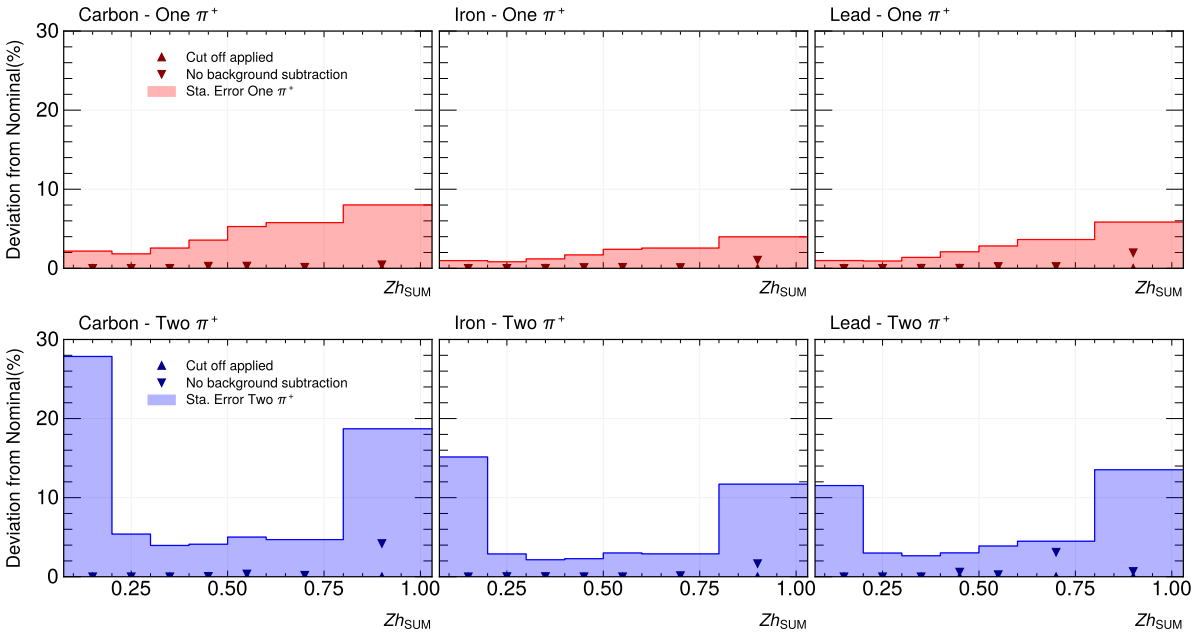

Figure 3.34: Deviation from the nominal ΔP_t^2 value due to the variation in the background subtraction procedure.

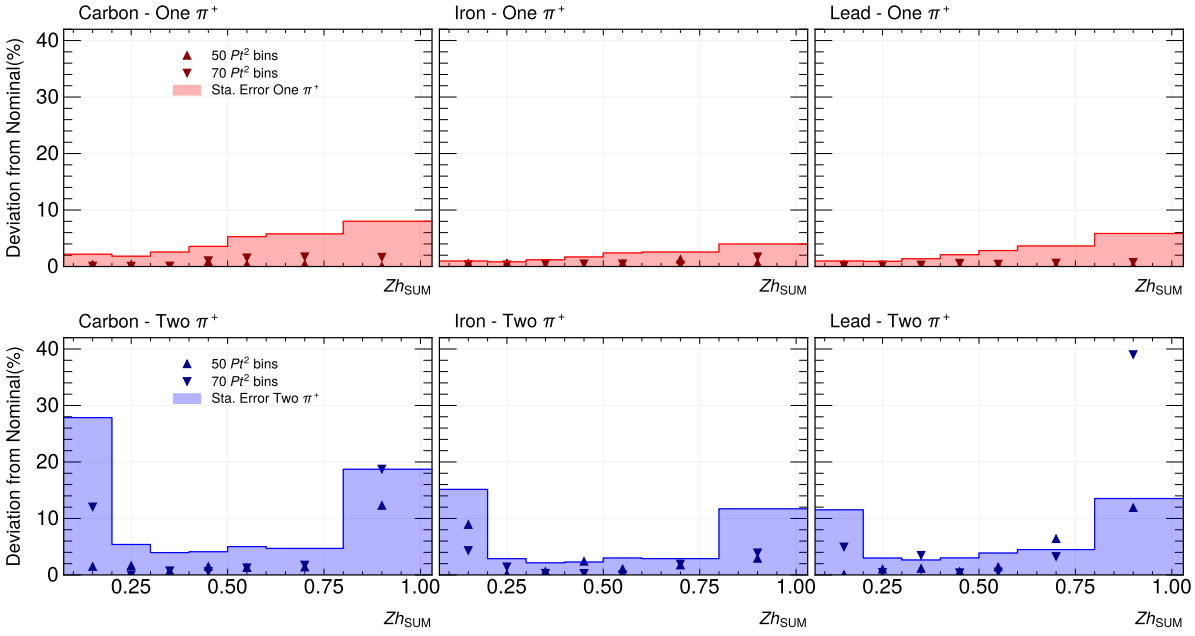

Figure 3.35: Deviation from the nominal ΔP_t^2 value due tothe variation in numbers of P_t^2 bins in the acceptance correction.

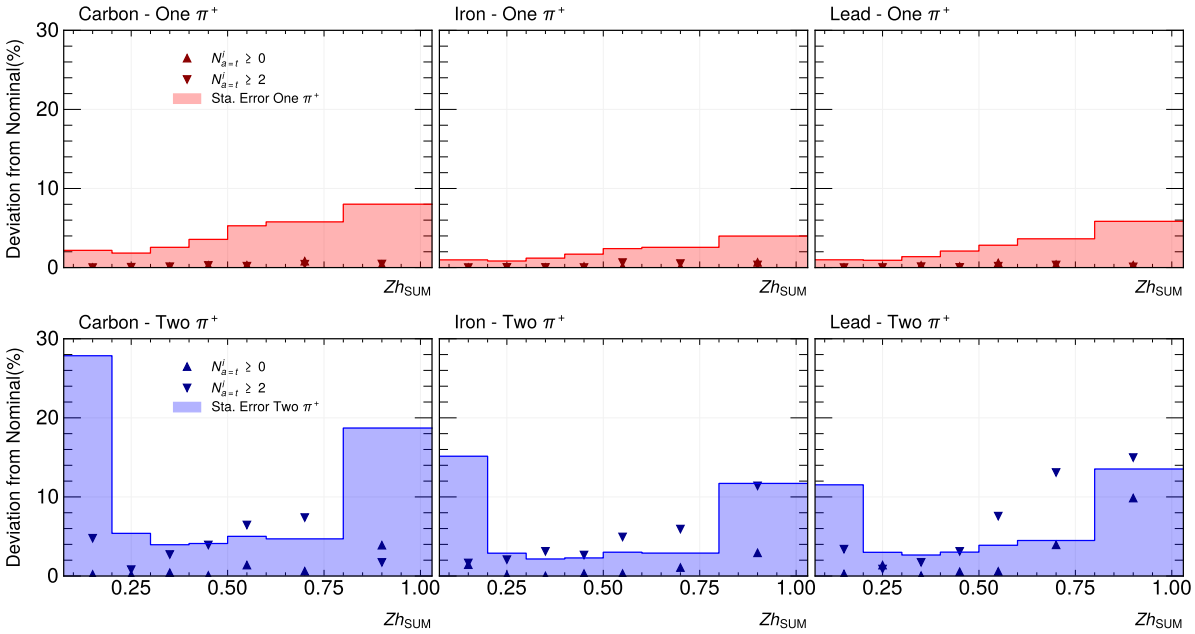

Figure 3.36: Deviation from the nominal ΔP_t^2 value due to the variation in $N^i_{a=t}$ cut.

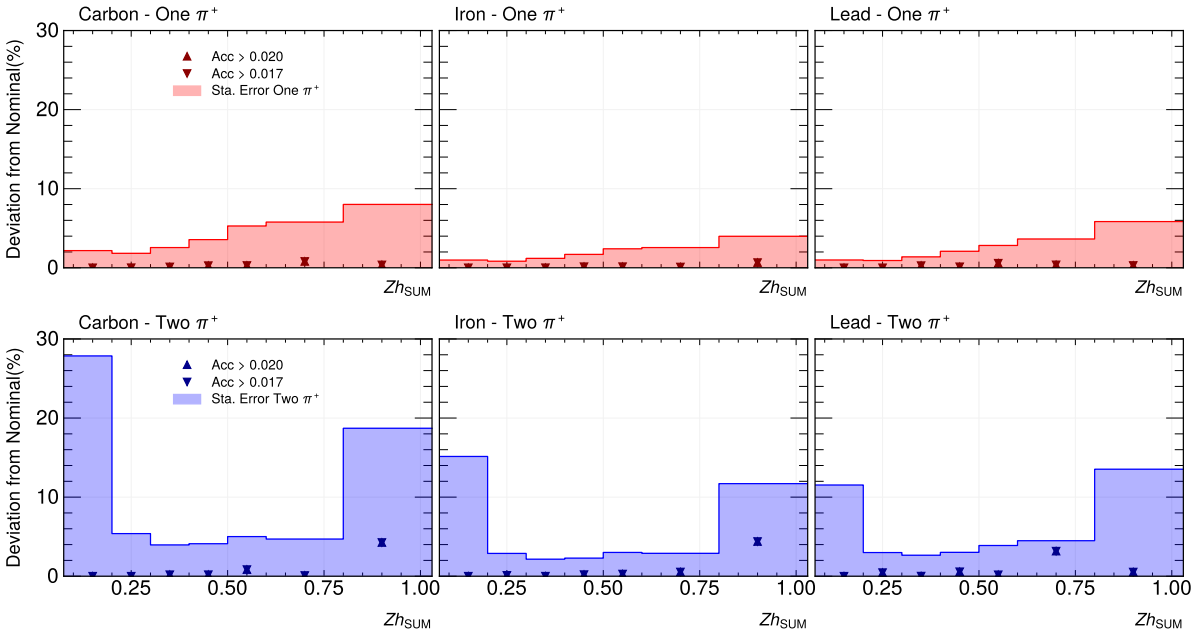

Figure 3.37: Deviation from the nominal ΔP_t^2 value due to applying a cut in Acc^i.

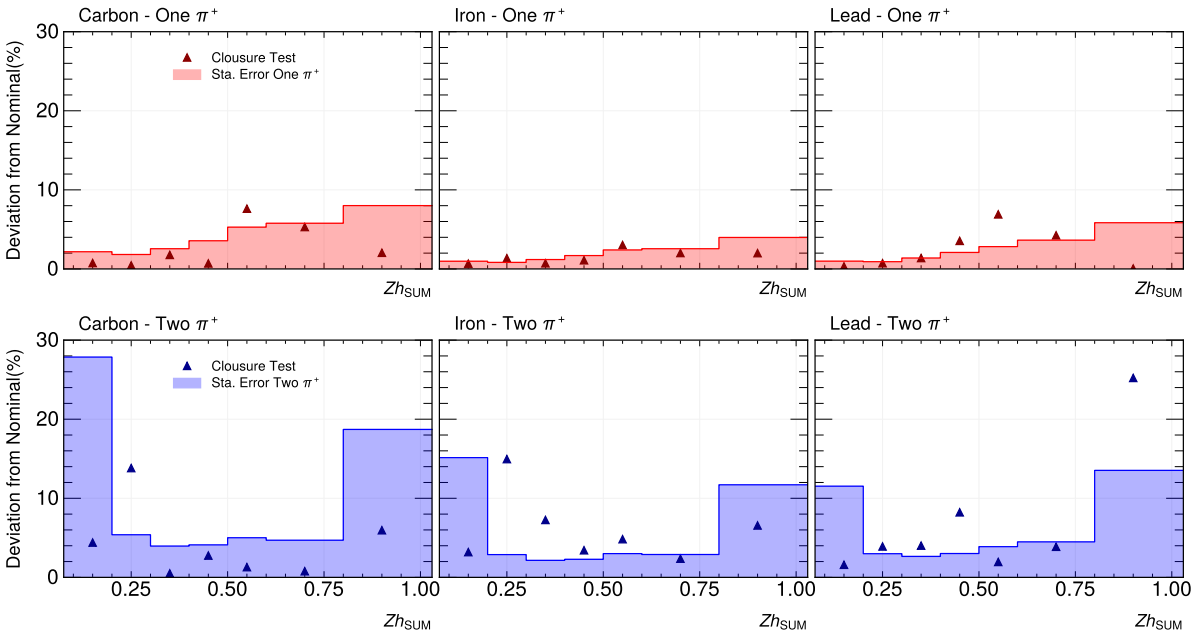

Figure 3.38: Deviation from the nominal ΔP_t^2 value due to applying the CT factor.

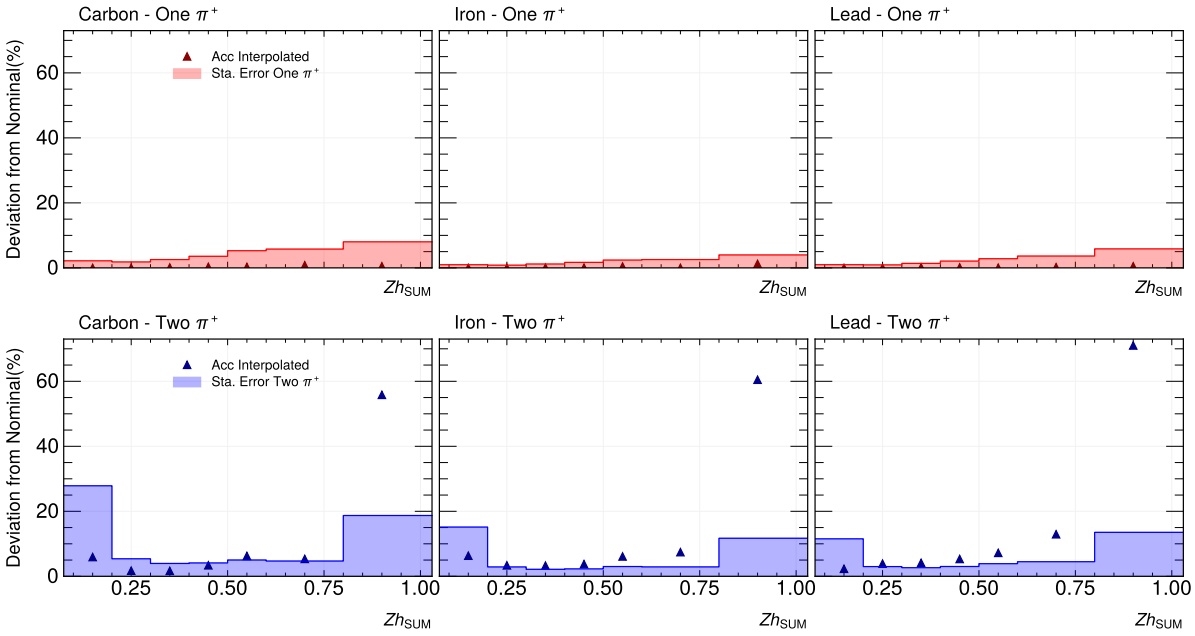

Figure 3.39: Deviation from the nominal ΔP_t^2 value due to not interpolating the acceptance factors.

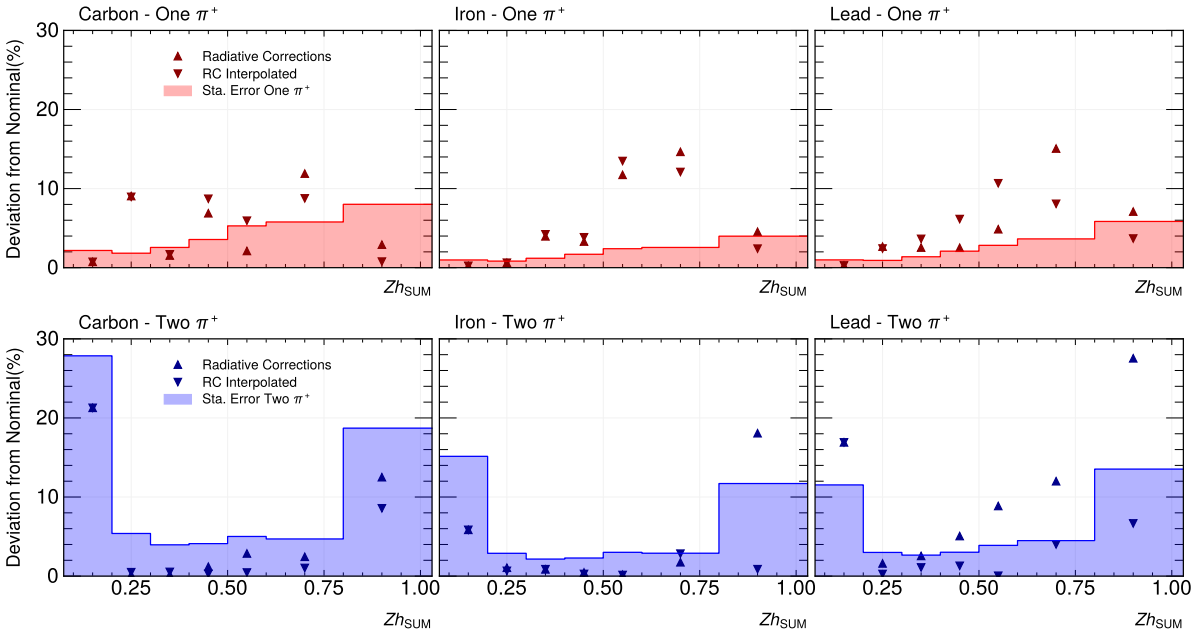

Figure 3.40: Deviation from the nominal ΔP_t^2 value due to the radiative correction.

Chapter 4

Results and Conclusions

4.1 Results

The main analysis of the thesis was the transverse momentum broadening as function of Zh_{Sum} and as function of $A^{\frac{1}{3}}$ for three different targets (carbon, iron, and lead). The results depending on Q^2 and ν are also shown; however, those results do not include the background subtraction procedure; therefore, they do not include the related systematic uncertainty source.

The results in which Zh_{Sum} is integrated take into account the region $0.1 < Zh_{Sum} < 1.0$.

The total error in the measurement has the form:

$$\sigma^2_{tot} = \sigma^2_{sta} + \sigma^2_{sys} \tag{4.1}$$

The most important results are detailed below:

- The transverse momentum broadening with all the kinematic variables integrated increases with $A^{\frac{1}{3}}$ (A is the mass number of the target) for one and two pions events (see Fig. 4.2). The plot also shows a significant impact in the number of pions, being bigger for two pions events. The measurement is 1.8 times bigger for carbon and around 1.5 times bigger for iron and lead.

- The broadening is bigger for more massive targets for one and two pions events in all the bins of Zh_{Sum}. see Fig. 4.5.

- There is a strong dependence in the number of pions for the results as a function of Zh_{Sum}. For $Zh < 0.3$, the broadening is smaller for two pion events; for $Zh_{Sum} > 0.3$, the results are bigger for two pions events. see Fig. 4.5.

- The difference between one and two pions events increases with Zh_{Sum} (see 4.6). For $Zh_{Sum} < 0.2$, the broadening for two pions is around half that of two pions, and the bigger differences are in $0.8 < Zh_{Sum} < 1$. where the broadening is around two and a half times bigger for two pion events.

- In the region $0.1 < Zh_{Sum} < 0.2$ and $0.8 < Zh_{Sum} < 1.0$, the errors for two pions events are much bigger than in the rest of Zh_{Sum}. In that region, the errors are within 34% and 54% (see Tab. 4.1 - 4.3).

- The results have a similar dependence on Q^2 for one and two pions events, increasing in both cases. see Fig. 4.7.

- The dependence on ν is different for one and two pions events. For one pion events, the broadening increases linearly with ν, but for two pions events, the broadening decreases in high ν for carbon and lead, and it is almost constant for lead. see Fig. 4.8.

There are different models describing the transverse momentum broadening [25], [26], [27]; in some of them increase in the broadening implies an increase in the in-medium path length. There is also a hypothesis that when a struck quark has a longer in-medium path length, more pions will be produced. This could be one of the reasons why the broadening for two-pions events is bigger in most of the cases.

The results are shown in plots and in tables in the Subsections 4.4 - 4.5.

4.2 Next steps

To finish the analysis, the plan is to find a method to reduce the systematic errors in the first and last bin of Zh_{Sum}; if it is not possible, those bins will not be included in the final results. Also, the idea is to apply the background subtraction procedure to the results depending on Q^2 and ν; however, the effect is expected to be small.

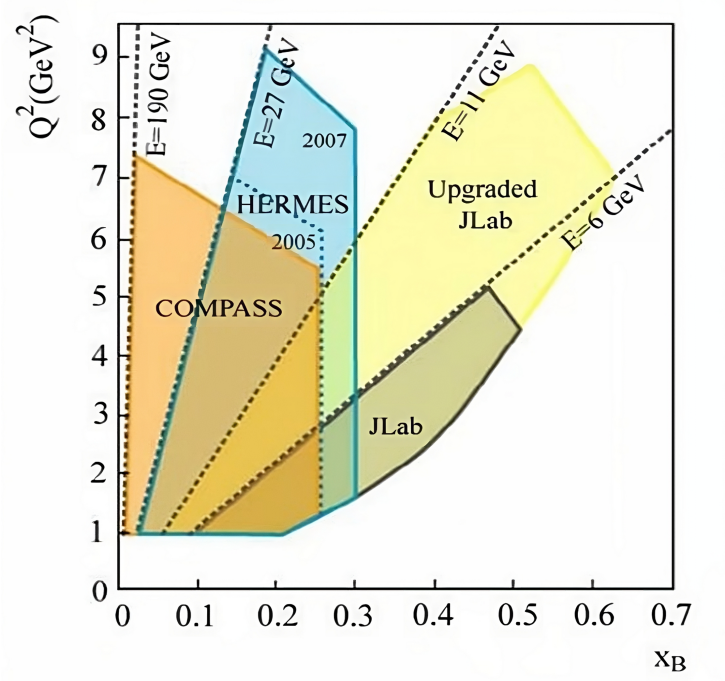

Figure 4.1: Kinematic phase space for different experiments. The yellow region represent the current status of the Jefferson lab beam.

After that, the CLAS analysis note will be written and sent to the CLAS collaboration for approval. Once the collaboration approves it, the analysis will be sent to a scientific journal for publication.

Besides this analysis, in 2024, a similar experiment will be carried out in Jefferson Lab but with the current capacities of the facilities. Nowadays, CEBAF has a bigger luminosity than when the Eg2 experiment took place and also can reach 12 GeV instead of 6 GeV (see Fig. 4.1). This experiment will provide many more statistics, allowing us to complete the measurement in the bins with low statistics, make the analysis in more than one dimension, and expand the analysis to events with more pions.

4.3 Conclusions

The thesis presented the measurement for average transverse momentum broadening of DIS multiple-pion events with acceptance correction, radiative corrections, and systematic uncertainties.

The broadening was measurement as function of $A^{1/3}$, Zh_{Sum}, Q^2, and ν. The results show that the broadening is bigger when the number of pions increases in almost all the kinematic space, except at low Zh_{Sum}. Also the results increase with the mass of the

target in all the cases.

Due to the low statistics in low and high Zh_{Sum}, the first and last bins will probably not be included in the final results when the analysis get published.

4.4 Plots

The plot of this sections show the measurement of the transverse momentum broadening. The vertical lines represents the statistical error and the horizontal line the total errors. The plots of Fig. 4.4 and 4.5 have a small shift in the horizontal direction to make them easy to read.

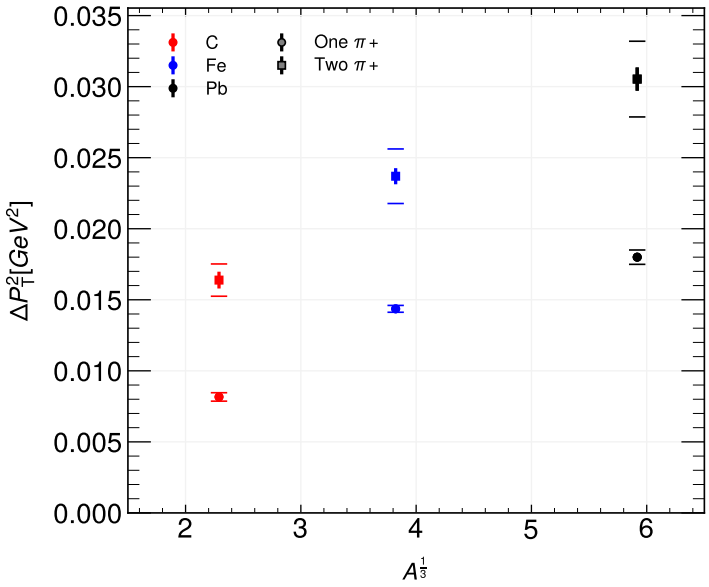

Figure 4.2: Transverse momentum broadening in function of $A^{\frac{1}{3}}$, all the other variables are integrated. The circles are one pions events, and the squares are two pions events.

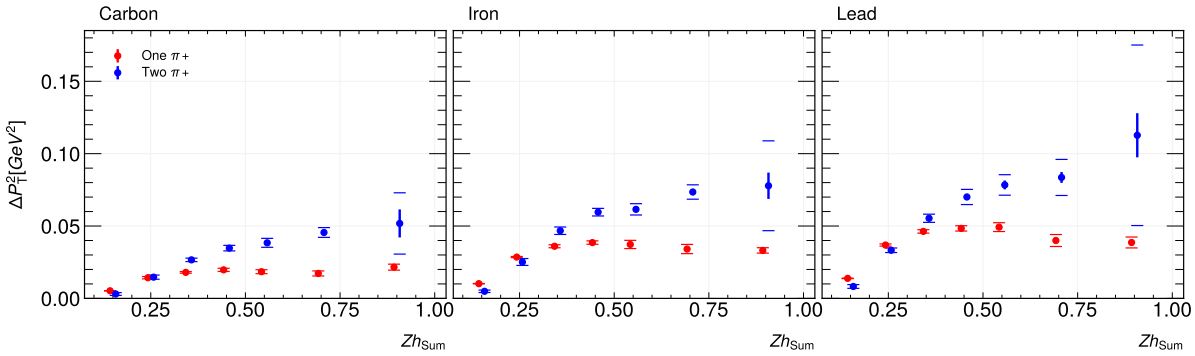

Figure 4.3: Transverse momentum broadening as a function of Zh_{Sum} (all the other variables are integrated). Each box represent a different target. In red, one pion events; and in blue, two pions events.

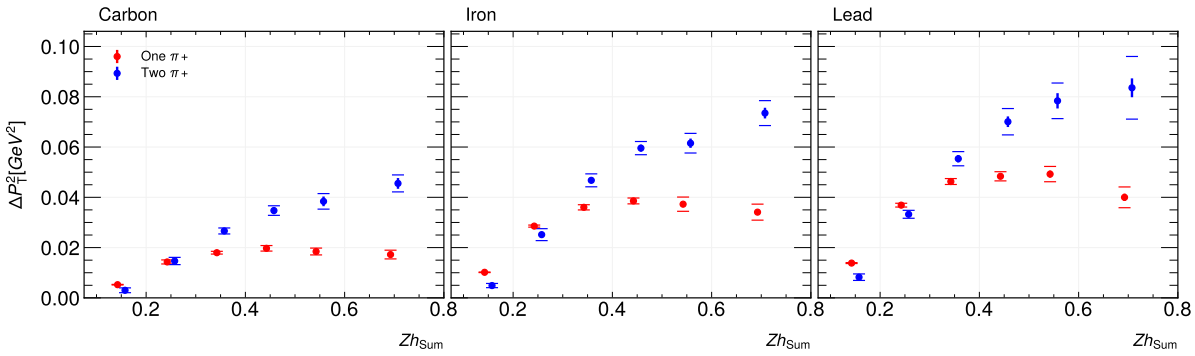

Figure 4.4: Transverse momentum broadening in function of Zh_{Sum}, for $Zh_{Sum} < 0.8$. Each box represent a different target. In red, one pion events; and in blue, two pions events.

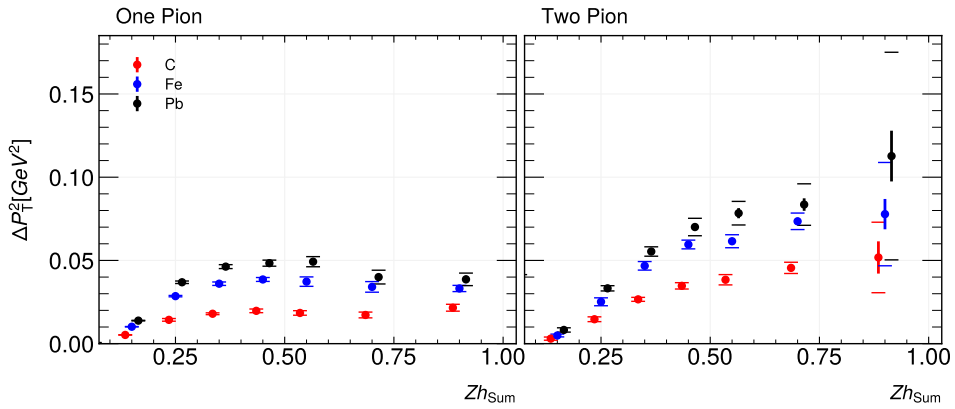

Figure 4.5: Transverse momentum broadening as a function of Zh_{Sum}, each box represent a different number of pions. In red, carbon results; in blue, iron results; and in black, lead results.

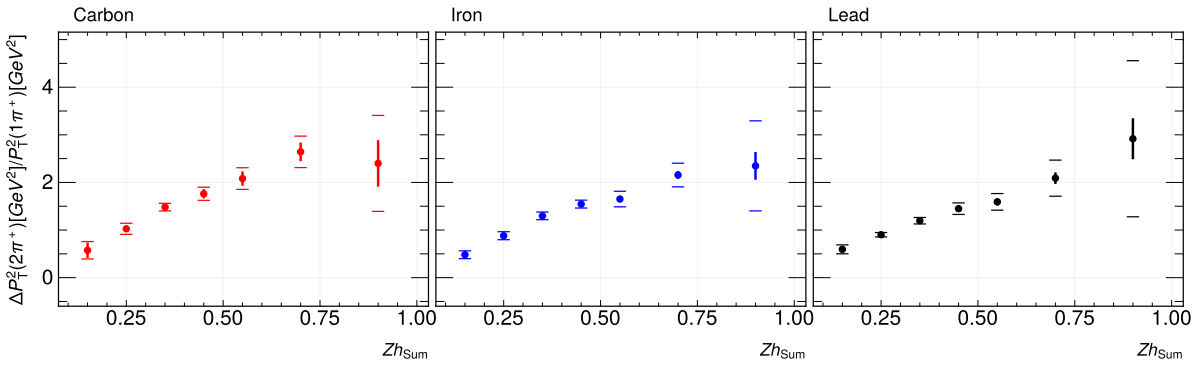

Figure 4.6: Ratio between the transverse momentum broadening of one pion event and two pion events, each box represent a different target.

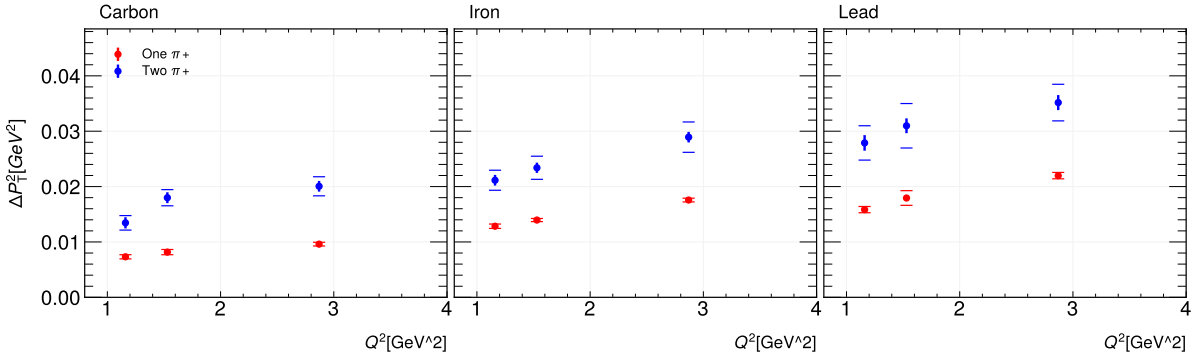

Figure 4.7: Transverse momentum broadening as a function of Q^2 (all the other variables are integrated), each box represent a different target. In red, one pion events; and in blue, two pions events.

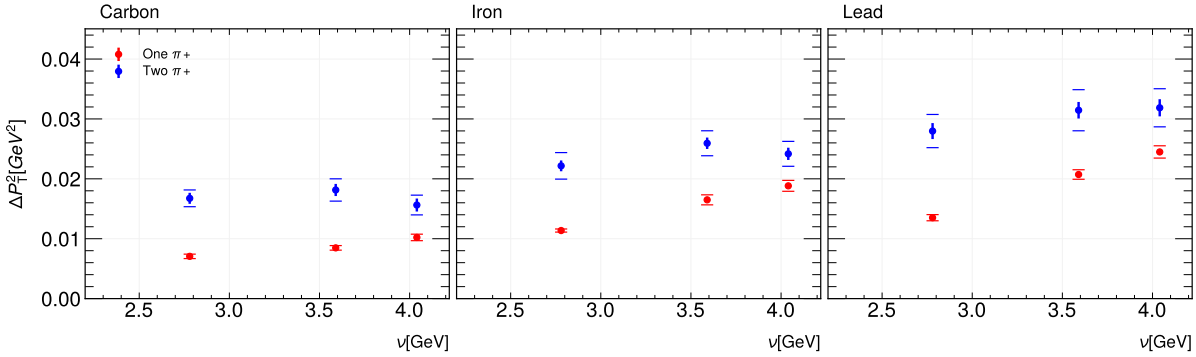

Figure 4.8: Transverse momentum broadening as a function of ν (all the other variables are integrated), each box represent a different target.. In red, one pion events; and in blue, two pions events.

4.5 Table

The exact values and errors for the transverse momentum broadening are in Tab. 4.1, 4.2, 4.3.

	One pion events				Two pion events			
Zh_{Sum}	ΔP_t^2	σ_{tot}	σ_{sta}	σ_{sys}	ΔP_t^2	σ_{tot}	σ_{sta}	σ_{sys}
0.1 - 0.2	0.0052	0.0001	0.0001	0.0	0.003	0.001	0.0008	0.0005
0.2 - 0.3	0.0143	0.0008	0.0003	0.0008	0.0147	0.0014	0.0008	0.0012
0.3 - 0.4	0.018	0.0005	0.0005	0.0003	0.0266	0.0012	0.0011	0.0006
0.4 - 0.5	0.0197	0.0011	0.0007	0.0008	0.0347	0.0019	0.0014	0.0013
0.5 - 0.6	0.0184	0.0014	0.001	0.0009	0.0384	0.0031	0.0019	0.0024
0.6 - 0.8	0.0172	0.0017	0.001	0.0014	0.0455	0.0034	0.0021	0.0026
0.8 - 1.0	0.0216	0.0021	0.0017	0.0011	0.0518	0.0212	0.0097	0.0188

Table 4.1: Transverse momentum broadening for carbon. The results are in GeV^2

	One pion events				Two pion events			
Zh_{Sum}	ΔP_t^2	σ_{tot}	σ_{sta}	σ_{sys}	ΔP_t^2	σ_{tot}	σ_{sta}	σ_{sys}
0.1 - 0.2	0.0102	0.0001	0.0001	0.0001	0.0049	0.0008	0.0007	0.0004
0.2 - 0.3	0.0285	0.0004	0.0002	0.0003	0.0252	0.0024	0.0007	0.0023
0.3 - 0.4	0.036	0.001	0.0004	0.0009	0.0468	0.0026	0.001	0.0024
0.4 - 0.5	0.0386	0.0012	0.0007	0.001	0.0596	0.0026	0.0014	0.0022
0.5 - 0.6	0.0373	0.0028	0.0009	0.0027	0.0615	0.0039	0.0018	0.0034
0.6 - 0.8	0.0341	0.0032	0.0009	0.0031	0.0735	0.005	0.0021	0.0045
0.8 - 1.0	0.0331	0.0019	0.0013	0.0013	0.0778	0.031	0.0091	0.0297

Table 4.2: Transverse momentum broadening for iron. The results are in GeV^2

	One pion events				Two pion events			
Zh_{Sum}	ΔP_t^2	σ_{tot}	σ_{sta}	σ_{sys}	ΔP_t^2	σ_{tot}	σ_{sta}	σ_{sys}
0.1 - 0.2	0.0138	0.0002	0.0001	0.0001	0.0082	0.0013	0.0009	0.0009
0.2 - 0.3	0.0369	0.0008	0.0003	0.0007	0.0332	0.0016	0.001	0.0012
0.3 - 0.4	0.0463	0.0012	0.0006	0.001	0.0554	0.0028	0.0015	0.0024
0.4 - 0.5	0.0484	0.0018	0.001	0.0015	0.0701	0.0052	0.0021	0.0048
0.5 - 0.6	0.0492	0.003	0.0014	0.0027	0.0784	0.0071	0.003	0.0064
0.6 - 0.8	0.04	0.0041	0.0015	0.0039	0.0836	0.0125	0.0038	0.0119
0.8 - 1.0	0.0386	0.0038	0.0023	0.003	0.1127	0.0624	0.0152	0.0605

Table 4.3: Transverse momentum broadening for lead. The results are in GeV^2

	One pion events				Two pion events			
Q^2	ΔP_t^2	σ_{tot}	σ_{sta}	σ_{sys}	ΔP_t^2	σ_{tot}	σ_{sta}	σ_{sys}
1.00 - 1.32	0.0073	0.0004	0.0003	0.0002	0.0135	0.0013	0.001	0.0008
1.32 - 1.74	0.0082	0.0005	0.0003	0.0004	0.018	0.0015	0.001	0.0011
1.74 - 4.00	0.0096	0.0003	0.0003	0.0002	0.0201	0.0017	0.001	0.0014

Table 4.4: Transverse momentum broadening for carbon for different Q^2 bins. The results are in GeV^2

	One pion events				Two pion events			
Q^2	ΔP_t^2	σ_{tot}	σ_{sta}	σ_{sys}	ΔP_t^2	σ_{tot}	σ_{sta}	σ_{sys}
1.00 - 1.32	0.0128	0.0004	0.0003	0.0003	0.0211	0.0018	0.001	0.0015
1.32 - 1.74	0.014	0.0003	0.0002	0.0002	0.0234	0.0021	0.0009	0.0019
1.74 - 4.00	0.0176	0.0003	0.0002	0.0003	0.0289	0.0027	0.001	0.0026

Table 4.5: Transverse momentum broadening for iron for different Q^2 bins. The results are in GeV^2

	One pion events				Two pion events			
Q^2	ΔP_t^2	σ_{tot}	σ_{sta}	σ_{sys}	ΔP_t^2	σ_{tot}	σ_{sta}	σ_{sys}
1.00 - 1.32	0.0158	0.0006	0.0004	0.0004	0.0279	0.0031	0.0014	0.0028
1.32 - 1.74	0.0179	0.0013	0.0003	0.0013	0.031	0.004	0.0013	0.0038
1.74 - 4.00	0.022	0.0006	0.0003	0.0005	0.0352	0.0033	0.0014	0.003

Table 4.6: Transverse momentum broadening for lead for different Q^2 bins. The results are in GeV^2

	One pion events				Two pion events			
ν	ΔP_t^2	σ_{tot}	σ_{sta}	σ_{sys}	ΔP_t^2	σ_{tot}	σ_{sta}	σ_{sys}
2.20 - 3.36	0.0071	0.0004	0.0002	0.0003	0.0167	0.0014	0.0009	0.0011
3.36 - 3.82	0.0085	0.0004	0.0003	0.0002	0.0181	0.0019	0.001	0.0016
3.82 - 4.26	0.0102	0.0005	0.0004	0.0004	0.0156	0.0016	0.0011	0.0012

Table 4.7: Transverse momentum broadening for carbon for different ν bins. The results are in GeV^2

	One pion events				Two pion events			
ν	ΔP_t^2	σ_{tot}	σ_{sta}	σ_{sys}	ΔP_t^2	σ_{tot}	σ_{sta}	σ_{sys}
2.20 - 3.36	0.0114	0.0003	0.0002	0.0002	0.0222	0.0022	0.0009	0.002
3.36 - 3.82	0.0165	0.0008	0.0003	0.0008	0.0259	0.0021	0.001	0.0019
3.82 - 4.26	0.0188	0.0009	0.0003	0.0008	0.0242	0.0021	0.001	0.0018

Table 4.8: Transverse momentum broadening for iron for different ν bins. The results are in GeV^2

	One pion events				Two pion events			
ν	ΔP_t^2	σ_{tot}	σ_{sta}	σ_{sys}	ΔP_t^2	σ_{tot}	σ_{sta}	σ_{sys}
2.20 - 3.36	0.0135	0.0005	0.0003	0.0004	0.028	0.0028	0.0013	0.0024
3.36 - 3.82	0.0207	0.0008	0.0004	0.0007	0.0315	0.0034	0.0014	0.0031
3.82 - 4.26	0.0245	0.001	0.0005	0.0009	0.0319	0.0032	0.0014	0.0028

Table 4.9: Transverse momentum broadening for for different ν bins. The results are in GeV^2

Bibliography

[1] A. C.-S. Robin Devenish, *Deep Inelastic Scattering*. Oxford University Press, 2004.

[2] F. Halzen and A. D. Martin, *QUARKS AND LEPTONS: AN INTRODUCTORY COURSE IN MODERN PARTICLE PHYSICS*. John Wiley & Sons, 1984.

[3] P. D. G. et al, "Review of Particle Physics," *Progress of Theoretical and Experimental Physics*, vol. 2020, 08 2020. 083C01.

[4] B. Kopeliovich, J. Nemchik, and I. Schmidt, "Time evolution of jets and perturbative color neutralization," *Nuclear Physics A*, vol. 782, no. 1, pp. 224–233, 2007.

[5] A. Accardi, J. L. Albacete, M. Anselmino, N. Armesto, E. C. Aschenauer, A. Bacchetta, D. Boer, W. K. Brooks, T. Burton, N. B. Chang, W. T. Deng, A. Deshpande, M. Diehl, A. Dumitru, R. Dupré, R. Ent, S. Fazio, H. Gao, V. Guzey, and H. H. et al, "Electron ion collider: The next qcd frontier - understanding the glue that binds us all," 2014.

[6] A. Airapetian and H. C. et al., "Transverse momentum broadening of hadrons produced in semi-inclusive deep-inelastic scattering on nuclei," *Physics Letters B*, vol. 684, no. 2, pp. 114–118, 2010.

[7] Leemann, Christoph W. and Douglas, David R. and Krafft, Geoffrey A., "THE CONTINUOUS ELECTRON BEAM ACCELERATOR FACILITY: CEBAF at the Jefferson Laboratory," *Annual Review of Nuclear and Particle Science*, vol. 51, no. 1, pp. 413–450, 2001.

[8] B.A. Mecking et. al., "The CEBAF large acceptance spectrometer (CLAS)," *Nuclear Instruments and Methods in Physics Research Section A: Accelerators, Spectrometers, Detectors and Associated Equipment*, vol. 503, no. 3, pp. 513–553, 2003.

[9] M. D. et. al., "Probing high-momentum protons and neutrons in neutron-rich nuclei," *Nature*, vol. 560, pp. 617–621, Aug 2018.

[10] CLAS Collaboration (M.D Mestayer et. al) , "The CLAS drift chamber system," *Nuclear Instruments and Methods in Physics Research Section A: Accelerators, Spectrometers, Detectors and Associated Equipment*, vol. 449, no. 1, pp. 81–111, 2000.

[11] W. Leo, *Techniques for Nuclear and Particle Physics Experiments: A How-to Approach*. Springer, 1994.

[12] CLAS Collaboration (G. Adams et. al), "The CLAS Cherenkov detector," *Nuclear Instruments and Methods in Physics Research Section A: Accelerators, Spectrometers, Detectors and Associated Equipment*, vol. 465, no. 2, pp. 414–427, 2001.

[13] CLAS Collaboration (E.S. Smith et. al), "The time-of-flight system for CLAS," *Nuclear Instruments and Methods in Physics Research Section A: Accelerators, Spectrometers, Detectors and Associated Equipment*, vol. 432, no. 2, pp. 265–298, 1999.

[14] CLAS Collaboration (M. Amarian et. al.), "The clas forward electromagnetic calorimeter," *Nuclear Instruments and Methods in Physics Research Section A: Accelerators, Spectrometers, Detectors and Associated Equipment*, vol. 460, no. 2, pp. 239–265, 2001.

[15] H. Hakobyan and W. B. et. al., "A double-target system for precision measurements of nuclear medium effects," *Nuclear Instruments and Methods in Physics Research Section A: Accelerators, Spectrometers, Detectors and Associated Equipment*, vol. 592, no. 3, pp. 218–223, 2008.

[16] S. Moran, "Charged-pion multiplicity ratio measurement with eg2 data," *CLAS Analysis Note*, 2021.

[17] L. Zana, "Evidence for the onset of color transparency in ρ_0 electroproduction off nuclei," *Physics Letters B*, vol. 712, no. 4, pp. 326–330, 2012.

[18] T. Minneva, "Neutral pion multiplicity ratios from sidis lepton- nuclear scattering," *CLAS Analysis Note*, 2020.

[19] R. Dupré, "Quark fragmentation and hadron formation in nuclear matter," *PhD thesis. Université de Lyon*, 2011.

[20] H. Hakobyan, "Observation of quark propagation pattern in nuclear medium," *PhD thesis. Yerevan State University*, 2008.

[21] H. W. Kendall, "Deep inelastic scattering: Experiments on the proton and the observation of scaling," *Rev. Mod. Phys.*, vol. 63, pp. 597–614, 1991.

[22] I. Akushevich, N. Shumeiko, and A. Soroko, "Radiative effects in the processes of hadron electroproduction," *The European Physical Journal C*, vol. 10, pp. 681–687, oct 1999.

[23] I. Akushevich, A. Ilyichev, and M. Osipenko, "Lowest order QED radiative corrections to five-fold differential cross section of hadron leptoproduction," *Physics Letters B*, vol. 672, pp. 35–44, feb 2009.

[24] E. Molina, "Experimental measurement and phenomenological study of positive pion production in nuclear media," *Ms thesis. Universidad Tecnica Federico Santa Maria*, 2022.

[25] S. Domdey, D. Grünewald, B. Kopeliovich, and H. Pirner, "Transverse momentum broadening in semi-inclusive DIS on nuclei," *Nuclear Physics A*, vol. 825, pp. 200–211, jul 2009.

[26] B. Kopeliovich, J. Nemchik, E. Predazzi, and A. Hayashigaki, "Nuclear hadronization: within or without?," *Nuclear Physics A*, vol. 740, no. 1, pp. 211–245, 2004.

[27] William K. Brooks and Jorge A. López, "Estimating the color lifetime of energetic quarks," *Physics Letters B*, vol. 816, p. 136171, may 2021.